

Silicon Photomultiplier Classification of the Pre-Production GCT Camera of CTA

Silicon Photomultiplier Klassifikation der Pre-Production GCT Kamera von CTA

Master-Thesis von Ben Gebhardt aus Heidelberg

Tag der Einreichung:

1. Gutachten: Dr. Richard White (MPIK)

2. Gutachten: Prof. Jim Hinton (MPIK)

3. Gutachten: Prof. Tetyana Galatyuk (TU DA)



TECHNISCHE
UNIVERSITÄT
DARMSTADT

Fachbereich Physik

Max Planck Institut für Kernphysik Heidelberg

8 Silicon Photomultiplier Classification of the Pre-Production GCT Camera of CTA
Silicon Photomultiplier Klassifikation der Pre-Production GCT Kamera von CTA

Vorgelegte Master-Thesis von Ben Gebhardt aus Heidelberg

1. Gutachten: Dr. Richard White (MPIK)
2. Gutachten: Prof. Jim Hinton (MPIK)
3. Gutachten: Prof. Tetyana Galatyuk (TU DA)

Tag der Einreichung:

10 **Abstract**
11

12 Earth is continuously hit by high energy gamma radiation that carries with it vast amounts
13 of information about the most energetic phenomenon in our galaxy and beyond. Part of this
14 information is delivered to Earth in the form of a gamma ray induced particle shower in our
15 atmosphere. While it is also possible to detect those particles directly on the ground, traveling
16 through Earth's atmosphere those particles emit Cherenkov light. Particles in the shower pro-
17 duce a light cone that can be detected by telescopes on the ground. From the Cherenkov light,
18 it is possible to reconstruct the direction and energy of the gamma ray.

19 One such experiment capable of observing gamma rays is the proposed Cherenkov Telescope
20 Array. It consists of over 100 telescopes grouped in three energy ranges, deployed on two array
21 sites, achieving whole-sky coverage. Different designs of the telescopes are able to use Sili-
22 con Photomultipliers for photon detection. Silicon Photomultipliers are semiconductors that
23 attracted increased attention for their possible use in astroparticle physics. Each detected pho-
24 ton entering the detector is converted to a measurable signal through avalanche creation. Being
25 a fairly new technology, they are continuously being developed, and finding the most promising
26 candidate is a task spread across many groups.

27 In this work dark measurements of five proposed candidates are conducted. An initial teststand
28 for dark measurements is build, that can later be upgraded to support light measurements. Data
29 acquisition and analysis code is developed and utilized to evaluate important characteristics of
30 the candidates. Among them are the gain of a SiPM, being a measure for the signal strength
31 through conversion of a photoelectron. The temperature dependence of the gain is evaluated,
32 this is important during observation, where the gain fluctuation is required to be low in order
33 to avoid errors. Important noise characteristics are evaluated, among them thermally induced
34 dark rates and optical cross talk. Those have a direct impact on the single photon detection res-
35 olution. The dark rates originate from thermal effects, and together with the optical cross talk,
36 the temperature dependence of the noise is investigated. To conclude, the measured devices
37 are compared among themselves and against results from involved groups, to find the most
38 promising initial candidate.



Abstract

40
41
42 worum es geht



43 List of Figures

45	1	Cosmic radiation	7
46	2	Fermi LAT	8
47	3	Cherenkov light cone	10
48	4	GCT and CHEC-M at Meudon	12
49	5	GCT optical system	13
50	6	CHEC focal plane	14
51	7	Structure and carrier multiplication through an avalanche inside a SiPM	16
52	8	Cherenkov light spectrum	18
53	9	Avalanche induced secondary effects	21
54	10	Teststand outside view	23
55	11	Thermal chamber inside view	24
56	12	Experimental setup scheme	25
57	13	Shaped versus unshaped signal	26
58	14	Zero pole cancelation	26
59	15	Multi p.e. persistence plot	27
60	16	Pulse height spectrum generated by the oscilloscope	27
61	17	Pedestal subtraction	30
62	18	Peak Detection	31
63	19	Fitted pulse area histogram	32
64	20	Regression line plots of 1p.e. and Δ p.e.	33
65	21	MPD parameter challenges and the integration window	35
66	22	MPD parameter challenges and the threshold	36
67	23	List of examined SiPM devices	38
68	24	CHEC-S SiPM	40
69	25	CHEC-S average pulse shape	40
70	26	CHEC-S gain	41
71	27	CHEC-S DCR	42
72	28	CHEC-S OCT	43
73	29	LCT5 6mm SiPM	45
74	30	LCT5 6mm average pulse shape	45
75	31	LCT5 6mm gain	46
76	32	LCT5 6mm DCR	47
77	33	LCT5 6mm OCT	48
78	34	LCT5 7mm SiPM	49
79	35	LCT5 7mm average pulse shape	49
80	36	LCT5 7mm gain	50

81	37	LCT5 7mm DCR	51
82	38	LCT5 7mm OCT	51
83	39	LCT5 LVR 6mm SiPM	53
84	40	LCT5 LVR 6mm average pulse shape	53
85	41	LCT5 LVR 6mm gain	54
86	42	LCT5 LVR 6mm DCR	54
87	43	LCT5 LVR 6mm OCT	55
88	44	SensL FJ60035 SiPM and average pulse shape	56
89	45	SensL FJ60035 gain	57
90	46	SensL FJ60035 DCR	57
91	47	SensL FJ60035 OCT	58
92	48	DCR device comparison	60
93	49	OCT device comparison	61
94	50	Comparison based on two proposed points of operation	63
95	51	PDE versus OCT comparison	64
96	52	CTA in Chile and the stereoscopic technique	69
97	53	Current IACT experiments	69
98	54	OCT dependency on the cell-size	70
99	55	Pulse area spectra of three different integration windows	73
100	56	S12642 pulse height and pulse area spectrum	74
101	57	LCT5 6mm pulse area spectrum	75
102	58	Breakdown-voltage versus temperature	76
103	59	Breakdown-voltage dependency	77
104	60	Full schematic of the shaper developed at the University of Leicester.	78
105	61	List of candidate SiPM devices	79
106	62	CHEC-S pixel comparison of the gain	80
107	63	CHEC-S pixel comparison of the DCR	80
108	64	CHEC-S pixel comparison of the OCT	81
109	65	Raw data	82
110	66	Peak detection level	83
111	67	Number of peaks detected	84
112	68	Integration window	85

113 **Contents**

115	1 Cosmic Radiation	7
116	1.1 Air shower induced Cherenkov Radiation	9
117	1.2 Imaging Atmospheric Cherenkov Telescopes	10
118	2 Cherenkov Telescope Array	12
119	2.1 Gamma Cherenkov Telescope	13
120	2.2 Compact High Energy Camera	14
121	3 Silicon Photomultipliers	16
122	3.1 SiPM characteristics	16
123	3.2 Gain of a Silicon Photomultiplier	18
124	3.3 Thermally induced dark counts	20
125	3.4 Avalanche-induced secondary effects	20
126	3.5 Photon Detection Efficiency	22
127	4 Experimental Setup	23
128	5 Data Analysis	29
129	5.1 Tracefile Conversion	29
130	5.2 Pedestal Subtraction	30
131	5.3 Peak Detection	31
132	5.4 Gain Extraction	32
133	5.5 Analysis improvements	34
134	5.6 Data Challenges	35
135	6 Results	38
136	6.1 SiPM devices for CTA	38
137	6.2 Hamamatsu S12642-1616PA-50 50 μ m 3mm	40
138	6.3 Hamamatsu LCT5 50 μ m 6mm	45
139	6.4 Hamamatsu LCT5 75 μ m 7mm	49
140	6.5 Hamamatsu IVR 50 μ m 6mm	53
141	6.6 SensL FJ60035 6mm 35 μ m	56
142	7 Comparison	59
143	7.1 Dark Count Rate	59

¹⁴⁴	7.2 Optical Cross Talk	60
¹⁴⁵	7.3 Point of Operation Comparison	62
¹⁴⁶	7.4 Photon Detection Efficiency	62
¹⁴⁷	8 Conclusion and Outlook	65
¹⁴⁸	9 Glossary	66
¹⁴⁹	10 Bibliography	67
¹⁵⁰	11 Appendix	69

151 1 Cosmic Radiation

153 Cosmic rays consist of a single particle with energies from 10^{10} to 10^{20} eV and describes extra-
154 solar charged particles arriving on Earth and hitting the atmosphere (fig(1)). The most energetic
155 laboratory based accelerators operate in the 10^{12} eV energy range. They were discovered by V.F.
156 Hess in 1912 during the famous balloon flight experiments. He aimed to measure the con-
157 ductivity of air, that until then, was believed to be an insulator resulting in some problems
158 regarding the discharge of an electrically charged body, no matter how well it was isolated from
159 the ground. Hess found the air's conductivity to increase with higher altitude, concluding the
160 presence of a large amount of ionizing radiation above the atmosphere.
161 Cosmic rays do not include those low energy particles originating from our sun. With a particle
162 energy up to 1 keV, those are referred to as solar wind, which means, by definition, cosmic rays
163 arrive on Earth from outside our solar system. They consist of 87% protons, 12% α -particles
164 , 1% heavier nuclei and some electrons. High energy cosmic rays hitting Earth are very rare,
165 averaging to one per year in an area of one square kilometer. Except at those very high ener-
166 gies ($>10^{18}$ eV) cosmic rays will not reach earth directly and cannot be observed to pinpoint
167 their source. Traveling through the interstellar medium , they get scattered by the interstellar
168 magnetic fields, the cosmic microwave background and other hindrances and therefore have
169 lost all directional information. However, directly observable cosmic rays, for example at the
170 Pierre-Auger Observatory, provide an insight into cosmic particle accelerators.[2]

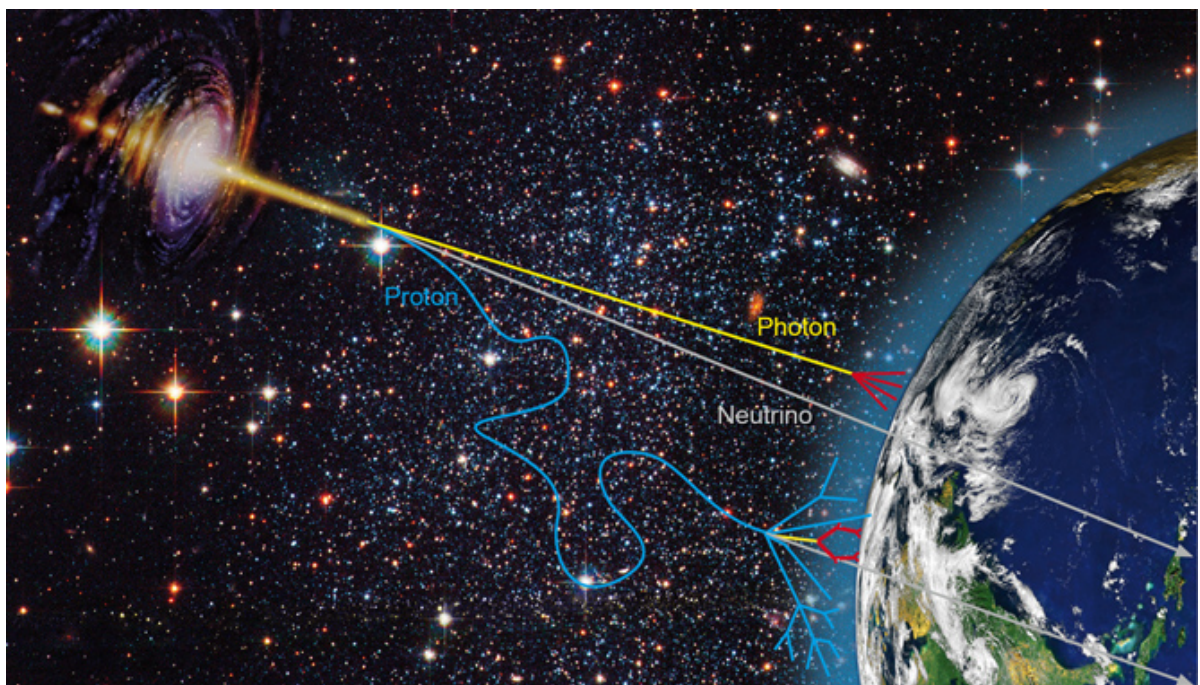


Figure 1: Gamma radiation photons (yellow) and scattered cosmic ray protons (blue) from an astrophysical source arriving on Earth. Neutrinos (grey) mostly do not interact. Picture from [25]

171 Cosmic rays of the higher energies are therefore observed via a detour: Gamma radiation.

172

173 Gamma radiation cannot be generated by
174 thermal emission of hot stellar objects, the
175 only event with a high enough temperature
176 to produce thermal radiation in the range
177 of GeV and TeV gamma radiation would be
178 the big bang, there is and has been nothing
179 else in the known universe. If thermal
180 radiation reflects the temperature of the
181 emitting body, what do gamma rays tell
182 us?



Figure 2: FermiLAT Picture from [26]

183
184 Gamma radiation probe a non-thermal universe. In this other mechanisms are needed to concentrate large amounts of energy into a
185 single quantum. The possible emission mechanisms are outlined below.

186
187 There are many diverse mechanisms of emitting gamma radiation. Gamma rays are generated
188 by high relativistic particles, in a first step for example: accelerated by the shockwave of a super-
189 nova explosion. Those cosmic rays then collide with ambient gas, interact with photons or
190 magnetic fields, by inverse Compton scattering, emitting high energy photons in a down-top
191 fashion. Very-high-energy (VHE) gamma radiation is defined as gamma radiation in the energy
192 range of 10^{11} to 10^{14} eV.

193

194 One such source of VHE gamma radiation and also the most famous, because the first to be
195 discovered, lies within the Crab Nebula. The Neutron Star located inside the Crab Nebula is a
196 Pulsar and the remnant of Supernova1054 and steadily emits gamma radiation energies up to
197 80 TeV. Another compound of the gamma radiation here is the so called Pulsar Wind Nebula. It
198 is composed of highly relativistic charged particles from the Pulsars giant rotating magnetic field
199 interacting with the expanding Supernova remnant via inverse Compton scattering. Supernova
200 shockwaves themselves can also drive atomic nuclei to high energies which in turn emit observ-
201 able gamma-rays in a top-down fashion. Additionally, binary systems consisting of a black hole
202 or pulsar orbiting a massive star can emit a flow of high-energy particles with varying intensity,
203 based on the elliptical orbit, where particle acceleration conditions vary.

204 Just like thermal radiation reflects the temperature of the emitting object, the flux and energy
205 spectrum of the gamma rays reflect the flux and spectrum of the high energy seed particles,
206 coming from the source. So they can be used to trace these cosmic rays and electrons in distant
207 regions of our own galaxy or even beyond. [1]

208 One surprise was the discovery of so called "dark sources" , objects emitting VHE gamma-rays,

209 but have no counterpart in other wavelengths, meaning those objects might only be observ-
210 able through gamma-rays. In extragalactic regions, gamma rays provide information on active
211 galaxies, where a constant stream of gas feeds a supermassive black hole at the center, releasing
212 enormous amounts of energy. From there, gamma rays are believed to be emitted, giving insight
213 into one of the most violent but to date poorly understood environments in our universe.

214 Even higher energy gamma rays could also be the product of decays of heavy particles, like
215 dark matter or cosmic strings. They therefore also provide a window to the discovery of dark
216 matter.

217

218 Gamma Radiation carries unique information about the most energetic phenomena in our
219 universe. The only problem is, our atmosphere is opaque for gamma radiation, gamma ray as-
220 tronomy in the lower energies is done by satellite based instruments like FermiLAT. The Large
221 Area Telescope, the principle scientific instrument on the Fermi Gamma-Ray Space Telescope
222 Spacecraft sensitive in the energy range between 20 MeV and 100 GeV, launched in June 2008
223 fig(2). To reach the higher energy range through space based telescopes is very inconvenient,
224 since the required mass the telescope active area would need to detect the gamma rays increases
225 with gamma ray energy, and can therefore be very expensive to launch into space. Low energy
226 gamma rays can be efficiently captured by a volume appropriate for a spacecraft, for higher en-
227 ergy gamma rays using other interaction and detection media, like water or Earth's atmosphere,
228 is more viable.

229 **1.1 Air shower induced Cherenkov Radiation**

230 The effect of gamma radiation on Earth is visible through gamma-ray induced particle cascades.
231 When a primary particle, i.e. a gamma photon or cosmic ray enters the atmosphere and collides
232 with a nucleus of the air, it gets scattered and creates secondary electrons, positrons and pho-
233 tons. Those secondary particles also interact with the atmosphere creating a cascade of particles
234 called a particle shower.

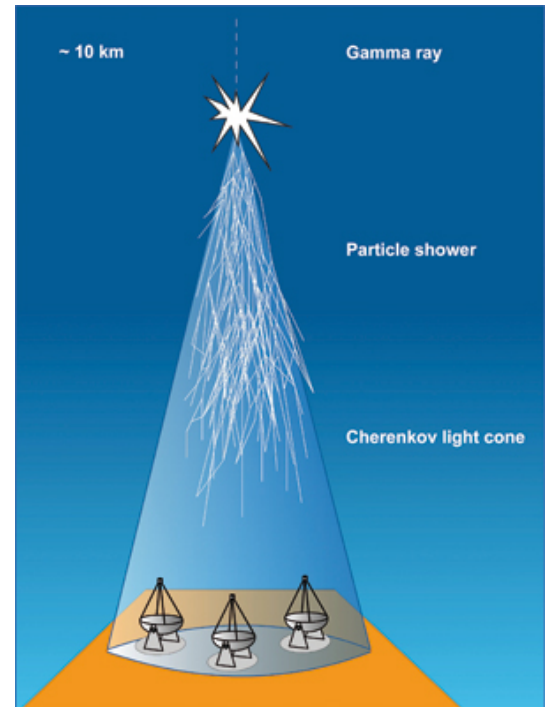
235 In this air shower, the initial and each subsequent particle traveling through our atmosphere
236 emits Cherenkov light. Cherenkov radiation is a phenomenon caused by charged particles trav-
237 eling faster than the local speed of light would allow in that medium. This light is emitted in a
238 narrow cone with an increasing angle as the particles travel downward. This Cherenkov light
239 shows as a very short ($\sim 5\text{ns}$) flash with a peak in the UV-spectrum at around 330nm. Thus,
240 we can image the particle cascade measured with the telescope and can reconstruct the direc-
241 tion and energy through a stereoscopic image of the shower taken by multiple telescopes (see
242 section(A)), reconstructing the position of the source in the sky. It is also possible to recon-
243 struct the energy of the original photon from the amount of light produced, because energy is
244 conserved, so all energy of the original photon is now distributed between the particles of the
245 shower.

247 To determine whether it is a hadronic shower, originating from cosmic rays, or a gamma shower,
248 originating from gamma ray photons, the shape of the shower and so called Hillas parameters
249 are used to determine the difference.

250 1.2 Imaging Atmospheric Cherenkov Telescopes

252 The technique, pioneered by the Wipple Collaboration
253 behind the ground based experiments called
254 Imaging Atmospheric Cherenkov Telescope (IACTs)
255 aims at measuring the time, direction and en-
256 ergy of flashes of Cherenkov light from exten-
257 sive air showers caused by VHE gamma radia-
258 tion.

259 Those ground based instruments have a much larger
260 effective detection area than any satellite based in-
261 strument, which have a typical detection size of
262 1m^2 . The range of the Cherenkov flash being be-
263 tween 300-600nm, current generation Silicon Photo-
264 multipliers (SiPMs) are a promising candidate to re-
265 place the progenitor photon detector used in previ-
266 ous experiments like HESS, the Photomultiplier Tube
267 (PMT).



268 **Figure 3:** The cone of Cherenkov light
269 emitted by an extensive air
270 shower. Picture from [27]

271 Current ground based IACT experiments are HESS,
272 MAGIC and Veritas. (see section(B)) HESS¹, based in
273 Namibia, consists of four telescopes the size of 12 m
274 operating in the energy range of 3 GeV to 100 TeV. The chosen name is in honor of Victor Hess,
275 the first to discover cosmic rays. The recent HESS upgrade added a fifth larger telescope in the
276 center of the array with a mirror diameter of 28 m. MAGIC², based in La Palma one of the
277 Canary Islands, is a system consisting of two 17 m diameter telescopes at 2200m asl³, covering
278 the energy range 30 GeV and 30 TeV. Veritas⁴, operating between 50 GeV - 50 TeV consists of
279 four 12 m telescopes, based in Arizona, USA.

280 Due to the limited effective area, caused by the number of telescopes spread over a wide
281 area, most cascades are viewed by only 2 or 3 of the telescopes. Additionally, due to the low
flux of VHE gamma radiation, detectors for this energy range are spread over a large area, mak-

¹ High Energy Stereoscopic System

² Major Atmospheric Gamma Imaging Cherenkov Telescopes

³ above sea level

⁴ Very Energetic Radiation Imaging Telescope Array System

282 ing space based instruments, which detect the incident gamma ray, an inconvenient and costly
283 choice.

284

285 Another detection concept for VHE gamma radiation are ground based air shower particle
286 detectors such as the High-Altitude-Water-Cherenkov observatory (HAWC) [6]. It employs a
287 similar detection principle, recording shower particles reaching arrays of ground based particle
288 detectors filled with water as detection medium, in contrast to air in IACTs. Those have the
289 advantage of a larger duty cycle than IACTs, as they are able to operate during the day. Their
290 limited sensitivity even with high observation time however will not allow them to compete
291 with the sensitivity and resolution of IACTs such as in the CTA. The array will however be able
292 to provide useful complementary information.

2 Cherenkov Telescope Array

295 The Cherenkov Telescope Array,
 296 CTA, is a proposed ground-based
 297 observatory array of many tens of
 298 telescopes distributed over a larger
 299 energy range than before. It will al-
 300 low detection of gamma rays over a
 301 large area on the ground and from
 302 multiple different directions. The
 303 array will consist of 60 - 100 tele-
 304 scopes of different designs and sizes
 305 to cover the aimed for energy range
 306 and area. Science goals of CTA are
 307 the understanding of cosmic rays
 308 and their role in the universe, in-
 309 cluding the study of cosmic particle
 310 accelerators, such as pulsars, pulsar
 311 wind nebulae , supernova remnants
 312 and gamma ray binaries. Secondly
 313 particle acceleration around black
 314 holes of supermassive or stellar size and lastly physics beyond the Standard Model.
 315 There are currently three groups of telescopes planed, differing in their size and achievable
 316 energy range:[2]

- 317 1. LST⁵ The low energy instrument, between 20 and 200 GeV, is a 23 meter class telescope
 318 with a moderate field of view (FoV) of the order of about 4.5°.
- 319 2. MST⁶ The medium energy range, from around 100 GeV to 10 TeV, is covered by a telescope
 320 of the 12 meter class with a FoV of 7°.
- 321 3. SST⁷ The high energy instrument, operating between a few TeV to 300 TeV, is a 4 meter
 322 telescope with a FoV ranging from 9.1° to 9.6°.

323 There are currently two sites planed, which when deployed, will achieve full-sky coverage. The
 324 southern site in the Atacama Desert in Chile, one of the most driest and isolated regions on
 325 Earth, will consist of four LSTs, 24 MSTs, and about 70 SSTs covering an area of 4 km². The



Figure 4: The prototype GCT Structure with mounted CHEC-M at the Observatory at Meudon, Paris, one of the telescopes of CTA.

⁵ LST large sized telescope

⁶ MST medium sized telescope

⁷ SST small sized telescope

326 northern site will only cover 0.4 km^2 and will only contain four LSTs and 15 MSTs due to spac-
327 ing reasons with the MAGIC observatory at the same location at the Roque de los Muchachos
328 Observatory on La Palma, one of the Canary Islands.

329
330 One proposed concept for the SST is the Gamma Cherenkov Telescope (GCT) (fig(4)).
331

332 **2.1 Gamma Cherenkov Telescope**

334 The reflector design of IACTs traditionally consists of multiple mirror segments, which focus the
335 incident light onto a camera covering $\sim 1 \text{ m}$ with pixels $1'' - 1.5''$ in diameter. Such a reflector
336 design is proposed for both, the LST and the MST of CTA resulting in the telescope sizes men-
337 tioned in section(2) above, that will use the traditional PMTs.

338 For the SST such a design would result in a cheap telescope structure, but a disproportionately
339 expensive camera, i.e. the cost and size of the structure is reduced, while the cost of the camera
340 is not. The cost of one SST camera would be near the cost of a MST camera, which given the

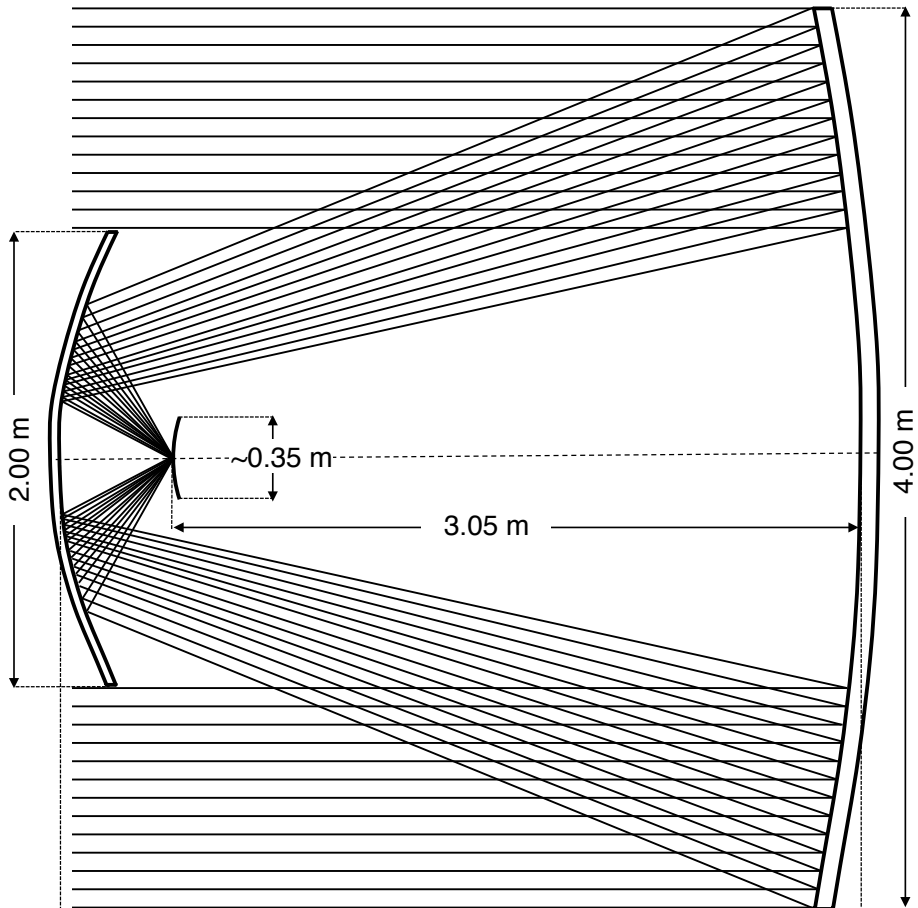


Figure 5: Optical mirror system of the GCT telescope. A primary(4 m)-secondary(2 m) mirror optics system focuses the light onto a 0.35 m camera focal plane.

341 number of SST telescopes at the southern site is sub-optimal.
 342 The alternative solution is the reduction of the camera plate scale through a dual-mirro design
 343 allowing the use of more affordable photosensors. The optical system of the telescope is com-
 344 plemented with a secondary mirror added to the primary mirror. This shortens the effective
 345 focal length so the focal surface will lie between primary and secondary mirror fig(5). This
 346 optical design is based on the Schwarzschild-Couder design first produced by Karl Schwarzschild
 347 (Schwarzschild, 1905) and later refined by Couder (Couder, 1926) and then adapted for use in
 348 IACTs by Vassiliev and Fegan [10]. With the dual-mirror design optimized for GCT by Blake et
 349 al. [11] the camera plate scale is reduced, allowing the use of more affordable photosensors,
 350 Silicon Photomultipliers (SiPMs) and multi-anode photomultipliertubes (MAPMs) among them,
 351 potentially reducing the cost of each SST.

352 **2.2 Compact High Energy Camera** 353

354 The Compact High Energy Camera, or CHEC (fig(6)) is one of three prototype camera concepts
 355 in development for one of the SST structures within CTA. One camera features 2048 photosen-
 356 sors, building equally many readout channels per camera. The readout is done by so called
 357 TARGET⁸ modules for sampling, digitization and triggering, one of those consists of 4 ASICS⁹
 358 with 16 channels each. The camera houses 32 TARGET modules, one of them responsible for
 359 readout of 64 photosensors. The TARGET modules build the front-end of the integrated elec-
 360 tronics¹⁰ inside the CHEC camera connecting the buffer to the cameras backplane. After the

⁸ TARGET TeV Array Readout with GS/s sampling and Event Trigger

⁹ ASIC Application Specific Integrated Circuit

¹⁰ FEE front end electronics

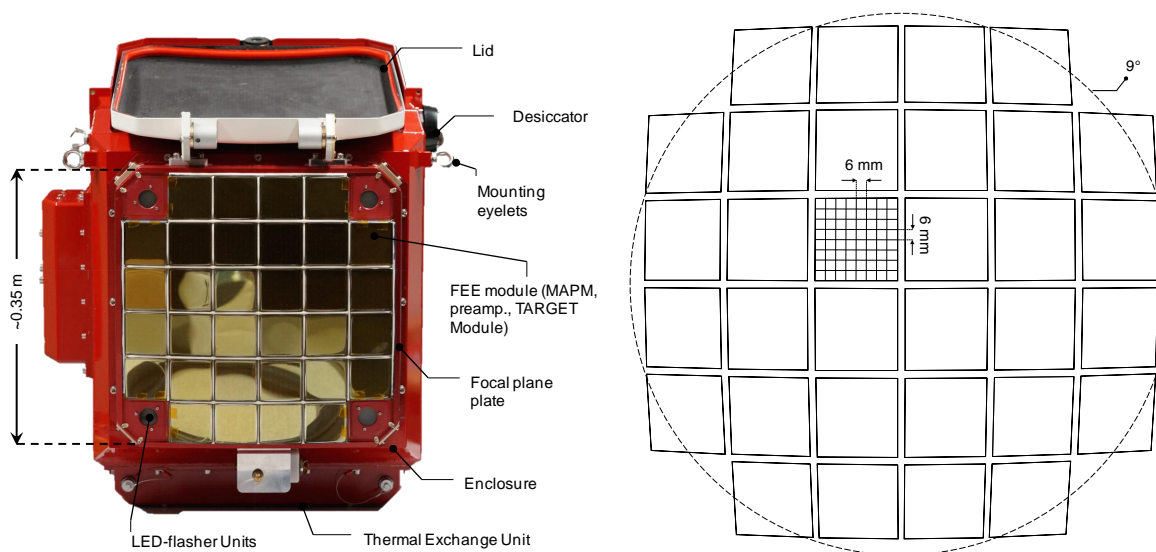


Figure 6: Front view of the CHEC-M prototype (left), view of the camera focal plane. Schematic of the focal plane (right), illustrating the 9° FoV with 6 mm pixels. Pictures from [18]

361 photosensor is triggered the buffer amplifies the signal, that is then send to the ASIC inside the
362 TARGET module, where an analog-to-digital converter and a shaper convert the signal before it
363 is send to the backplane for transfer to the main array hub. Two iterations of the CHEC camera
364 are tested, CHEC-M is the first design based on MAPMs as photosensors and was the initial pro-
365 totype platform all improvements to the electronics are tested on. CHEC-M since then moved to
366 Meudon in Paris and is now mounted on the GCT structure for further testing of the entire GCT
367 prototype. The second iteration of the camera: CHEC-S, based on SiPMs as photosensors is a
368 similar concept, with applied improvements to electronics and mechanical design. The two cam-
369 eras are very similar in shape and can both be mounted on the GCT structure without alterations.

370

371 In order to make an educated choice on the best SiPM candidate to use to populate the camera
372 focal plane of the camera, an in-depth characteristic study on pulse-shape, gain, temperature-
373 dependence, detection efficiency, thermal noise and correlated secondary effects is conducted
374 by multiple groups within the CTA collaboration.

375

376 This work studies the gain, noise from thermal, as well as correlated secondary effects and
377 their temperature dependence.

3 Silicon Photomultipliers

380 Silicon Photomultipliers (SiPMs) are semiconductor photo detectors, that have attracted in-
381 creased attention over the last decade for their possible use in astroparticle physics. The sensor
382 consists of an array of avalanche photo-diodes, typically $\sim 50 \mu\text{m}$ in size. Depending on the
383 pixel-size, one pixel contains several 1000 diodes, hereafter called cells. Each cell is a PN junc-
384 tion (fig(7)) supplied with a reverse bias-voltage above breakdown, which is called operation in
385 Geiger-mode, in analogy to the Geiger counter. In this mode, a photon or thermal excitation will
386 produce an electron-hole pair in the depleted region. Through impact ionization these charge
387 carriers will in turn trigger an avalanche in a cell, which in turn generates a large output pulse
388 typically in the range of several Mega electronvolt. This avalanche is then passively quenched
389 by a resistor to limit the current in the substrate and to reset the cell to a quiet state so it is
390 photosensitive again. The signal of the SiPM is the sum of the signal of all cells, read out over
391 their quenching resistor via a common output.

392

3.1 SiPM characteristics

393 SiPMs posses major advantages over their progenitor, the Photomultipliertubes, or PMT. They
394 are more resistant to mechanical and accidental light-exposure damage through ambient light.
395 Single SiPM cells have a lower power consumption, but more SiPM cells are needed to cover the
396 same space as a PMT. Operating at a much lower bias-voltage, there is no need for high-voltage
397 as in PMTs. They possess a high PDE and are insensitive to magnetic field changes. There is
398 rapid improvement, being a fairly new technology, with new generations every ~ 5 months and
399 decreasing costs per mm^2 . Viewed over all cells of the whole pixel, fluctuations in the gain are

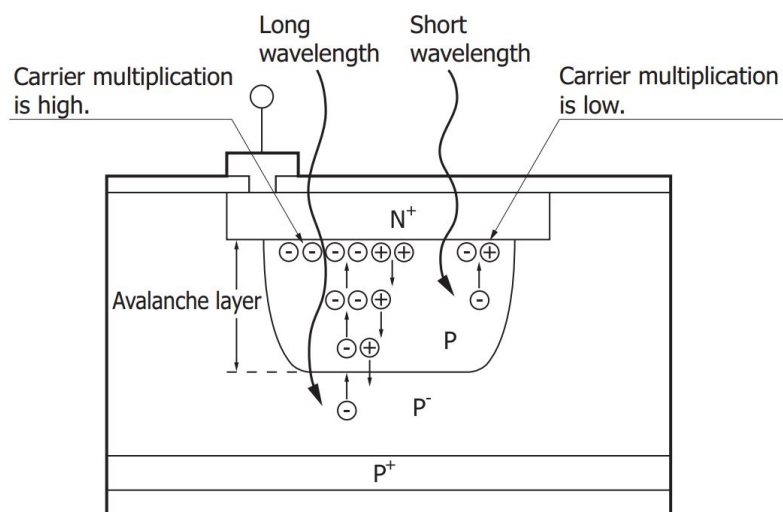


Figure 7: Structure and carrier multiplication through an avalanche inside a SiPM. Picture from [16]

very small. This is because of the uniformity during manufacture and visible in the width and the clear resolution of the p.e. peaks in the pulse area spectrum. See section(E) for examples. MAPMs on the other hand posses larger gain fluctuations, which is due to their structure. These make SiPMs an interesting candidate in astrophysics experiments for both, space- and ground-based telescopes (like IACTs). However SiPMs also posses drawbacks, one of which is their temperature dependence through their gain and Dark Count Rate (DCR). Another source of worry is their Optical Cross Talk (OCT), although manufacturers advance to reduce this source of noise.

410

411 Advantages:

- | | |
|--|---|
| 412 1. Sturdiness | 419 5. No need for HV as in PMTs |
| 413 2. May be exposed to ambient light (observation 420 during bright moonlight periods is 421 possible) | 422 6. High PDE |
| 416 3. Low power consumption ($\leq 50\mu\text{W}/\text{mm}^2$) | 423 7. Insensitivity to magnetic fields |
| 417 4. Low operation voltage (typically ~ 20 424 100 Volts) | 425 8. Being a fairly new technology it is steadily improved, meaning a new generation of SiPMs every 5months |
| | 9. Rapidly decreasing cost per mm^2 |

426 Drawbacks:

427

- 428 1. temperature dependence of gain and DCR
429 2. Noise through OCT
430 3. cost per mm^2 larger than PMTs

431

432 There is a multitude of attributes of SiPMs that are desired by CHEC, and CTA in general, among them is a high enough fill-factor (detector space versus dead space) to guarantee high Photon 433 Detection Efficiency (PDE) (section(3.5)). The PDE quantifies the absolute efficiency of any photon 434 detector to absorb a photon and produce a measurable signal at its output. To achieve a high 435 PDE in the 400 nm regime, the design moves to very thin implantation layers on the surface in 436 order to minimize the absorption of shorter wavelength photons in insensitive areas (fig(??)). 437 Different entry window coatings and avalanche structures explore the capable enhancements in 438 the blue sensitive UV region.

439 The peak of the spectral response of the SiPM is desired to be around the spectral peak of the Cherenkov light at ~ 400 nm and at the same time, must have a fast enough drop to ensure less Night Sky Background (NSB) pick up (fig(8)). The overall noise from thermal and correlated secondary effects, like cross-talk, of the SiPM must be sufficiently below the expected NSB rate at the location (usually around $\sim 20\text{-}80$ MHz[9]). It is common practice to compare those two characteristics directly to showcase the behavior of the PDE versus OCT. A point of low cross-

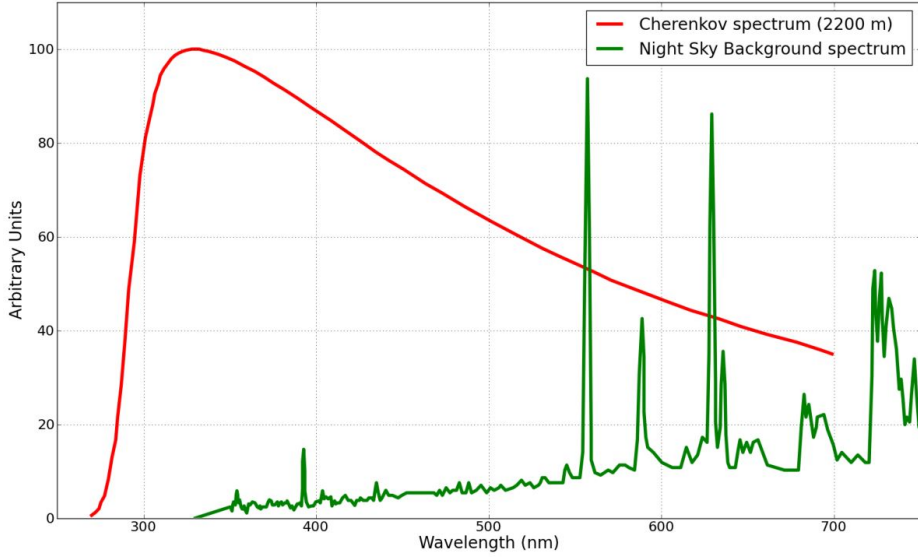


Figure 8: The spectrum of Cherenkov light observed from an extended air shower at 2200m asl. compared to the expected NSB measured in La Palma. Cut-off of the spectrum at wavelengths below ~ 300 nm due to atmospheric absorption. The emission peaks above ~ 550 nm in the NSB spectrum are mostly attributed to atomic oxygen, hydroxide and sodium in the atmosphere. Units on the y-axis are arbitrary because NSB and Cherenkov light vary by different parameters. There is a region between 550 and 650 nm, where the average Cherenkov light spectrum across the focal plane and contributions from the NSB overlap. Image from [9]

446 talk, where the PDE is still at maximum is desired.

447 Another important characteristic is the temperature dependence of the gain. While the CHEC
448 camera is observing, the preferred fluctuation of the gain is $\leq 10\%$. The camera focal plane
449 underlies temperature shifts during operation, which will be slightly countered by cooling the
450 photosensing area. Despite that the focal plane will still be warming up, so a lower gain depen-
451 dence on temperature is desired in order to minimize the gain fluctuations.

452 **3.2 Gain of a Silicon Photomultiplier**

453 The gain of a SiPM measures the internal conversion of a photon incident into a signal at the
454 output. The amplification of the device is expressed as the average number of charge carriers
455 produced. There is no distinction whether the incident was caused by a single original photon
456 or a thermal electron. The gain (M) (eq 1) of a SiPM results from the deposited charge (Q)
457 of the pulse generated from one cell when it detects one photon, divided by the charge per
458 electron (e). The charge deposited per event is proportional to the cells capacitance (C) and
459

460 the supplied over-voltage ($V_{bias} - V_{breakdown}$).[9] This results in the gain (M) in units of total
461 number of charge carriers, usually in the several 10^6 range.

$$M = \frac{Q}{e} \quad (1)$$
$$Q = C \times (V_{bias} - V_{breakdown})$$

462 Estimation can be done via the voltage mean of the 1 p.e. amplitude: (e.g. see figure(25)).
463 For a better understanding, stating the gain in units of mV per photoelectron or mV/p.e. is
464 more suitable, as it gives a direct correlation between detected photoelectron and expected
465 voltage amplitude. Given the very narrow pulse shapes, using the average pulse amplitude and
466 extracting FWHM as a time measure of the total charge flowing during discharge and using the
467 formula (eq 2):

$$Q(p.e.) = C \times (V_{bias} - V_{breakdown}) \quad (2)$$
$$U(p.e.) = \frac{Q(p.e.)}{t(FWHM)} \times 50\text{ohm}$$

468 Resulting in the expected event charge flowing during capacitor discharge. Given the bias-
469 voltage and C as capacitance of one cell and the resistance (50ohm) of the quenching resistor, a
470 conversion factor and the average amplitude per photoelectron can be extracted.

471
472 The gain is obviously higher the larger the cell capacitance or the higher the bias-voltage
473 (eq 1) will be. But increasing the bias-voltage also increases dark counts and crosstalk. The
474 gain is also dependent on the temperature, mainly through the quenching resistor but also from
475 the silicon bulk itself, at a certain bias-voltage decreasing as temperature rises. The quench-
476 ing resistor is affected by a lowering of the electrical conductivity with rising temperature, in
477 accordance to the Wiedemann-Franz law, stating that the ratio of electrical and thermal con-
478 ductivity remains constant. The silicon bulk at rising temperatures underlies increased crystal
479 lattice movement. This impinges charge transport by increasing the probability that carriers
480 might impact on the lattice before the carrier energy has become large enough for continued
481 ionization. In order to counteract this, the electric field must be increased by increasing the sup-
482 plied bias-voltage so ionization is more likely. Doing this has drawbacks as discussed before. For
483 application as a photon detector, keeping the gain constant is an inevitable step, otherwise the
484 shifting gain leads to problems. To do that, either the bias-voltage need to be adjusted to match
485 ambient temperature, leading to problems with varying dark counts and crosstalk. Or the sur-
486 face temperature must be regulated to be kept constant. Although more challenging hardware
487 would be required, the latter option has obvious advantages, keeping dark counts and crosstalk
488 and more important the gain constant by simply regulating the surface temperature.

489 Taking into account equation 1, it appears that the breakdown-voltage can be estimated from
490 the zero-crossing of a linear extrapolation of the gain at every bias-voltage per temperature. By
491 doing this a linear breakdown-voltage dependence of the temperature can be observed. See
492 section(F)
493 When parametrized over over-voltage, the gain is essentially temperature independent.
494 For gain measurements see section(6).

495 **3.3 Thermally induced dark counts**
496

497 Inside the SiPMs depleted region a dark pulse originates from thermal excitation of an electron
498 to the conduction band. Without an event photon present to trigger the avalanche, it is still
499 indistinguishable from a photoelectron pulse. These thermally generated carriers are observed
500 along with the signal from a real photoelectron, presenting an irreducible source of noise. The
501 number of dark pulses observed is referred to as dark counts ant the number per second as
502 the Dark Count Rate (DCR). For applications that need to operate in an environment with low
503 noise, those dark counts are a concern. In IACT application of SiPMs however, this is only a
504 minor problem, since IACTs operate in a naturally noisy environment. Even though sky dark-
505 ness is one of the prime criteria of the proposed site selections for CTA, the surrounding NSB at
506 the most darkest side in Chile will still exceed any random noise in the detector. The pollution
507 of those NSB photons is unavoidable noise and will essentially limit the low energy resolution
508 of the telescope to the NSB rate. As long as any random noise, being dark counts or other, is
509 significantly below the NSB rate, it will not affect the telescopes performance.

510 Telescope performance simulations of the Schwarzschild-Couder MST of CTA at the site of
511 Chile showed a rate of $\sim 20 - 80$ MHz per pixel for one of the older SiPM iterations from
512 Hamamatsu.[9] This is purely for NSB photons and pixels with a size of 6×6 mm², the cov-
513 ered range originates from differences in illumination level of the night sky by galactic- and
514 extragalactic-fields.

515 **3.4 Avalanche-induced secondary effects**
516

517 An avalanche originating from the primary cell can sometimes, either directly or by reflection,
518 propagate outside the cell and trigger an avalanche almost simultaneously in a secondary cell.
519 This will, unless accounted for, degrade the SiPMs photon counting resolution, since the sig-
520 nal will be a merge of cross-talk cells and real incident cells. This effect is referred to as the
521 OCT, since it is conveyed via secondary photons generated in the primary avalanche. Afterpuls-
522 ing also falls under this category, with the main difference to cross-talk being that the carrier
523 triggers a secondary avalanche in the primary cell, basically generating a parasitic pulse inside
524 the previously fired cell. Contained in a single cell, afterpulsing increases the measured charge
525 registered for an incident photon. The difference in arrival time of the secondary avalanche
526 distinguishes different components comprising the cross-talk and afterpulsing. Those secondary

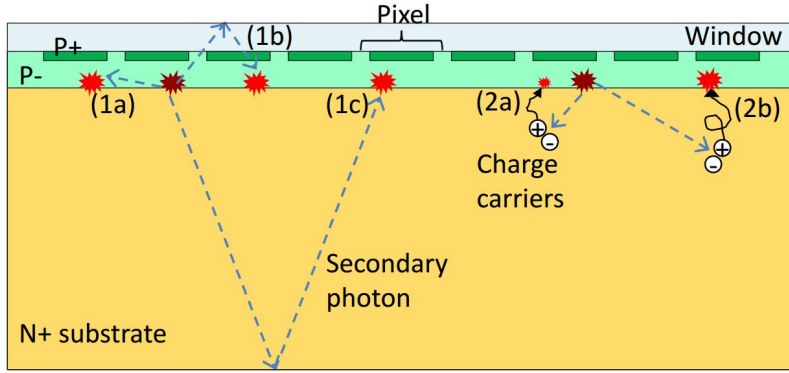


Figure 9: Secondary effects (bright red) caused by primary avalanches (dark red) in a Silicon Photomultiplier. In this work a single pixel, in this figure, is referred to as a cell (see section(3)). Everything labeled under 1 is associated with prompt cross-talk, afterpulsing labeled as 2a, and delayed cross-talk labeled as 2b. Image adapted from [13]

avalanches can again emit photons, that can trigger secondary avalanches themselves, leading to high amplitudes, even in dark conditions. Cross-talk is dependent on the ability of the secondary photons to reach a neighboring cell. This means, that an increase in cell-size and therefore cell-area should directly correlate with the OCT of a pixel. The OCT dependency on the cellsize was tested and can be found in section(C).

Figure(9) shows different physical processes causing secondary effects in SiPMs based on their delay time. Cause of the delay time is the dependence on the penetration depth of the incident photon, or the region the dark count generated, and the diffusion time inside the substrate. At long delay times of up to 70ns afterpulsing and cross-talk are not distinguishable.[13] The prompt OCT happens basically simultaneous to the primary avalanche, since it is unaffected by the primary cells recovery time and is labeled 1 in Figure(9). It is either triggered by the secondary photon directly (1a) reaching the neighboring cell, or after first reflecting on the surface layer (1b) or the bottom surface (1c). If the cross-talk avalanche delay time is shorter than the detection resolution, the difference in signal between an OCT event or an incident photon being detected, is not observable.

Time delayed OCT is caused by a carrier generated in the non-depleted substrate diffusing to a neighboring cell and triggering an avalanche in the depleted region (2b). If the carrier stays in the primary cell, the triggered avalanche is labeled afterpulsing (2a) and will have a lower amplitude, due to the cell not being recovered yet. The delay time is influenced by how deep the carriers are being trapped in the substrate, the time they need to diffuse to the surface, and also distinguished by traps with different lifetimes.

This is very important in IACT performance, since this effect gives random NSB and dark count photons the ability to rise to larger amplitudes. The consequent need to raise the trigger threshold to counteract the resulting rising accidental-triggerate has a negative impact on the low

551 energy resolution of the telescope.

552

553 Parametrized with over-voltage, the secondary avalanche effects are temperature indepen-
554 dent, for OCT measurements see section(6).

555 3.5 Photon Detection Efficiency

$$PDE = \frac{N_{detected\ photons}}{N_{total\ photons}} \quad (3)$$

557 The PDE is the probability of a detector to absorb an incoming photon and produce a mea-
558 surable signal at its output, and depends on a number of factors. First the photon must enter
559 the depleted region via transmission through the surface of bare silicon, which has a reflectivity
560 of 30%. However, the transmission probability can be improved by coating the surface with
561 a substrate with adequate thickness and a refraction index between air $\eta_{air} = 1.$ and silicon
562 $\eta_{silicon} = 3.4.$ Devices presented in this work are coated with a silicon resin and glass. The
563 coating also has the added benefit of insulating and protecting the cells against environmental
564 influence. A possible negative effect of coating is an increase in prompt cross-talk and a larger
565 dependency of the overall cross-talk on the cellsize.[20] The second factor is quantum efficiency,
566 describing how susceptible the depleted region is to photons exciting electrons from the valence
567 band to the conduction band. This is also referred to as spectral response of a detector to re-
568 flect the wavelength dependence of a detector and makes the PDE wavelength dependent. The
569 over-voltage dependency of the PDE is conveyed by the third factor, the avalanche probability.
570 It depends on the electric field present, and thus on the applied over-voltage. The last factor is
571 the fill-factor: the more the surface area of the detector is covered with active-area cells and the
572 less dead-area exists between cells the higher the fill-factor is.

573 The PDE is commonly measured by illumination of the pixel and a calibrated reference photo-
574 diode with a flashing light source, and determining the average number of photons hitting the
575 photosensor during a light pulse.

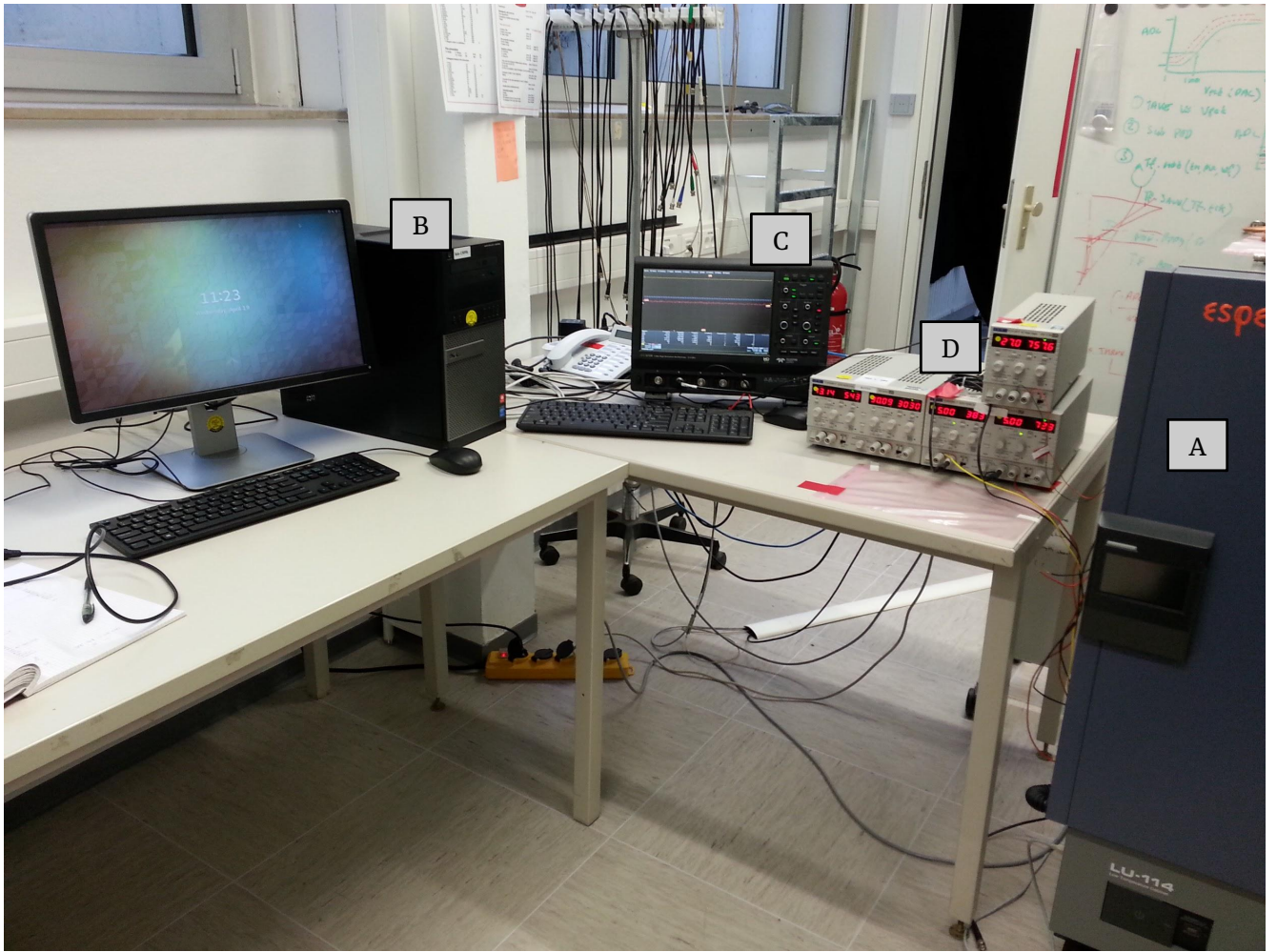


Figure 10: Outside view of the teststand with the ESPEC LU-114 thermal chamber (A), the Lab-PC (B), the Lecroy HD6104 oscilloscope (C) and the TTi power supplies (D).

576
577

4 Experimental Setup

578 The experimental setup in general is designed to house a variety of SiPM devices. Over the
 579 course of this work, 5 different types of SiPMs were mounted on the setup and evaluated. It
 580 involves a thermal chamber fig(12)(A) for temperature regulation which proved light tight and
 581 thus also serves as a dark box, to prevent any stray light to reach the SiPMs surface. The thermal
 582 chamber in question is a LU-114 constant climate cabinet from ESPEC with a programmable in-
 583 terface for remote control. The chamber is able to raise and lower the inside temperature with a
 584 $\pm 0.5^\circ\text{C}$ accuracy, direct measurements of the SiPMs surface with a temperature probe confirmed
 585 this. In the absence of light tests, heating of the SiPM surface through the dark current proved
 586 no concern.

587 Depending if the SiPM fig(12)(A1) in testing is pre-manufactured on a test-array or supplied
 588 as a standalone chip, it is either mounted directly on a mechanical arm inside the chamber
 589 in the former case, or in the latter the mechanical arm supports a specifically designed PCB

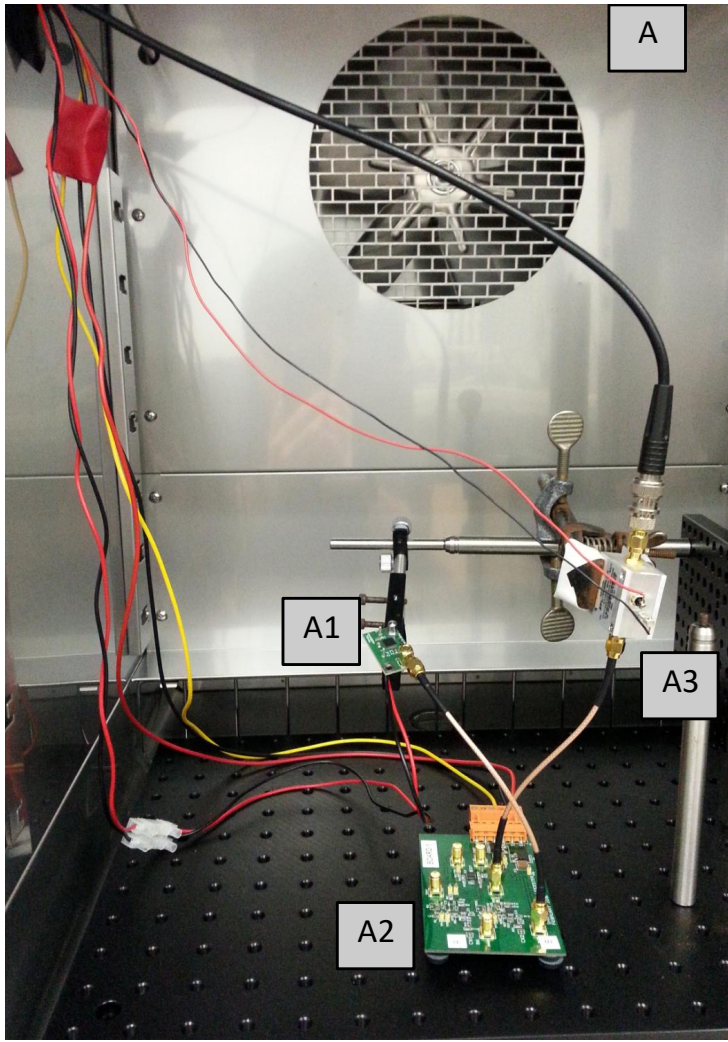


Figure 11: Inside view of the thermal chamber (A), with the SiPM (A1), the shaping electronics (A2) and the MiniCircuits PreAMP (A3). Signal throughput in the top left corner.

590 connecting to the device. Via the mount, bias-voltage is supplied and signal is transferred to
 591 the shaper fig(12)(A2). In some cases the output signals amplitude is to low to trigger the
 592 oscilloscope, therefore amplification is needed. I used a ZFL-1000-LN+ amplifier from MiniCir-
 593 cuits fig(12)(A3) supplied with different voltages depending on the tested device to amplify the
 594 shaped signal.

595

596 Data acquisition in the Laboratory is realized by a Lab-PC fig(12)(B), that forms the central
 597 control station for multiple pieces of equipment. It is connected to the oscilloscope fig(12)(C),
 598 which records the waveforms of the device in testing, and then sends the data back to the PC
 599 via Ethernet. The oscilloscope is a Lecroy HDO6104 1GHz HS Oscilloscope capable of 2.5 GS/s.

600

601 The power supplies fig(12)(D) control the bias-voltage of the SiPMs, ramping of the bias-voltage
 602 is controlled by the PC. Lastly the thermal chamber is connected to the Lab-PC, where the data

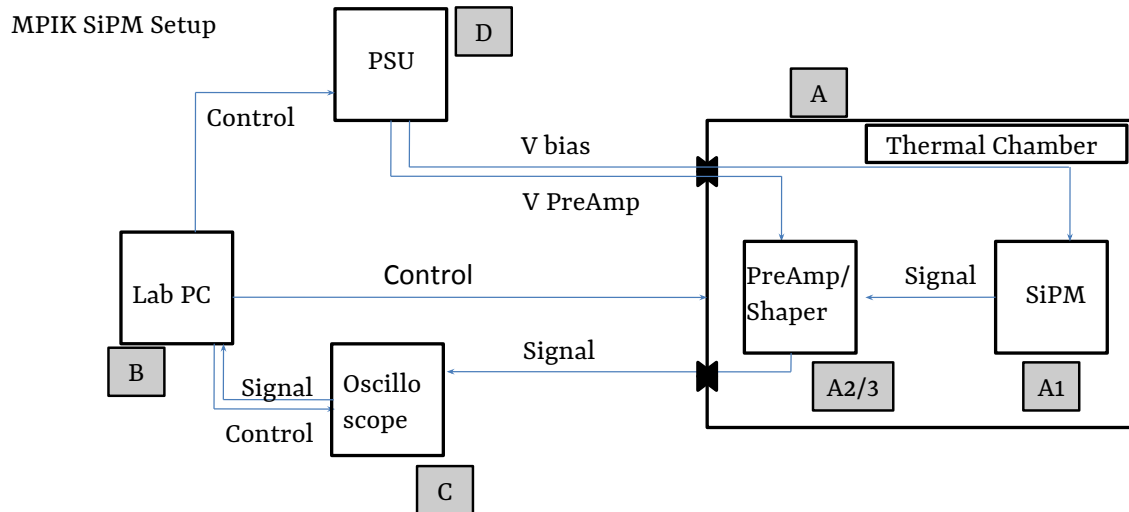


Figure 12: Experimental setup scheme, Annotations see text

603 acquisition script controls the temperature, and continuously rechecks it during temperature
 604 ramps. Signal transfer from the shaper to the oscilloscope is via a throughput on the side. All
 605 equipment is connected via ethernet, plugged into a common hub, to form a local network.
 606 While the temperature of the thermal chamber is ramping from the previous to the next set-
 607 point, the data is send to the Lab-PC.

608

609

610 Temperature regulation is an issue in the teststand, as there is no way of controlling the SiPMs
 611 surface temperature. In dark conditions however, without conducting illumination tests, the
 612 shift in temperature on the SiPMs surface is only minimal. See section(F) for the breakdown-
 613 voltage dependence on temperature. Checking the surface temperature of all devices with a
 614 temperature probe during testing showed minimal rising temperatures. So the influence of the
 615 temperature on the breakdown-voltage is only of minor concern. However, once illumination
 616 tests begin, the rising temperature on the SiPMs surface will no longer be negligible and the
 617 temperature must be regulated, either by cooling of the surface or including the temperature
 618 parameter.

619

620 There is also the issue of the saturation of the input of the oscilloscope making the higher
 621 over-voltage range difficult to reach, due to potential multi p.e. pulses being amplified and
 622 reaching the input. This is possible because of the difference in amplitude between a 1 p.e. and
 623 a multi p.e. event and the electronic noise, forcing a high resolution of the amplitude in the
 624 oscilloscope. Different couplings were tried to circumvent the problem, to no avail.

625



Figure 13: The shaped and unshaped pulse from a pulse generator emulating the output of the front-end buffer of the CHEC-S SiPM. The unshaped pulse in yellow and negative, due to the buffer-output. The shaped pulse is flipped to the negative through the electronics in green. Image credit [21]

626 The shaper consists of two stages, the main
 627 components are an Op-Amp amplifier serving
 628 as an input buffer followed by a zero pole can-
 629 celation circuit for pulse shaping and is com-
 630 monly used in photon-counting applications.
 631 A zero pole cancellation circuit is basically a
 632 RC circuit eq(4) (C_Z, R_0) suppressing the high
 633 frequencies to narrow the pulses from the
 634 usual ~ 50 ns to ~ 10 ns, using a high-pass
 635 filter with a tunable time constant, through
 636 f_C which gives control over the frequency re-
 637 sponse of the circuit.[22]

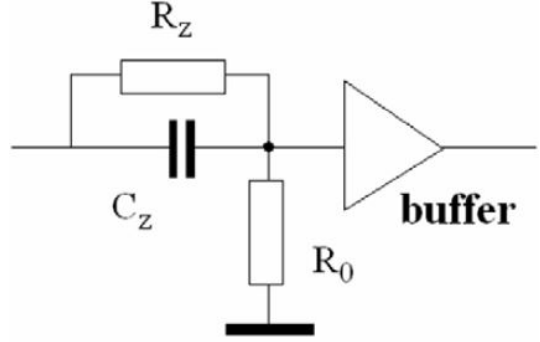


Figure 14: A Zero Pole cancellation circuit com-
 monly used in photon counting applica-
 tions. Taken from [22]

$$R_0 \times C_Z = 1/(2\pi \times f_C) \quad (4)$$

638 In Figure(13)[21], the shaped and unshaped pulse is shown, the negative amplitude (yellow)
 639 corresponds to the unshaped signal mimicked by a function generator to emulate the output
 640 of the front-end buffer of the CHEC-S SiPM. These tests correspond to an initial design of the
 641 shaper and do not correspond to the final setup.

642

643

644

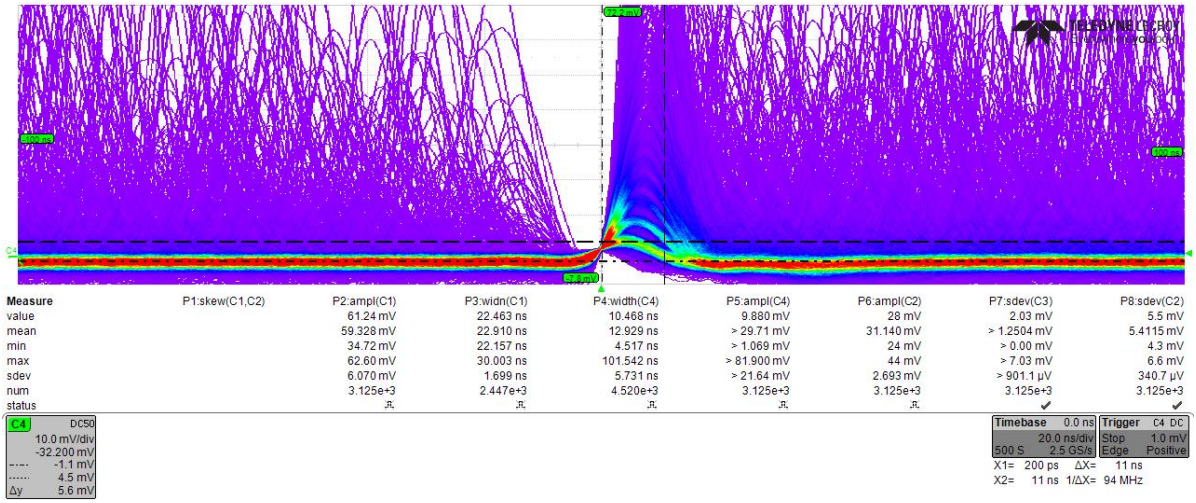


Figure 15: Persistence figure of the shaped pulse after adapting the electronics to a preferable pulse shape. In the center, a row of pulses with rising quantified amplitudes is visible. These are the multiple N p.e. pulses, differing by ~ 5 mV. The purple area off-center is due to delayed cross-talk and after-pulsing. Image credit [21]

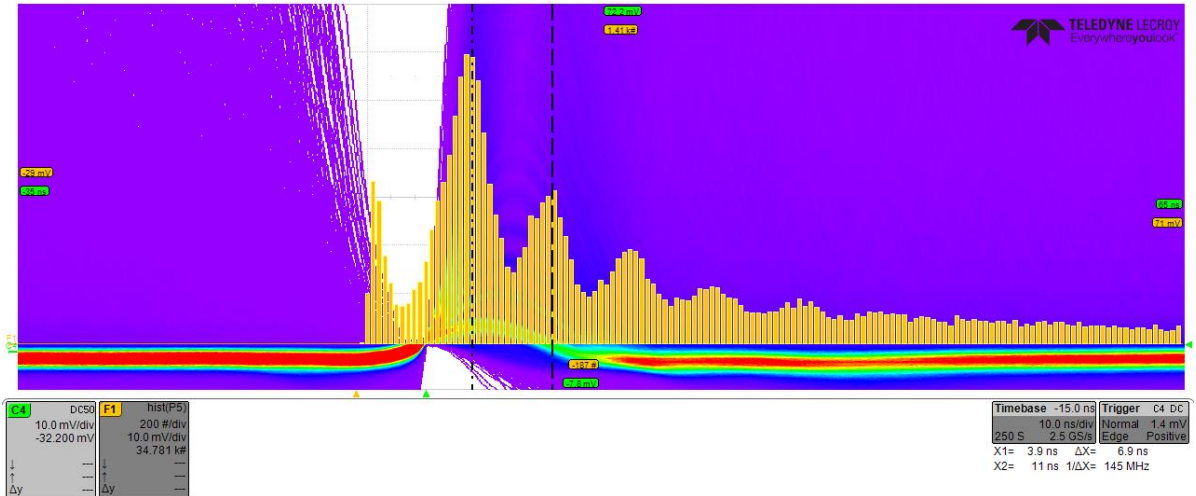


Figure 16: An oscilloscope based pulse height spectrum in the same scheme as the persistence plot fig(15). The distance between the peak maxima delivers an estimation of the gain of the SiPM at this bias-voltage. Image credit [21]

645 The shaper board contains tunable capacitors (C9) and resistors (R20) (see schematic in
646 section(G)), that can be tuned and optimized for ideal pulse layout. The green pulse in
647 figure(13) shows the output after shaping, with a width of FWHM of 9 ns. The output pulse has
648 some ringing after the main pulse.

649
650 After tweaking the tunable electronics on the shaper to a preferable pulse shape, clear quan-
651 tified single p.e. peaks are visible in a persistence plot. fig(15). The peaks have an amplitude of
652 ~ 5 mV/p.e., from this and from the following, a gain estimate for the peak finding threshold in

653 the analysis can be made. With the same configuration a gain estimate at different bias-voltages
654 of the SiPM is possible through an on-oscilloscope pulse height spectrum fig(16). The distance in
655 peak maxima is a reference to the gain of the SiPM, in the case of figure(16) close to ~ 5 mV/p.e..

656

657 This chain of shaper modification is done for every single SiPM cell from Hamamatsu Photo-
658 tonics K.K. tested in this work (three in total) as they arrived as a single unmounted device,
659 in need of shaping and amplification. The device from SensL is premounted on a test array,
660 preshaped and only externally amplified.

661 5 Data Analysis

663 The analysis of the SiPM waveforms is done exclusively in python following the sequence:

664

- 665 1. data conversion
- 666 2. pedestal subtraction
- 667 3. peak detection
- 668 4. gain extraction
- 669 5. calculation

670 The waveform data, after being transferred to a separate PC, is analyzed offline. The goal is
671 to extract event-data from the waveforms in order to produce pulse-area spectra for every bias-
672 voltage at every temperature. To that end, the pedestal of the electronic noise must be found and
673 subtracted from the data. After that, event-pulses are detected and integrated. This generates
674 a list of pulse-areas, which is in turn used to fill a pulse-area histogram. To this pulse-area
675 histogram, a model is fitted from which the gain can be extracted. Due to the linear behavior
676 of the gain with rising bias-voltage, a regression line is fitted, from which the DCR and the OCT
677 are calculated using the original pulse-area histogram.

678 5.1 Tracefile Conversion

680 The oscilloscope produces the waveform data in its intrinsic data format, called a trace with
681 the data suffix trc in binary. A trace file contains a header and two binary lists, an amplitude
682 based on the oscilloscopes voltage-range and offset, and a list of the same length containing the
683 associated event-time, based on the time-range and horizontal offset. The first step is therefore
684 a conversion of the amplitude and associated event-time of all segments of a waveform trace
685 file into two lists of floats.

686 5.2 Pedestal Subtraction

688 A single waveform from the oscilloscope is
689 anticipated to be uncentered fig(17)(grey), it
690 will be slightly above or below zero, depending
691 on the device setup (some devices pro-
692 duce inverted signals). The signal is mixed
693 with electronic noise when it is observed
694 and forms a pedestal, shifting the mean of
695 the waveform from its original position to
696 zero. Pedestal subtraction removes this av-
697 erage noise.

698 The first step of the process is reading in the
699 uncentered waveform fig(17)(grey) and cal-
700 culating an initial mean(mean0), expected to
701 be slightly higher than the actual mean of the
702 noise, due to the presence of event-pulses.
703 The waveform is then shifted to about zero,

704 by subtracting the mean0. A second mean of the now nearly centered waveform is taken
705 (mean1). Now a new, same-sized array is formed and filled with the data from the wave-
706 form that is smaller than mean1, this represents the negative part of the noise. The data larger
707 than mean1, the positive noise, is also filled into the array, but is negative-signed. This cre-
708 ates an array of the waveform centered around zero and, above the mean1, folded towards the
709 negative. It proved reliably, that calculating the root-mean-square of this helper-array is a solid
710 possibility of stripping the waveform of event-peaks. Taking the root-mean-square with a factor
711 3 of the helper-array, a cut is now applied to the waveform on both, the positive and negative
712 side. In that fashion, the remnant is the waveform between the positive and the negative root-
713 mean-square and is now called a peakless-signal, representing the noise of the waveform.
714 Pedestal subtraction is done by calculating the mean of this peakless signal and subtracting
715 it from the waveform. After that, the peakless signal is also smoothed by convolving it with
716 a wide-windowed gaussian and subtracted from the waveform to eliminate any slow moving
717 noise, the resulting waveform is called "Filtered Signal 1" fig(17)(blue).

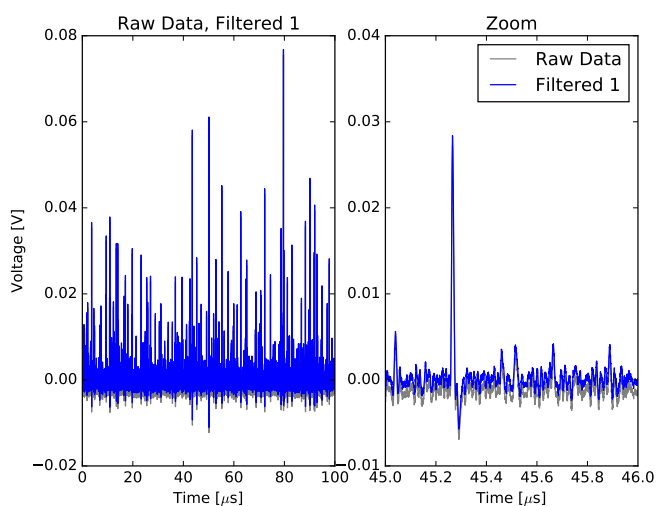


Figure 17: Raw, real data from a HPK SiPM in grey, in blue the pedestal subtracted and smoothed "Filtered Signal 1"

718

5.3 Peak Detection

719 Peak detection exploits the fact, that the first
720 derivative of an event-peak will cross zero
721 into the negative at the time of the peak max-
722 imum. The presence of random noise in the
723 signal however will lead to many false de-
724 tections. Therefore, before the detection of
725 the event-peaks, the waveform fig(18)(grey)
726 is smoothed with a narrow-window gaussian
727 with a width of about the FWHM of the de-
728 vices characteristic event-pulse, in order to at-
729 tenuate non-event peaks fig(18)(blue). After
730 the first derivative of the signal is calculated,
731 which in python is a fast process if using ar-
732 rays, a number of parameters decide the va-
733 lidity of the detected peaks. Most important
734 parameters are a certain predetermined mini-
735 mum amplitude, called the amplitude thresh-
736 old or: minimum peak height. This is determined from initial examination of pulses on the
737 oscilloscope and entered as a parameter to the analysis chain, but could later be calculated
738 based on the noise level. The second important parameter defining validity is the minimum
739 peak distance, which defines how close two events can occur after another. The value is deter-
740 mined by the FWHM of the device in testing, which is expected to be sensible enough to resolve
741 two events happening close after another.
742 While peak detection is done with help of "Filtered Signal 2", the integration of the pulses uses
743 "Filtered Signal 1", as to not falsify the data, because "Filtered Signal 2" is subject to attenuation
744 during the smoothing. The difference in amplitude can be seen in figure(18).
745
746 The peak detection algorithm cannot distinguish between instantaneous and delayed Opti-
747 cal Cross Talk, but nonetheless, due to the fact, that the signal data is taken over many
748 micro-seconds, all events are detected, independent of their source. On the other hand, this
749 also means, that it is possible for two events to happen at the same time, for example a real
750 photoelectron-event coinciding with delayed OCT or two simultaneous dark events being misin-
751 terpreted as one dark event + prompt cross-talk. This cannot be distinguished and will lead to
752 a slight shift of the amplitude, due to the mostly lower amplitude of afterpulsing and cross-talk
753 events.
754

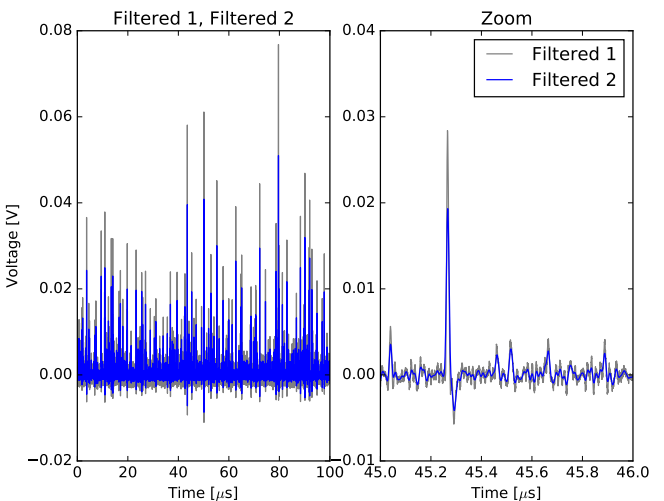


Figure 18: "Filtered Signal 1" in grey before smoothing with a narrow gaussian to generate "Filtered Signal 2" in blue, which is used for peak finding.

755
756

5.4 Gain Extraction

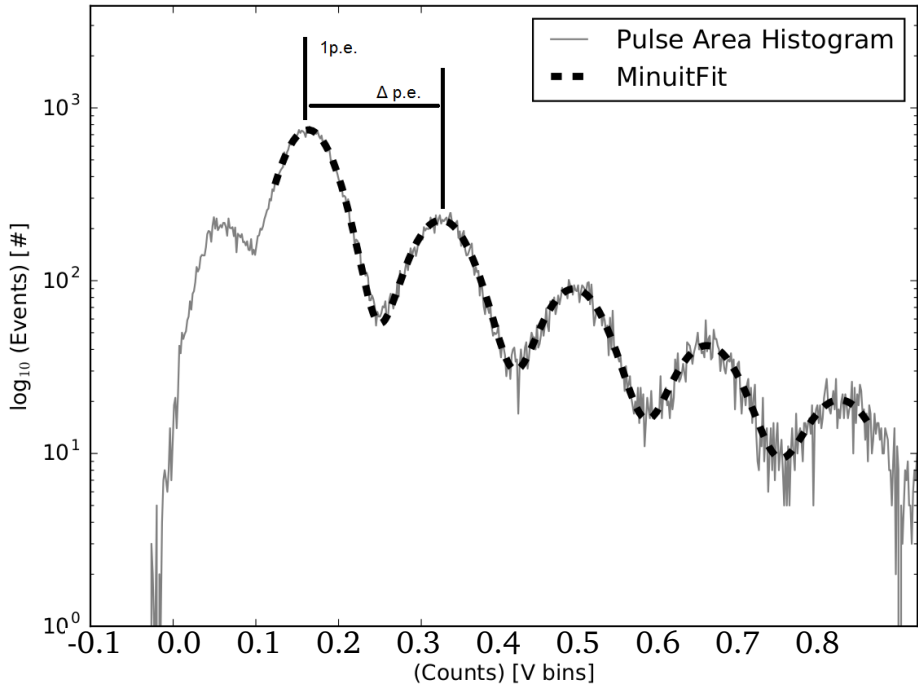


Figure 19: Pulse Area Histogram of a HPK S12642 with 1p.e. and Δ p.e. positions. Multi gaussian fitted function eq(5) as black dashed line.

757 The detected peaks are integrated with “Filtered Signal 1” and with a window extending
 758 symmetrically from the peak maximum, the width is chosen as slightly wider than the peaks
 759 FWHM. The generated list of peak areas is generating a peak area histogram (see section(E)).
 760 The amplitude, position and sigma of the first p.e. peak is calculated and fitted with a single
 761 gaussian using pythons scipy curvefit, the fitted parameters serve as a first guess. After the first
 762 guess parameters are determined, the histogram is fitted with a function of multiple gaussians
 763 eq(5) using iMinuit in python, seen in figure(19). To determine the number of gaussians to
 764 fit, another function checks the viability of each N p.e. peak, among the checked parameters is
 765 the ratio in height to the 1 p.e. peak and the amplitude of the checked Nth p.e. peak in the
 766 histogramm. The fit function $F(x)$ is a function of multiple gaussians with equal spacing eq(5).
 767 N is the multiplicity of the function or range the fit function is to be applied. A is the Amplitude
 768 of the Nth p.e. peak with σ , χ_0 is the x-position of the 1 p.e. peak, Δx is the p.e. spacing
 769 distance.

$$F(x) = (N \times \left[A \times e^{\frac{-(x-(\chi_0+N \times \Delta x))^2}{2 \times \sigma^2}} \right]) \quad (5)$$

770 Two parameters are extracted from the fit to the peak area histogram. The first χ_0 , the posi-
 771 tion of the 1p.e. peak is the position of the maximum of the first peak in the histogram, and the

position of corresponding multiple p.e. events should be integral factors of the 1p.e. position. This proved to not be the case for some devices, the suspected source of this error is a pedestal generated during the peak integration. For a more detailed study of the effect of the integration window see section(5.6).

776

A second parameter is extracted from the peak area histogram to deal with this problem, which is the distance between N p.e. peak maxima of the histogram, labeled Δ p.e. . This distance defines the gain, as it gives a measure of the difference of the generated signal of a 1p.e. signal and a 2p.e. signal. The apparent pedestal of the pulse area histogram makes extraction of the two parameters necessary in order to calculate the DCR and the OCT.

790

The gain of a SiPM has a linear dependence of the supplied bias-voltage. Given that the bias-voltage range is deliberately chosen such

that the over-voltage ranges from about 1V growing upwards, the range of linearity only starts at around the point of operation given by the manufacturer of the device. At the higher end of the bias-voltage range the behaviour usually starts to divert from the linearity. In order to get an estimation of the gain over a large range, both previously extracted parameters, the 1p.e. peak and the distance Δ p.e. are fitted with a linear regression line. The fit assumes linearity utilizing weighted least squares inherited from pythons statsmodels package. For the fit, the data, where more than two gaussians are fitted to the peak area histogram has a stronger weight.

801

Plotting both extracted parameters, as well as their respective regression lines versus bias-voltage, as in fig(20), shows the difference between the two parameters. Comparing the manufacturer supplied breakdown-voltage from the datasheet for all devices showed, that the zero-crossing of the 1 p.e. regression line is more consistent with datasheet values, in contrast to the zero-crossing of Δ p.e. , which lies slightly higher. The over-voltage, corresponding to the set bias-voltage at any given temperature is calculated from this breakdown-voltage.

DCR and OCT are calculated utilizing 1p.e. position and Δ p.e. derived from the regression line. Both values are applied, in the calculation, to the peak area histogram with the DCR of a

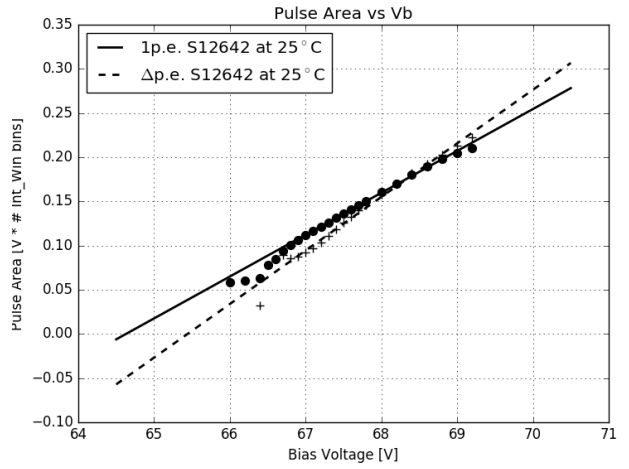


Figure 20: 1p.e. position and Δ p.e. extracted from the Pulse Area histogram at every bias-voltage for HPK S12642 with their respective regression lines.

810 SiPM being defined as all events exceeding 0.5 p.e. in amplitude $N_{events(\geq 0.5p.e.)}$ occurring over
811 the experiment time $t_{experiment}$ eq(6). Included in the measurement are thermally generated
812 dark counts, as well as delayed cross-talk and afterpulsing with only a minor contribution.

$$DCR = \frac{N_{events(\geq 0.5p.e.)}}{t_{experiment}} \quad (6)$$

813 The OCT of a SiPM is defined as all events exceeding 1.5 p.e. in amplitude [$N_{events(\geq 1.5p.e.)}$]
814 devided by all events exceeding 0.5 p.e. in amplitude [$N_{events(\geq 0.5p.e.)}$] eq 7. It scales with the
815 number of photons produced inside an avalanche, as well as the probability of these photons to
816 trigger a neighboring cell

$$OCT = \frac{N_{events(\geq 1.5p.e.)}}{N_{events(\geq 0.5p.e.)}}. \quad (7)$$

817 5.5 Analysis improvements

818
819 For one, at higher DCR the multi hit coincidence of two 1p.e. pulses rises and together with the
820 resolution of the waveforms this could lead to the OCT being calculated high (see section(K)).
821 Changing the determination of the threshold from being measured with an oscilloscope and
822 added as a parameter by hand, to being determined on a per-waveform basis before peak-
823 finding could improve the lower over-voltage resolution depending on electronic noise.
824 The source of the 'pedestal' in the pulse area spectra is suspected to originate from the pulse
825 integration, but this is not certain.

826 5.6 Data Challenges

828 5.6.1 The influence of the minimum peak distance

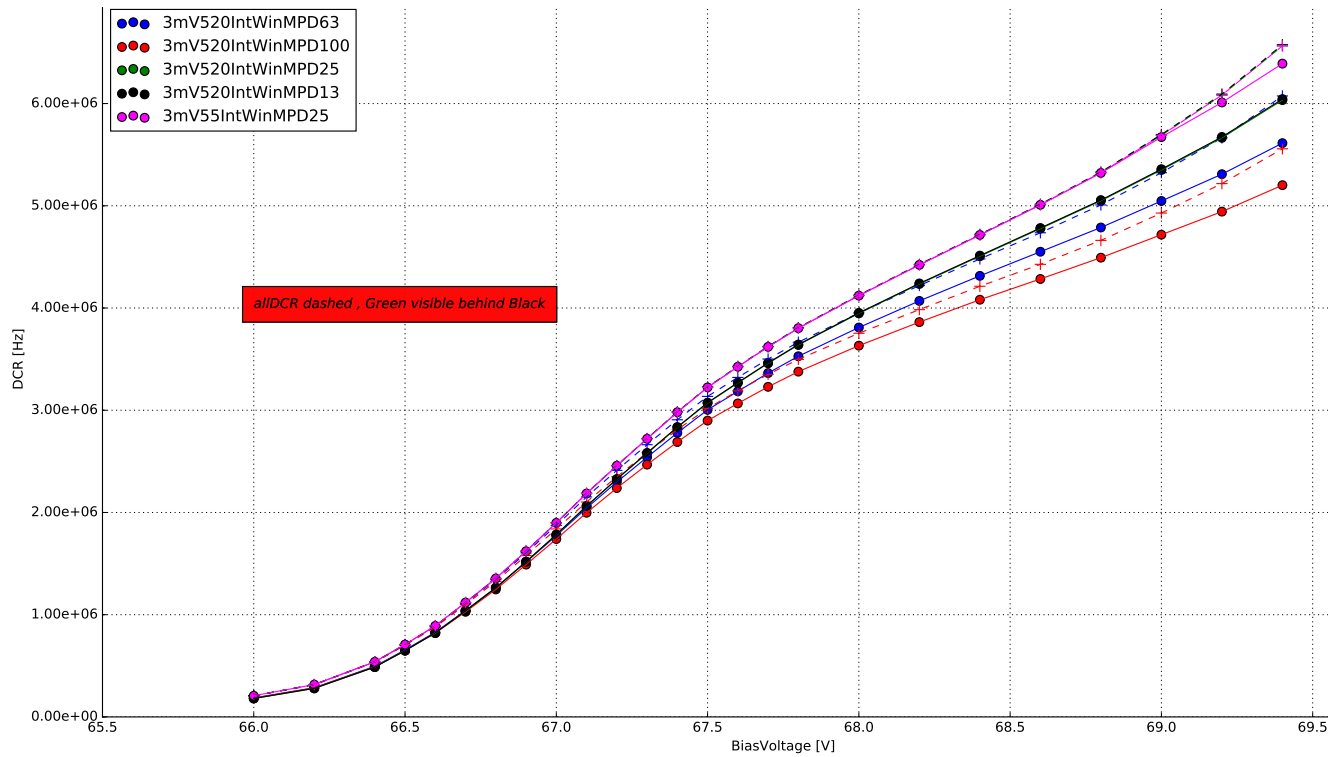


Figure 21: The difference between 4 minimum peak distance windows, in time-bins, during the peak detection. The dashed lines are the DCR considering all recorded events, forming an upper limit. In pink, the effect of a different integration window is shown.

830 The influence of the minimum peak distance is shown in fig(21) . Based on their bin-
831 width, four different peak-distance-windows are tested. With the oscilloscopes sampling rate
832 of 2.5 GS/s, the windows of 100, 63, 25 and 13 time-bins, correspond to 40, 25, 10, 5 ns win-
833 dows respectively. With a event pulse FWHM of \sim 10 ns, setting the minimum peak distance to
834 100 bins, resulting in a 40ns window is visibly to large, as the algorithm will skip over valid data
835 fig(21)(red). After an event is detected, skipping over 40ns worth of data will result in errors
836 of the DCR, since the calculation uses the complete experiment time. Therefore a more reliable
837 distance window must be chosen. The second window of 25 ns was the next approach, orig-
838 inating from the length of the pulse-tail fig(21)(blue). This would lead to no detected events
839 overlapping with the tail of one previously detected, resulting in a sharper pulse-area spectrum.
840 Compared to a window of approximately the pulse FWHM, the previously discussed window
841 would still lead to lost event-data. Since the sharpness of the pulse-area spectrum is already
842 sufficient, a window around the pulse FWHM was chosen as reference for all measured devices

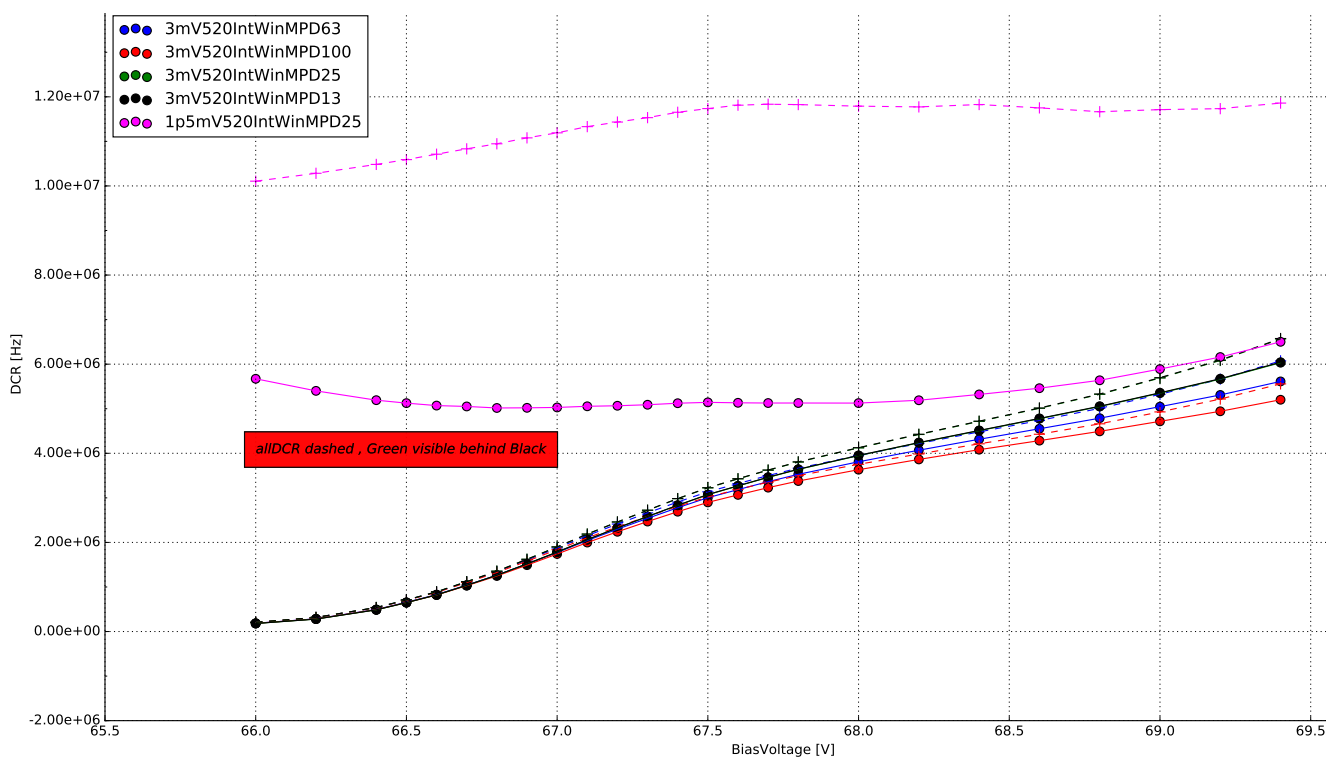


Figure 22: The difference between 4 minimum peak distance windows, in time-bins, during the peak detection. In pink, the effect of a lowered peak detection threshold is shown. The dashed lines are the DCR considering all recorded events, forming an upper limit.

843 fig(21)(green, obscured by black). Going lower than the pulse FWHM showed no improvement
 844 fig(21)(black).

845 5.6.2 The influence of the integration window

846
 847 Figure(21) also shows the influence of the size and shape of the integration window on the
 848 DCR. The influence of the chosen integration window is most visible in their respective pulse
 849 area spectra. Choosing a narrow, symmetrical integration window of 5ns left and right of the
 850 peak maxima, the noise peak, or zero-peak, is much more prominent compared to the pulse
 851 area spectrum of a symmetrical 10 ns window. This leads to errors in the multi-gauss fitting
 852 step, or the fitting will fail altogether. An asymmetrical integration window of 5ns left, 20ns
 853 right, to capture the influence of the pulse-tail proved, at first, to be the best solution as there
 854 was no visible zero-peak present. The low amplitude pulses are averaged out by the extended
 855 integration window to the right of the pulse-maximum. The downside of the asymmetrical
 856 window is the shifting of the pulse area spectrum and the fact, that the N p.e. peaks get blurred.
 857 The next step was widening the window on both sides. This proved the best solution, since
 858 there is no zero-peak visible and the N p.e. peaks are gaussian shaped. Please see section(D)
 859 for the respective plots of pulse area spectra of the different windows.

860 5.6.3 The influence of the peak detection threshold

862 Choosing an adequate peak-finding threshold is a crucial step. Lowering of the threshold to
863 ~ 0.5 p.e. will cause the peak finding algorithm to misinterpret a lot of noise peaks as actual
864 dark incidents. This, of course, leads to errors in the gain extraction and even if a gain regression
865 line can be extracted, the resulting DCR and OCT will be incorrect. Figure(22)(pink), shows the
866 effect a low peak finding threshold has on the DCR.

6 Results

6.1 SiPM devices for CTA

Manufacturer	pixel size [mm]	cell size [μm]	coating	connection	specifics	pre-Amp
HPK S12642-1616PA-50 *CHEC-S SiPM	3	50	SR	TSV	no trenches	CHEC-S buffer
HPK LCT5 S13360-6050CS	6	50	SR	wire-bonds	trenches	MS 13V
HPK LCT5 6.975MM-SIL Single	6.915	75	SR	wire-bonds	trenches	MS 8V
HPK 6050HWB-LVR-LCT	6	50	SR	TSV	trenches	MS 13V
SensL FJ60035	6	35	glass	TSV	no trenches	MS 15V

Figure 23: List of SiPM devices which results are presented in this work. *(SR: silicon resin , MS: MiniCircuits , TSV: through silicon via)

871 SiPM devices for CTA are researched by many different groups, validating different characteris-
 872 tics. Besides the current SiPM for CHEC-S, newly developed prototypes offer a diverse range of
 873 pixel- and cellsizes. The majority of the devices are tested in Japan, at the University of Nagoya,
 874 conducting in depth analysis of the characteristics over a wide over-voltage range at one static
 875 temperature, mainly focusing on PDE and OCT, and their correlation. This correlation of OCT
 876 and PDE for all devices determines the candidate for CHEC-S, by comparing the highest PDE
 877 at the lowest possible OCT for each device. At MPIK, chosen candidate devices are examined
 878 regarding different characteristics and their temperature dependence and as to assist in the final
 879 decision by confirming results with a different analysis technique.

880

881 The chosen devices include the current CHEC-S device HPK S12642-1616PA-50, from Hamam-
 882 matsu Photonics K.K., to be implemented in the first prototype camera. It is a previous gen-
 883 eration SiPM, which was decided for use in 2014, due to the limited availability in high PDE
 884 devices at that time. The manufacturer supplies a 16*16 channel premounted tile of $3 \times 3 \text{ mm}^2$
 885 pixels with a cell-size of $50 \mu\text{m}$. To emulate the usage in a TARGET module, four $3 \times 3 \text{ mm}^2$
 886 pixels are electrically connected to form a $6 \times 6 \text{ mm}^2$ superpixel. The tile is typically coated with
 887 epoxy resin, but due to specific requirements regarding the uniformity of the coating, it was re-
 888 placed with a very thin layer of silicon resin equivalent to later prototypes. The CHEC-S devices
 889 electronical connection is realized via the new through-silicon-via (TSV) concept of running a

890 connecting solder through the silicon bulk, instead of wiring on the outside, greatly increasing
891 the fill-factor, but also including some disadvantageous sideeffects later shown.

892

893 Additional tested devices include the LCT5 generation from Hamamatsu Photonics K.K., so
894 called due to their low cross talk properties, namely the commercial available S13360-5050CS.
895 This device is the first to include physical trenches between the cells, effectively dividing the
896 cells optically and thus reducing prompt cross-talk probability.

897

898 The LCT5 generation also made two prototype devices available for testing at MPIK, the first,
899 HPK LCT5 6.975MM-SIL Single, is a larger iteration with a cellsize of 75 μm and a pixelsize of
900 6.915 mm, leading to larger fill-factor, which would imply higher PDE, but also DCR and OCT.
901 Being from the LCT5 generation it also includes optical trenches. The second device available
902 is a LCT5 prototype designated 6050HWB-LVR-LCT , LVR meaning low-voltage-range, with the
903 same physical dimensions and properties as the S13360 device but incorporating TSV technology
904 and possibly other unknown deviations.

905

906 The final device is a commercially available test-array designated FJ60035 from SensL, pre-
907 mounted on a test-array by the manufacturer. It has the same pixel-size, but a much smaller
908 cell-size 35 μm than the previous mentioned devices, and such a lower fill-factor, and a different
909 coating (glass).

910

911 The tests conducted in Nagoya contain many different iterations of the LCT5 generation with
912 varying pixel- and cell-sizes[19]. For a full overview of the considered SiPMs, please refer to
913 section(H).

914 6.2 Hamamatsu S12642-1616PA-50 50 μ m 3mm

916 The SiPM by Hamamatsu Photonics designated S12642-1616PA-
917 50 is a 3 mm by 3 mm device. The array uses the TSV tech-
918 nology, meaning there are no wire-bonds present, the electrical
919 connection is realized through the silicon-body. The pixels are
920 coated with a thin film of silicon resin, after the previously used
921 epoxy resin proved not uniform enough. The electrical contact
922 is realized through the TSV technology, establishing connection
923 through the silicon bulk, allowing a tighter fit of the cells, with
924 minimal dead-space. One array consists of 256 pixels, four of
925 which are electrically tied together to form a 6 mm by 6 mm superpixel respectively, due to
926 limited availability at the time of 6x6 mm² pixels. Simulations showed 6x6 mm² pixels to be the
927 best choice, balancing FoV and angular resolution.

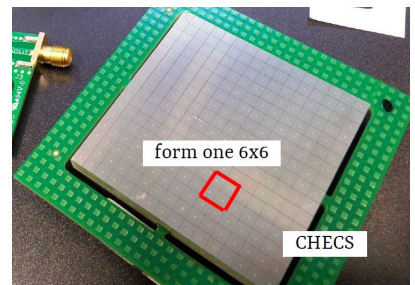


Figure 24: CHEC-S tile

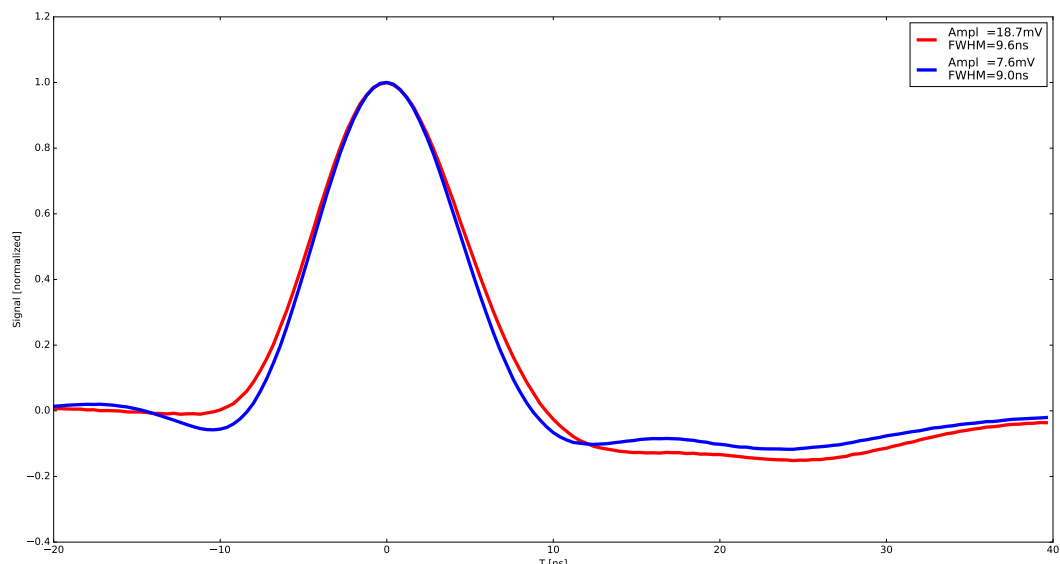


Figure 25: The average pulse shape of the 1photoelectron in blue and the 2photoelectron pulse in red of HPK S12642 at 25° C and 67.8V, which is around the proposed operating point. Both pulses are averaged over »1000 events and normalized to illustrate possible differences in pulseshape resulting from the utilized shaping electronics. Both pulses have a FWHM of around 10ns and are nearly free of ringing. The resulting average amplitude of the 1p.e. pulse is later used to calculate the Gain in [mV/p.e.] instead of [V*IntWin] by cross-referencing the 1 p.e. amplitude at multiple bias-voltages.

928 The measurements of the CHEC-S tile concentrate on the array as an as-is device. This means
929 their performance, influenced by external factors outside the actual SiPMs physics, are valid on
930 the assumption, that the way the measurements were conducted is the way the photomultiplier

will later be incorporated into the camera. On that ground, deviations of results of this works from the results of other groups and the manufacturer itself are expected. To clarify this further, for example, it is expected that the tests done at Hamamatsu Photonics where conducted on a single 3 mm pixel, not an array of 256 pixels, where four are tied together. Also divergence of shaping and amplification electronics between the groups will result in some differences. For this test, the CHEC-S tile is connected to the CHEC-S buffer, supplied with ± 4 V, where the signal is amplified. This signal in turn is then shaped via the CHEC-S shaper, developed by the University of Leicester, see section(4). This whole amplification and shaping chain is simulating later usage in the TARGET modules. Multiple measurements were conducted on many different pixels of the CHEC-S tile, see section(I). The deviation between the pixels showed larger than measurement errors.

6.2.1 Gain

As described in section(3.2), the average pulse shape fig(25) is used to convert the relative gain from the analysis procedure to an absolute gain in sensible units. This is necessary, because the analysis aims to use pulse-area rather than -height, which results in this relative gain being in units of $V \times \text{timebins}$, instead of voltage. Figure(26) shows the gain after conversion. A lower gain with increasing temperature is expected and described in detail in section(3.2). In short, increased lattice movement due to higher temperature hinders photoelectron transport. The effects visible at extreme bias-voltages at both ends are partially analysis related. The gain of a SiPM is expected to be linear over bias-voltage at a constant temperature.

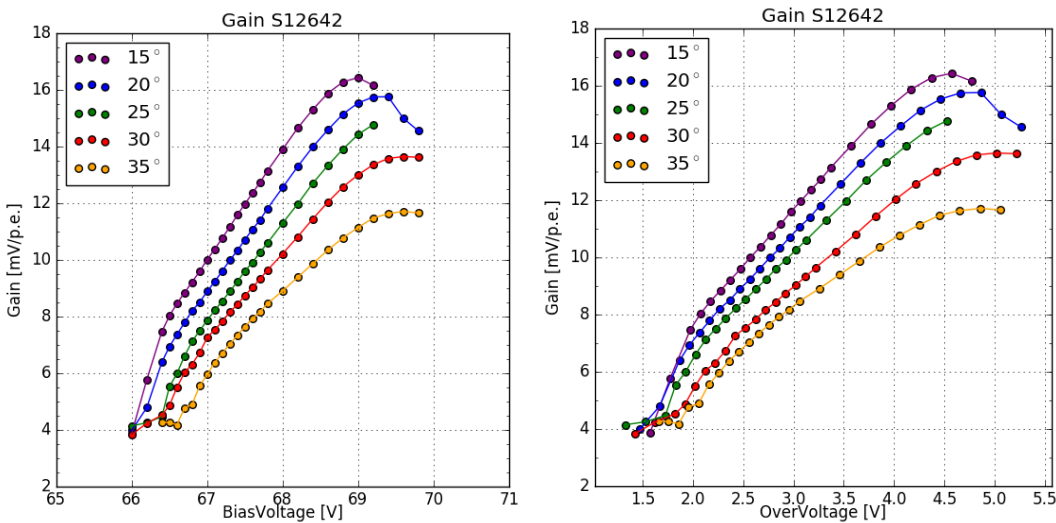


Figure 26: Gain of the HPK S12642 pixel, plotted against over-voltage , bias-voltage and temperature.

In the lower regime at bias-voltages ~ 66.5 V the gain is low compared to the noise, so the analysis struggles to pick up pulses. Depending on the determined peak-finding threshold, the analysis is suspected to interpret noise peaks as 1p.e. peaks at an increasing rate, the lower the

955 overvoltage is. This is visible in the sudden break in linearity at 30 °C and 35 °C , where the gain
 956 is almost in a plateau, due to this effect. The roll-over of the gain at the highest bias-voltages is
 957 in part a result of a voltage drop across the bias resistor occurring, because of high current flow
 958 through the SiPM. At higher temperatures, and therefore higher dark rates, the effect occurs at
 959 lower over-voltages. A second influence is caused again, by the noise at over-voltages of ~5 V,
 960 which is very high compared to the proposed point of operation at over-voltages of ~3 V. The
 961 same threshold is again counting the now increased noise peaks as 1p.e. peaks, but due to the
 962 abundance of 1p.e. pulses this results in an apparent lowering of the gain.

963 6.2.2 Dark Count Rate

965 The DCR is expected to increase with temperature, which is the case for S12642 shown in
 966 Figure(27) and to follow a nearly linear progression, a sudden turn-up or turn-down of the DCR
 967 would be analysis related. The turn-up at a certain point is visible in fig(27), particularly for
 968 15° C (purple) and 20° C (blue) respectively. At 15° C and an over-voltage of ~4V, the DCR
 969 starts to deviate from the previously linear behaviour. It starts to rise more rapid than before,
 970 the OCT at that point is also very high; exceeding 50% fig(28) (left). For the higher tempera-
 971 tures of 25° C (green) and 30° C (red) this critical point is not reached, so the effect is barely,
 if not at all visible. At 35° C (yellow), due to the high rate of 9-10 MHz, slight heating of

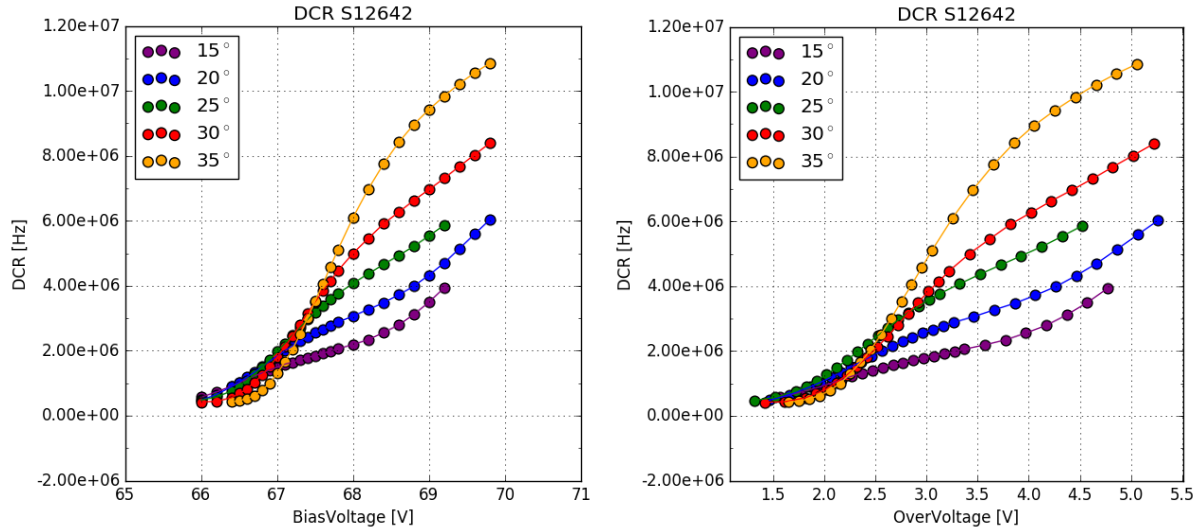


Figure 27: Dark Count Rate of the HPK S12642 pixel, plotted against over-voltage , bias-voltage and temperature. DCR at 2 - 3 MHz from datasheet at operation voltage = 2.4V and 25°C measured by current.

972
 973 the SiPMs surface could also affect the DCR through a slight shift of the temperature upwards,
 974 away from 35° C . So that the DCR declared at 35° C is in reality the rate at higher temperatures.

975
 976 At the lowest end of the bias-voltage range, part of the found 1p.e. pulses are suspected

977 to be noise related. So the DCR changing to a plateau is expected. This is also due to the
 978 fact, that the measurements are done with a fixed bias-voltage range. Due to the increase of
 979 the breakdown-voltage with rising temperature, part of the measured bias-voltage range cor-
 980 responding to a very low over-voltage, attributes to this effect. In order to reliably measure
 981 beyond an overvoltage of 2.5V in the lower range, the noise would need to be improved.

982 6.2.3 Optical Cross Talk

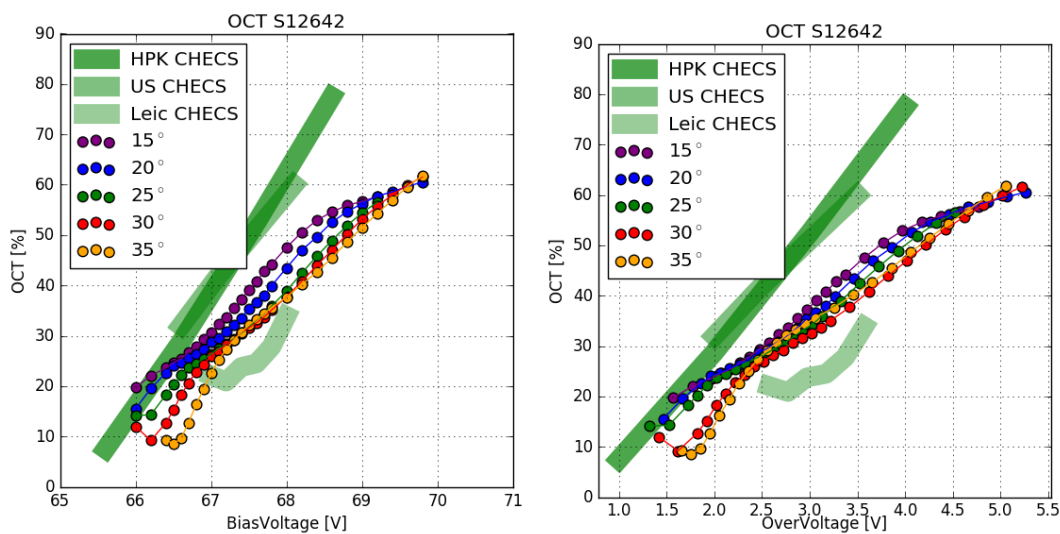


Figure 28: Optical Cross Talk of the HPK S12642 pixel, plotted against over-voltage , bias-voltage and temperature.

984 The OCT is expected to be linear and independent from temperature. This is confirmed for
 985 HPK S12642. Minor deviations from that are probably due to slight errors in the breakdown-
 986 voltage calculation from the gain regression line. At higher DCR the multi incident probability
 987 rises, an event of two simultaneous dark counts could easily be interpreted as a dark event
 988 + cross-talk. This leads to a systematic increase in OCT at the higher DCR, for examples see
 989 section(K).

990 The deviation of 30° C and 35° C below an over-voltage of 2V stems from the way the gain
 991 regression line is used to calculate both DCR and OCT. At higher temperatures the lower voltage
 992 range consists partly of noise, so using the gain regression line to calculate the OCT at those low
 993 voltages leads to the visible effect of the first few datapoints of 30° C and 35° C.

994 The deviations between the different groups results at 25° C (green) are caused by 4 major
 995 factors. Firstly the difference in the tested device. While the device measurements in this
 996 work has every four 3x3mm² pixels electrically tied together, the way the device will later be
 997 implemented into CHEC-S, the groups in the US[17] and Hamamatsu Photonics[16] are likely
 998 to run tests on one 3x3mm² pixel only. Secondly a slight difference in amplification and shaping
 999 electronics is suspected. The measurements conducted in this work as well as the measurements
 1000 of Leicester are done with the same shaper and buffer configuration. The difference here is,

1001 thirdly, measurements are done with dark counts only, while measurements from other groups
1002 are conducted with a pulsed light source and reading out timed windows. This causes the results
1003 from Leicester to be difficult to compare against, their surface temperature of the SiPM is likely
1004 much higher than 25° C, and thus, a misinterpreted breakdown-voltage at 25° C causes a shift
1005 of the OCT to the right. Lastly the difference in actual data taking and analysis procedure must
1006 be mentioned, also this is only of minor concern, as we will see with other measured devices.

1007
1008

6.3 Hamamatsu LCT5 50 μ m 6mm

1009 The SiPM designated HPK S13360 6050CS fig(29) is
1010 an LCT5, meaning Low Cross Talk 5th iteration de-
1011 vice from Hamamatsu Photonics. It is one of the most
1012 promising candidates for later usage in CHEC-S. It has
1013 a pixelsize of 6 mm consisting of 14400 cells with a
1014 cellsize of 50 μ m. The present device and its similar
1015 iterations are the first to incorporate trenches border-
1016 ing each cell, effectively insulating the cells and reduc-
1017 ing the prompt OCT. Tests are done with a single pixel
1018 only, in contrast to measurements done on S12642. It
1019 is mounted on a ceramic chip and coated with a sil-
1020 icon resin that is UV-transparent. Wire-bonds supply
1021 the electrical contact. A similar, but not tested, device from the same generation uses TSV
1022 technology.

LCT5 6mm

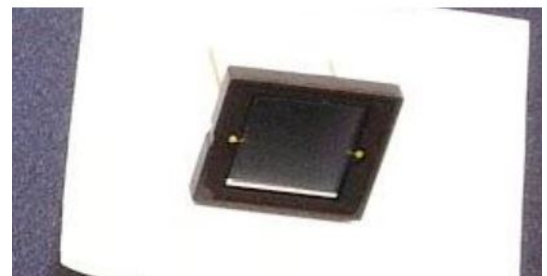


Figure 29: HPK S13360 6050CS pixel

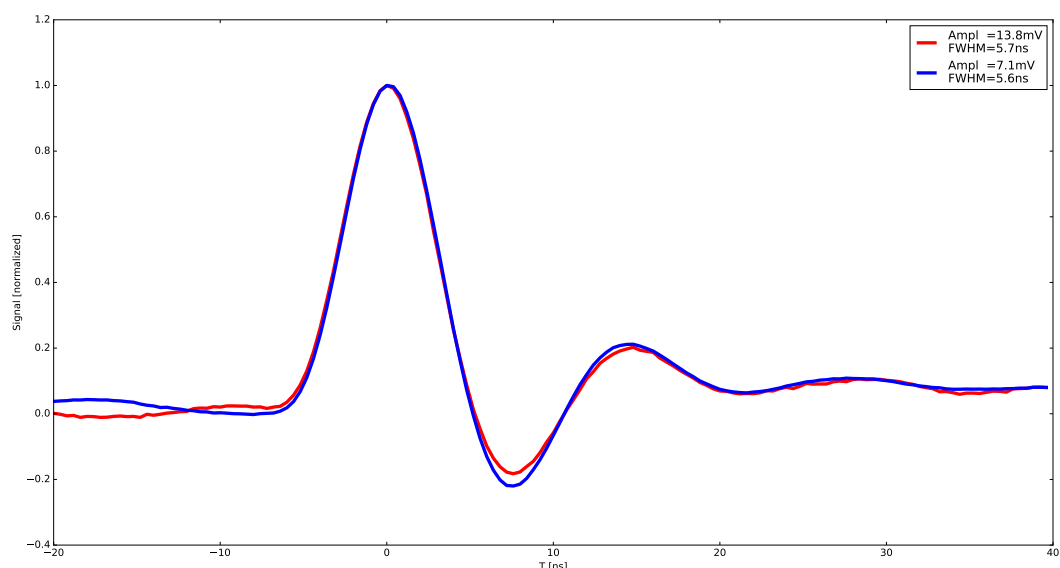


Figure 30: The average pulse shape of the 1photoelectron in blue and the 2photoelectron pulse in red of HPK S13360 6050CS at 25° C and at point of operation. Both pulses have a FWHM of around 5ns and ring for approximately 20ns with an undershoot of 20%.

1023 The layout of the single pixel test device made external amplification necessary. An amplifier
1024 from MiniCircuits was supplied with 13V during this test. Shaping of the pulse is conducted
1025 by a CHEC-S shaper, modified to fit the new unshaped pulse. The pulse shape fig(30) makes
1026 the pulses appear much harder to analyze, due to the possibility of events occurring during the
1027 ringing window. This assumption proved untrue, due to the devices low DCR and OCT, resulting
1028 in a low multi incident probability.

1029 6.3.1 Gain

1031 The gain of the LCT5 50 μ m 6mm device is clearly linear with some minor outliers at 30°C.
1032 The same effect as with S12642 is visible at 35°C, again counting noise peaks as 1p.e. peaks,
1033 resulting in an apparent lowering of the gain and the slope changing over into a plateau. In
1034 figure(31)(left) the gain is shown, plotted against over-voltage. It is still dependent on tem-
1035 perature, but due to reliable breakdown-voltage calculation, the spread is much smaller than,
1036 if plotted against bias-voltage. The same conversion is done to transform relative gain into an
1037 absolute gain with sensible units. When parametrized with over-voltage, the gain is essentially
temperature independent.

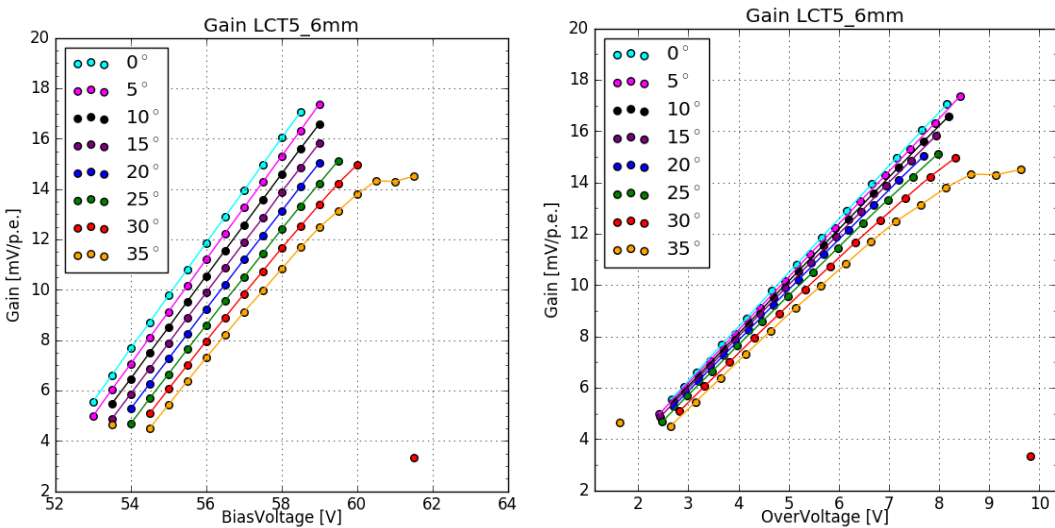


Figure 31: Gain of the HPK S13360 pixel, plotted against over-voltage , bias-voltage and temper-
ature.

1039 6.3.2 Dark Count Rate

1041 The DCR of two similar HPK S13360 devices is shown in figure(32). The bars show the dif-
1042 ference between the two devices, the results of one device is used as a reference, while the
1043 deviation is illustrated with the filled bar. The DCR of HPK S13360 follows the expected be-
1044 haviour, mostly linear in the significant range and rising with increasing temperature. Below
1045 an over-voltage of 2.5 V the gain is suspected to be low enough for larger noise peaks to be
1046 misinterpreted as events. Thus the regression line calculation is unreliable in this range.
1047 The turn-up at high over-voltages is most prominent at 0 °C(teal) after an over-voltage of 9 V.
1048 This is also the point where the OCT rises very rapidly. It is not pulse related, being at a DCR of
1049 1 MHz it would be visible earlier for higher temperatures, but their slope is linear.
1050 The datasheet values from the manufacturer cover a large range of the DCR at an over-voltage
1051 of 3V making it difficult to compare against, the manufacturer determines the DCR by measur-
1052 ing the current.

1053

1054 A standard counting error of the DCR is largest in the lower bias-voltage range. Despite the
 1055 low DCR at an over-voltage of 2 V of ≤ 0.5 MHz, in a measurement window of $100 \mu\text{s}$ there
 1056 are still ≥ 50 pulses detected. This means an experimental run of 500 segments of the $100 \mu\text{s}$
 1057 measurement window shows a standard counting error in the DCR of 0.003 MHz, below 0.1%.
 1058 This is lower than errors related to analysis or data acquisition and not visible given the size of
 1059 the datapoints.

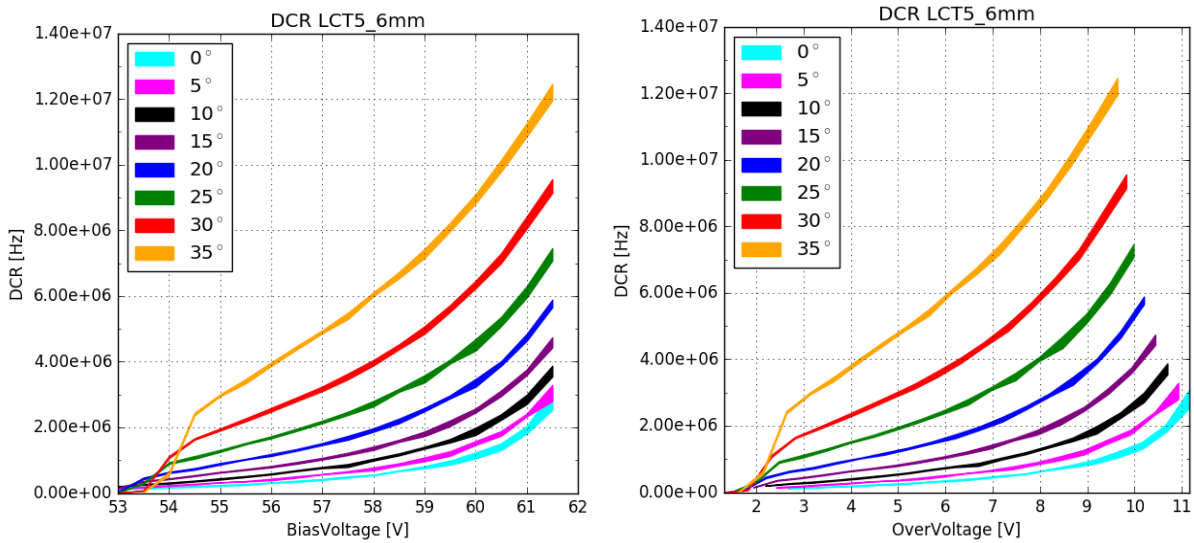


Figure 32: Dark Count Rate of the HPK S13360 pixel, plotted against over-voltage , bias-voltage and temperature. The Datasheet values cover a very large range between a DCR of 2 - 6 MHz at an over-voltage of 3 V at 25 °C, to wide to compare to reliably, and is measured by current.

1060
1061

6.3.3 Optical Cross Talk

1062 The measurements of the HPK S13360 SiPM done at the Nagoya University[19], Japan fig(33)
 1063 (faded green bar), correlate very strong with results from this work of the OCT in the over-
 1064 voltage range between 2.5 V and 9 V. The OCT in this range is linear and independent from
 1065 temperature, with minor deviations attributed to the breakdown-voltage calculation from the
 1066 regression line, causing the horizontal shift. In contrast to the dark counts measurements in this
 1067 thesis, the measurements at Nagoya University followed a pulsed light source approach, read-
 1068 ing out a time-window after the laser incident. This could have consequences, since OCT with
 1069 a longer delay time could be missed. Deviations below an over-voltage of 2.5 V are expected,
 1070 they are very likely caused by the regression line calculation being unreliable in this range due
 1071 to the analysis method misinterpreting noise as dark count events. Above an over-voltage of 9 V,
 1072 which is also the point of the turn-up of the DCR, the OCT is no longer linear and the deviation
 1073 from the results of Nagoya University increase very rapidly. The rapid increase in both DCR

1074 and OCT is suspected to be caused by the over-voltage reaching ranges, where interpretation of
 1075 noise as a 1 p.e. pulse becomes more likely. This, joint together with the usage of the MiniCir-
 1076 cuits amplifier supplied with 13 V, makes false interpretation of noise as pulses even more likely.
 1077 These two reasons in conjunction are suspected to be responsible for both, the sudden rise of
 1078 the DCR as well as the deviation of the OCT from linearity and the results of Nagoya University,
 1079 above over-voltages around 9V. In summary, the correlation between the two measurements,
 1080 conducted by two different methods of data acquisition and analysis, is evident.

1081

1082

1083 The S13360 series is the first to incorporate physical barriers, called trenches, effectively insu-
 1084 lating the cells from each other. This drastically reduces the prompt cross-talk, while increasing
 1085 the percentage the delayed cross-talk contributes to the overall cross-talk shown. This could
 1086 also be the reason for the up-turn, compared to data from the University of Nagoya; at higher
 1087 over-voltages the contribution from delayed cross-talk is higher[14]. With the trenches effec-
 1088 tively reducing the prompt cross-talk and the difference in analysis, the effect could be partially
 1089 explained by increased contribution of the delayed cross-talk. More on this subject in section(7).

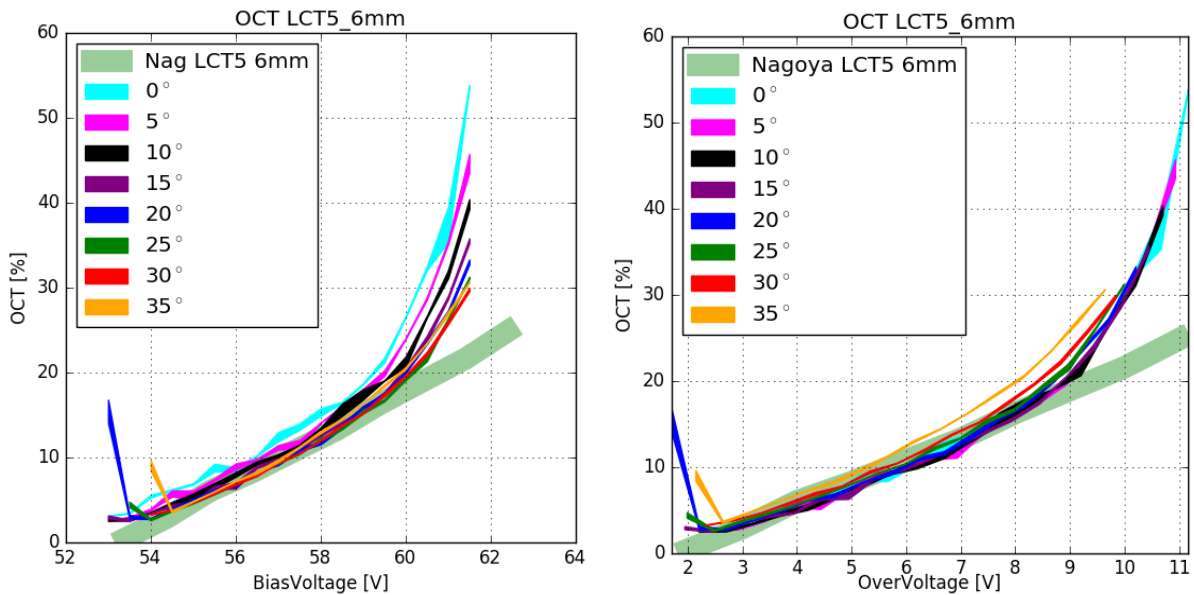


Figure 33: Optical Cross Talk of the HPK S13360 pixel, plotted against over-voltage , bias-voltage and temperature.

1090 6.4 Hamamatsu LCT5 75 μ m 7mm

1092 The device named 6.975MM-SIL Single (fig(34)) is a
1093 larger LCT5 prototype SiPM of the same design as
1094 S13360-6050CS. With an increase in cellsize to 75 μ m,
1095 the device gains a higher fill-factor than 50 μ m devices.
1096 The pixel-area is also expanded to 6.915x6.915 mm²,
1097 which will result in a higher fill-factor (less deadspace),
1098 both size increases together will presumably result in a
1099 higher PDE but also a higher OCT. Since it is a proto-
1100 type device, there is limited data from datasheets. The
1101 ID number suggests, that it is also a wire-bond device
1102 with a UV-transparent silicon-resin coating. It is also a
1103 single pixel test device, so external amplification is nec-
1104 essary with the MiniCircuits PreAMP, supplied with 8V during this test. The signal is shaped by a
1105 differently modified CHEC-S shaper, which results in a pulse shape similar to S12642, but with
1106 a much lower amplitude (fig(35)).

LCT5 7mm



Figure 34: HPK LCT5 7mm pixel

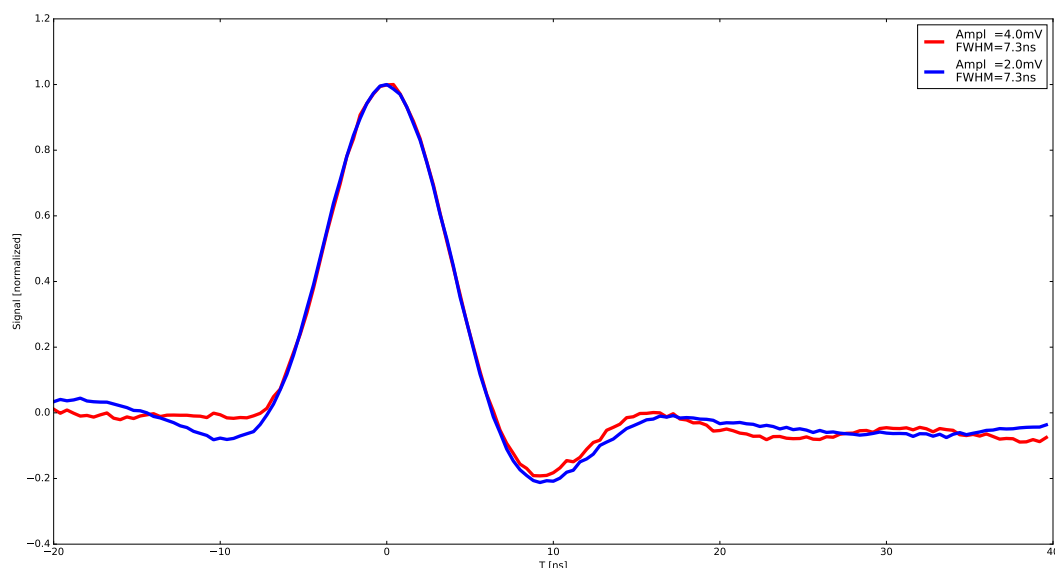


Figure 35: The average pulse shape of the 1 photoelectron in blue and the 2 photoelectron pulse in red of HPK LCT5 7mm at 25° C and at point of operation. Both pulses have a FWHM of around 7ns and an undershoot of 20%, with no ringing.

1107 6.4.1 Gain

1109 Figure(36) shows the gain of the LCT5 7mm device. Two sets of measurements are done for
1110 25 °C to extend the measured range. The first set of measurements covers the lower over-voltage
1111 range, where the low gain makes external amplification necessary, realized with a MiniCircuits

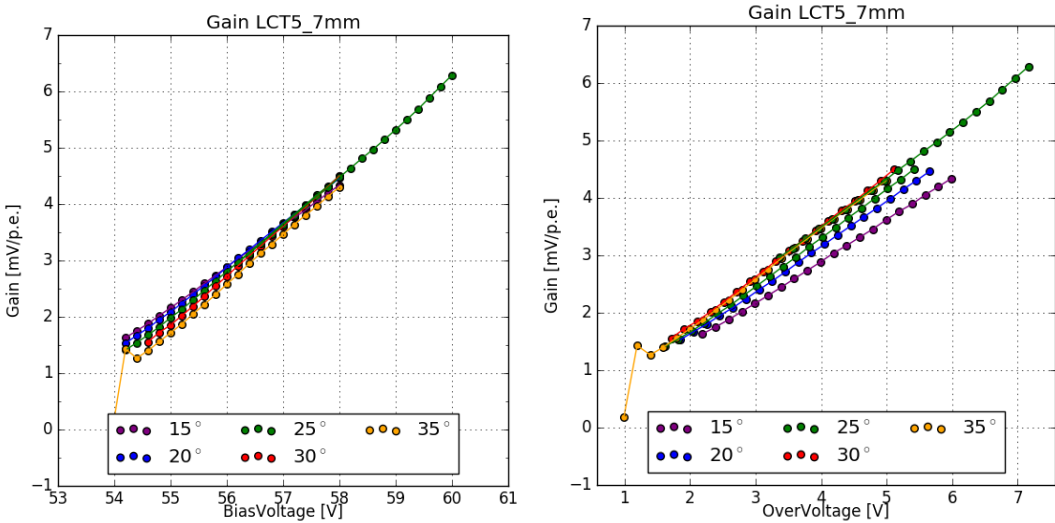


Figure 36: Gain of the HPK LCT5 7mm pixel, plotted against over-voltage , bias-voltage and temperature.

PreAMP supplied with 8 V. The lowest possible amplification of the PreAMP is chosen, so that reaching the point of saturation of the oscilloscope input is as late as possible as the over-voltage rises. Saturation of the oscilloscope occurs due to the possibility of generating very large p.e. (>10 p.e.) events at the higher over-voltages, which are saturating the input. Joint together, the LCT5 7mm device and the MiniCircuits PreAMP at 8 V reach this point at an over-voltage of ~ 6 V. In figure(36) the results from the lower range measurement are displayed as the lower-range green line extending between an over-voltage of 1.6 V to 5.4 V. The configuration for the second test removes the PreAMP from the setup, which makes the lower over-voltage range inaccessible, but extends the range to higher over-voltages. This configuration reaches the point of saturation at an over-voltage of ~ 8 V. The higher range measurement results are displayed as the second green line (25 °C) extending from 3.4 V to 7.2 V over-voltage in figure(36). There is a clearly visible overlap of the two measurements between ~ 3.4 V and ~ 5.4 V . It also seems, that the gain dependency on temperature is reversed. While for all other devices, the gain lowers with rising temperatures, the LCT5 7mm device seems to show inversed behaviour. This inverse behaviour is caused by the calculation of the breakdown-voltage from the gain-regression line and is likely an error. Plotting the gain versus bias-voltage, however, shows the expected behaviour of the gain.

6.4.2 Dark Count Rate

The behaviour of the DCR of the HPK LCT5 7mm device is shown in figure(37) and is as expected. It follows a linear progression in the relevant range and increases with rising temperature. I suspect the over-voltage range above ~ 2.5 V to be relevant. The extended range measurement at 25 °C confirms this behaviour. LCT5 7mm shows a linear DCR over an over-voltage range of 4 V. The faded green bar in figure(37) shows results from measurements undertaken

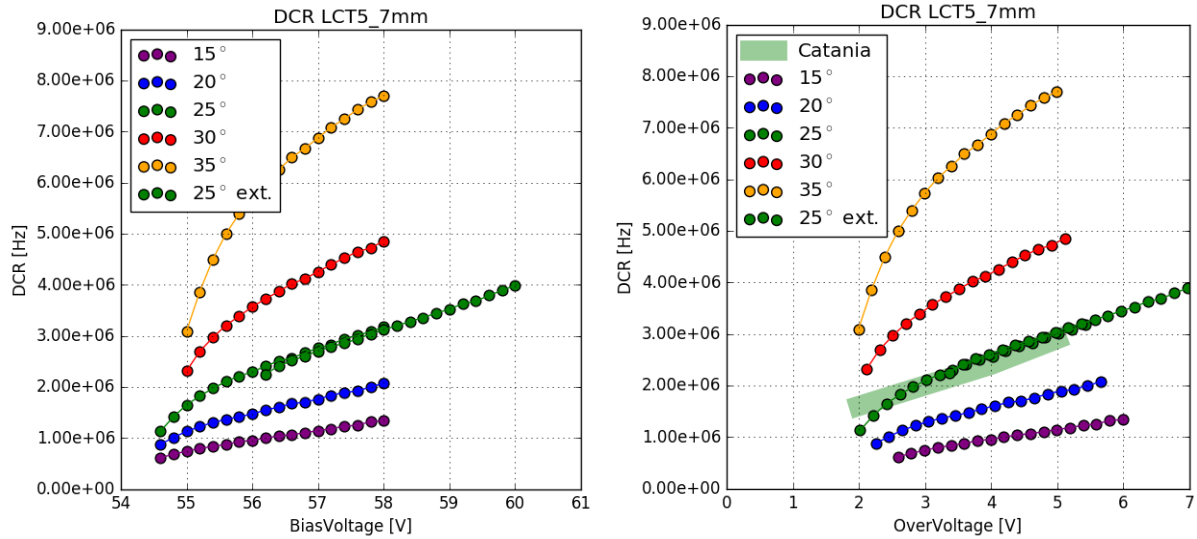


Figure 37: DCR of the HPK LCT5 7mm pixel, plotted against over-voltage , bias-voltage and temperature.

1136 by the Department of Physics and Astronomy at the University of Catania. Those measurements
 1137 were conducted on the exact same device, which is an important point, but with a different
 1138 method of data acquisition and data analysis. Analysis techniques are discussed in section(7).
 1139 The correlation between the two experiments is evident, although there is differences in the
 1140 acquisition and analysis process.

1141 6.4.3 Optical Cross Talk

1142

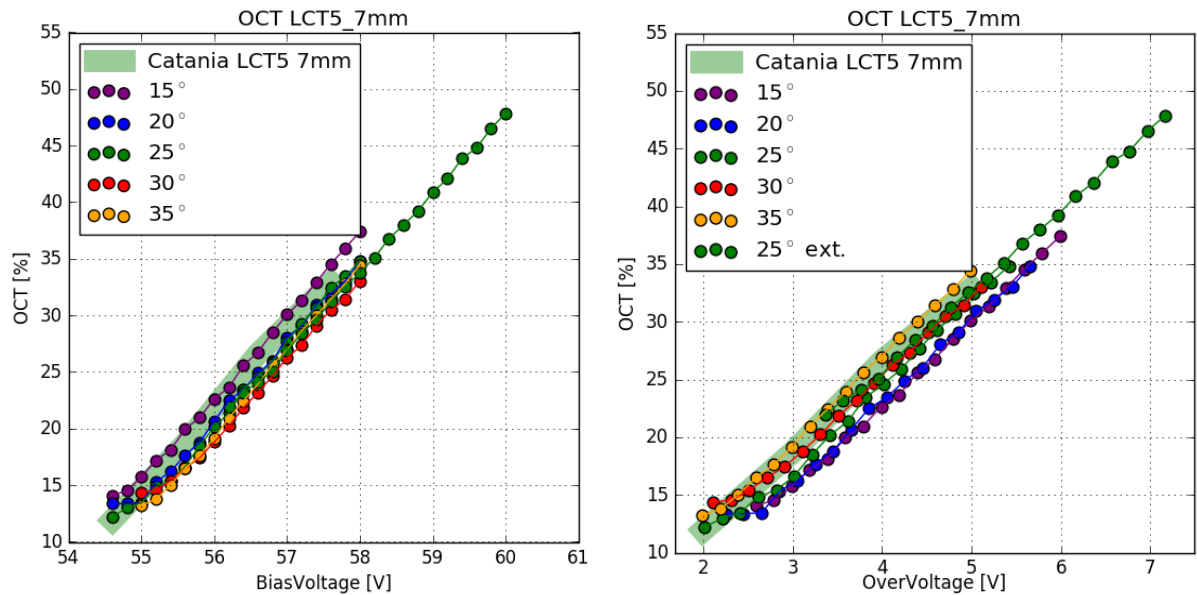


Figure 38: Optical Cross Talk of the HPK LCT5 7mm pixel, plotted against over-voltage , bias-
 voltage and temperature.

1143 The OCT is expected to be linear and independent from temperature. This is the case in
1144 the, in section(6.4.2) established, relevant over-voltage range of above ~2.5 V (fig(38)). Minor
1145 deviations are attributed to the calculation of the breakdown-voltage from the gain-regression
1146 line. The over-voltage is calculated from the former and the supplied bias-voltage, which in turn
1147 causes a slight horizontal shift. With that, comparing the results from this work to the measure-
1148 ments at 25 °C (faded green bar) from the University of Catania shows a strong correlation.

1149 6.5 Hamamatsu LVR 50 μ m 6mm 1150

1151 The SiPM by Hamamatsu Photonics with the designation
1152 6050HWB-LVR-LCT is a special prototype of the
1153 LCT5 design. LVR is an abbreviation of Low Voltage
1154 Range, meaning the device is meant to be operated
1155 at much lower operation voltages than other LCT5 de-
1156 vices. It has the same physical size as an LCT5 device
1157 (S13360 section(6.3)), a pixelsize of 6mm pixel with
1158 a cellsize of 50 μ m. The recommended point of opera-
1159 tion however is \sim 15V below that of the S13360 device,
1160 specifically at 40.2V(LVR) instead of 54.7V (S13360).
1161 It uses the TSV technology for electrical connection.
1162 The unshaped signal is similar to other LCT5 devices, therefore using the same modified CHEC-
1163 S shaper is feasible in this case, resulting in a similar pulse shape fig(40). After that the signal
1164 is amplified with the same MiniCircuits PreAMP supplied with 8.5V.

1165

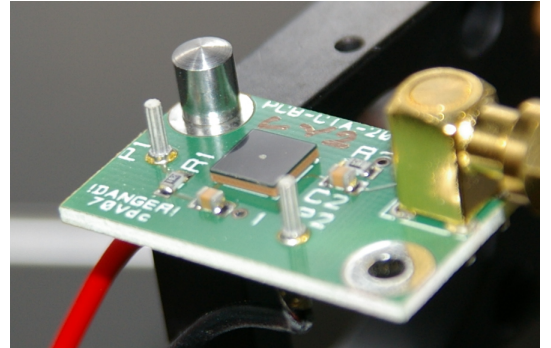


Figure 39: HPK LVR 6mm pixel

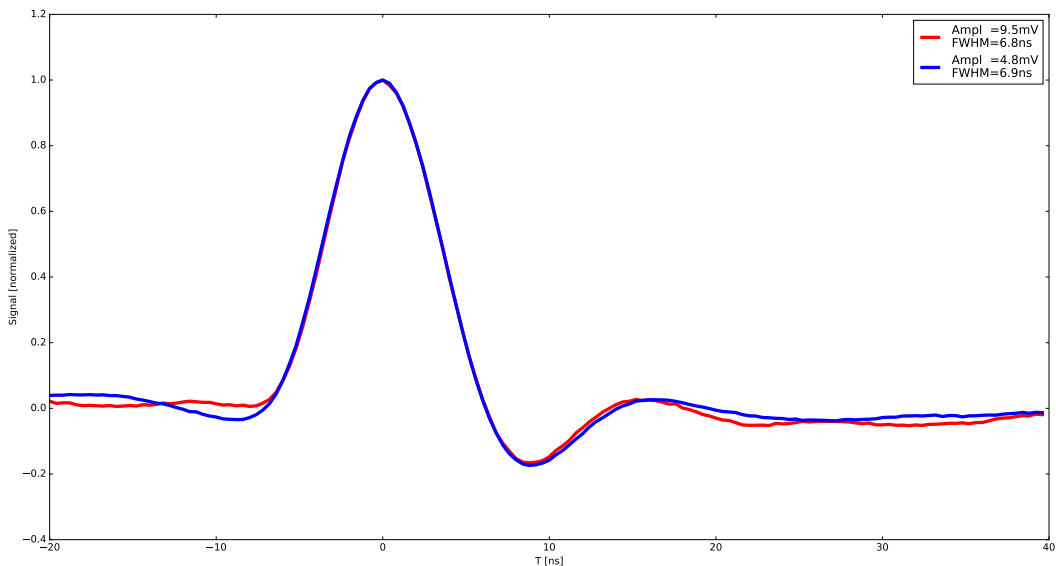


Figure 40: The average pulse shape of the 1photoelectron in blue and the 2photoelectron pulse in red of HPK LVR 6mm at 25° C and at point of operation. Both pulses have a FWHM of around 7ns and an undershoot of 20%, with no ringing.

1166 6.5.1 Gain 1167

1168 Figure(41)(right) shows the gain of the LVR 6mm device. It is, as expected, linear over a
1169 long range and nearly independent of temperature when parametrized with over-voltage. The
1170 flattening of the slope to a plateau shape in the lower over-voltage range is caused by noise

pollution. Only taking into account the linear region, limits the range, where the results are relevant to an over-voltage range above ~ 2.5 V. Saturation of the oscilloscope in this range is not visible, but a check with a more expanded range revealed, that the point of saturation of the oscilloscope is at an over-voltage of ~ 5 V. The apparent overlap of the gain, when plotted against over-voltage, is based on the calculation of the breakdown-voltage being very reliable due to the large linear range. Plotted versus bias-voltage fig(41)(left) the expected behaviour of the gain, lowering with increasing temperature, is visible.

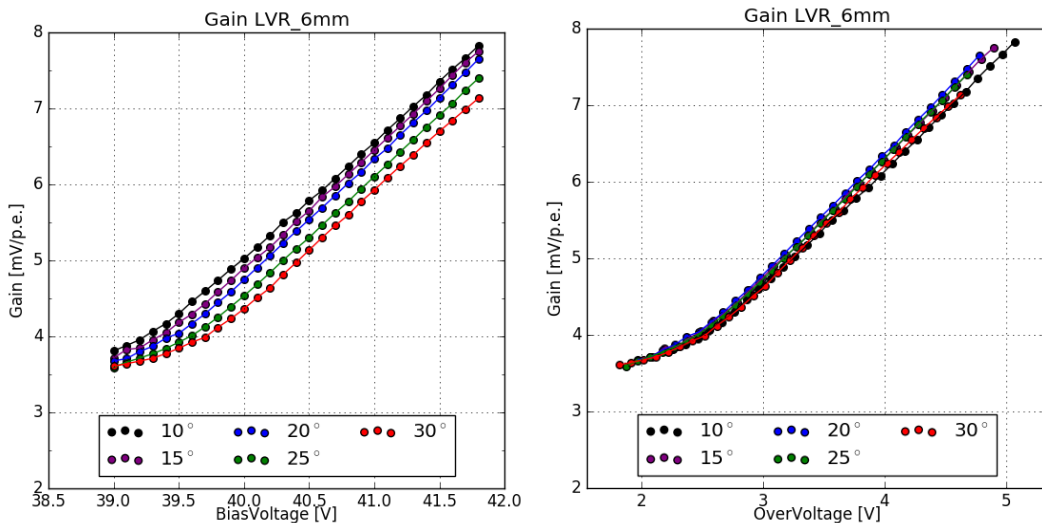


Figure 41: Gain of the HPK LVR 6mm pixel, plotted against over-voltage , bias-voltage and temperature.

1177

1178
1179

6.5.2 Dark Count Rate and Optical Cross Talk

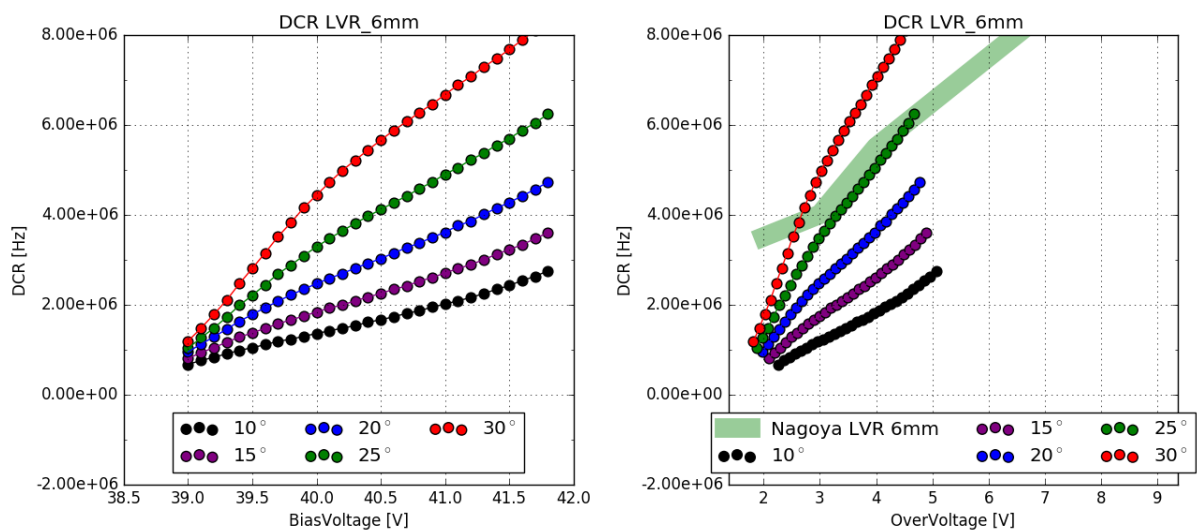


Figure 42: Dark Count Rate of the HPK LVR 6mm pixel, plotted against over-voltage , bias-voltage and temperature.

1180 The DCR fig(??)(left), taking into account only the relevant over-voltage range of $>\sim 2.5V$
 1181 seems to correlate, while the resulting OCT fig(??)(right) is very high compared to results from
 1182 the University of Nagoya, which also cover a much wider range. Only taking into account the
 1183 previously established relevant over-voltage range of $>\sim 2.5V$, the resulting OCT is a factor of
 1184 two higher. The device being a prototype, it could be the case, that there are physical differences,
 1185 a difference in coating, which combined with the TSV technology could lead to the present
 1186 uncorrelation[20]. This uncertainty is a contrast to results from previous devices, where strong
 correlations between different groups and measurement techniques are evident.

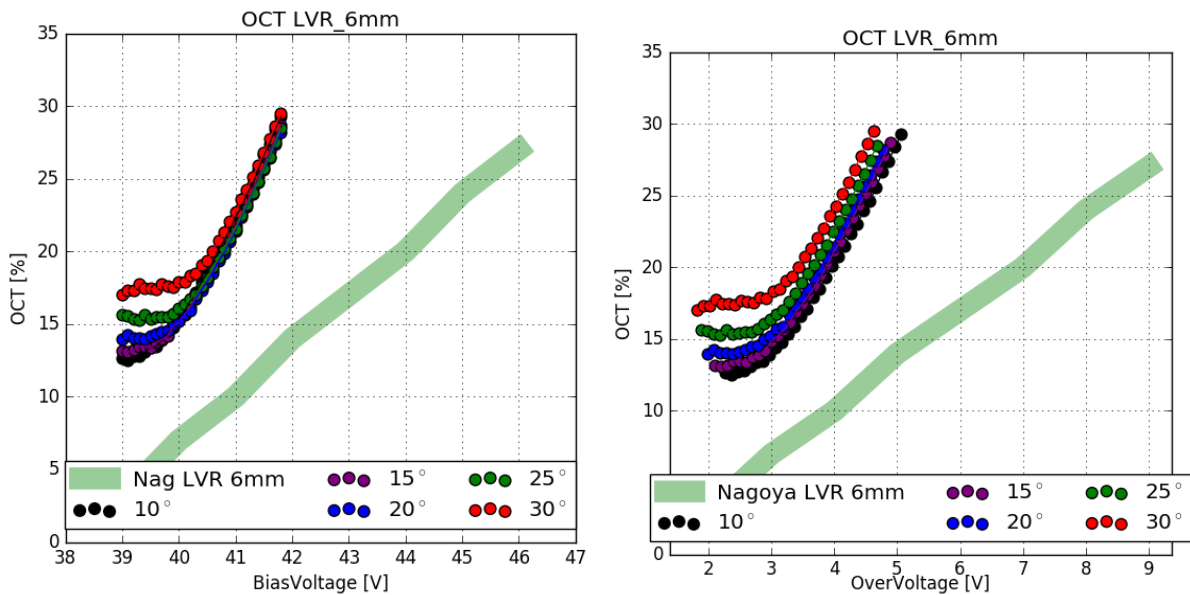


Figure 43: Optical Cross Talk of the HPK LVR 6mm pixel, plotted against over-voltage , bias-voltage and temperature.

1188 6.6 SensL FJ60035 6mm 35 μ m

1190 The SiPM by SensL with the designation FJ-60035 is another candidate device for use to pop-
1191 ulate the focal plane of CHEC-S. It is also a 6mm device, but with a much smaller cellsize of
1192 35 μ m, using the TSV technology, so there are no wire-bonds present. This results in 22292 cells
1193 on a single pixel with a fill-factor of 75% . It is coated with plain glass. The recommended
1194 point of operation is around 30V bias-voltage, lower even than that of the HPK IVR prototypes.
1195 The device is, by the manufacturer, pre-mounted on a printed circuit board, called a test ar-
1196 ray. This test array contains a fast output, that directly couples to the cells, and a slow output,
1197 conventionally read out via the quench resistor. For the conducted tests, I used the fast output
1198 amplified with the MiniCircuits PreAMP supplied with 12V. The SensL device was the first de-
1199 vice measured, therefore the analysis procedure used was an older iteration compared to the
1200 procedure for the Hamamatsu devices.

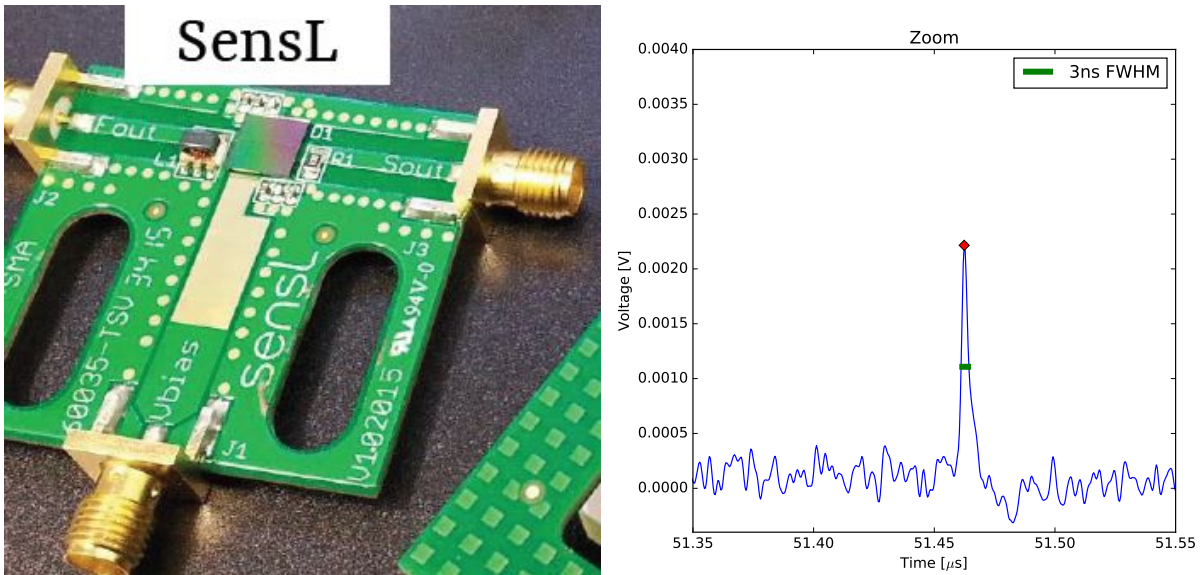


Figure 44: SensL Test Array and the average pulse shape at $V_{bias-voltage} = 29V$

1201 6.6.1 Gain

1203 Evaluating the SensL pulse area spectra shows the 1 p.e. position and Δ p.e. overlapping,
1204 so using the older analysis iteration introduced no error when evaluating the gain of the SensL
1205 device. It is clearly linear over a wide temperature range from -5°C to 35°C over an over-voltage
1206 ranging from 2V up to 8V. When plotted versus over-voltage the spread of the gain is even
1207 tighter signaling slight temperature independency, but still following the expected behaviour of
1208 decreasing with increasing temperature.

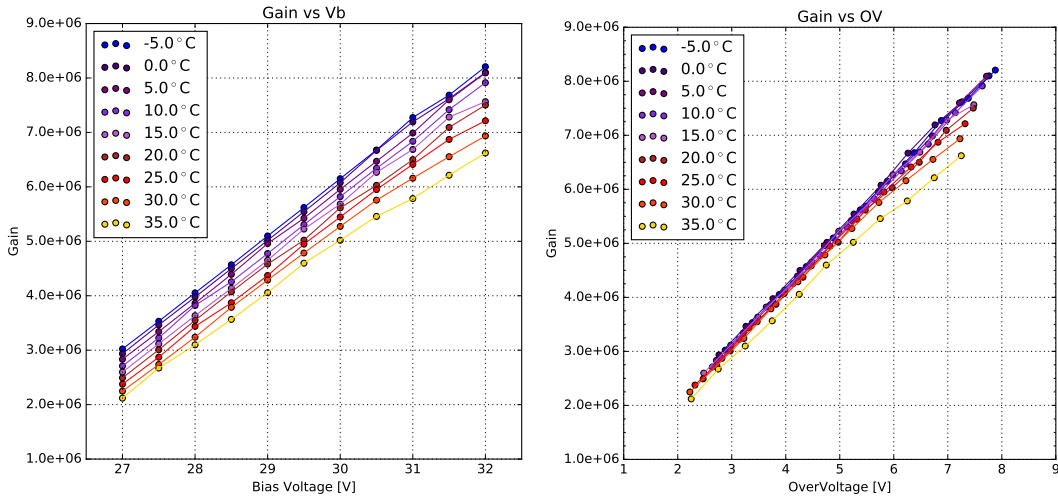


Figure 45: Gain of the SensL FJ-60035 test array, plotted against over-voltage , bias-voltage and temperature.

1209 6.6.2 Dark Count Rate and Optical Cross Talk

1211 The DCR fig(46) also shows the expected behaviour. At very low temperatures the changes in
 1212 rate over the over-voltage range is minimal. Increasing the temperature shows a rapid increase
 1213 in thermally induced dark counts. The OCT fig(47) on the other hand is independent of the
 1214 device temperature, also as expected. In both cases, the values agree with values derived from
 1215 the datasheet.

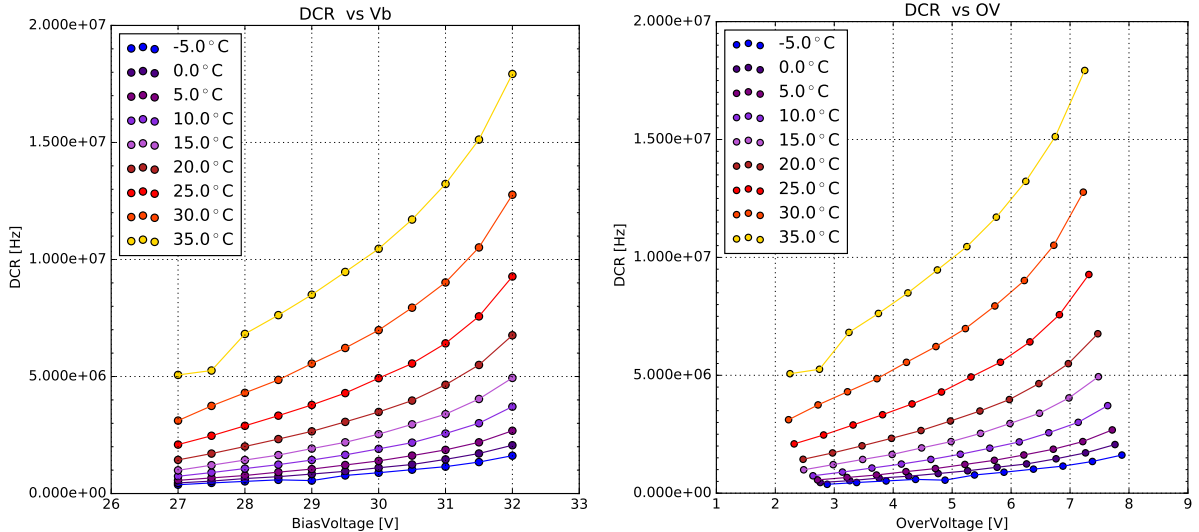


Figure 46: Dark Count Rate of the SensL FJ-60035 test array, plotted against over-voltage , bias-voltage and temperature. Datasheet values at $V_{OV} = 2.5$ V and 5 V at 25 °C are between 1.6 - 2.7 MHz and 2.9 - 5.7 MHz respectively.

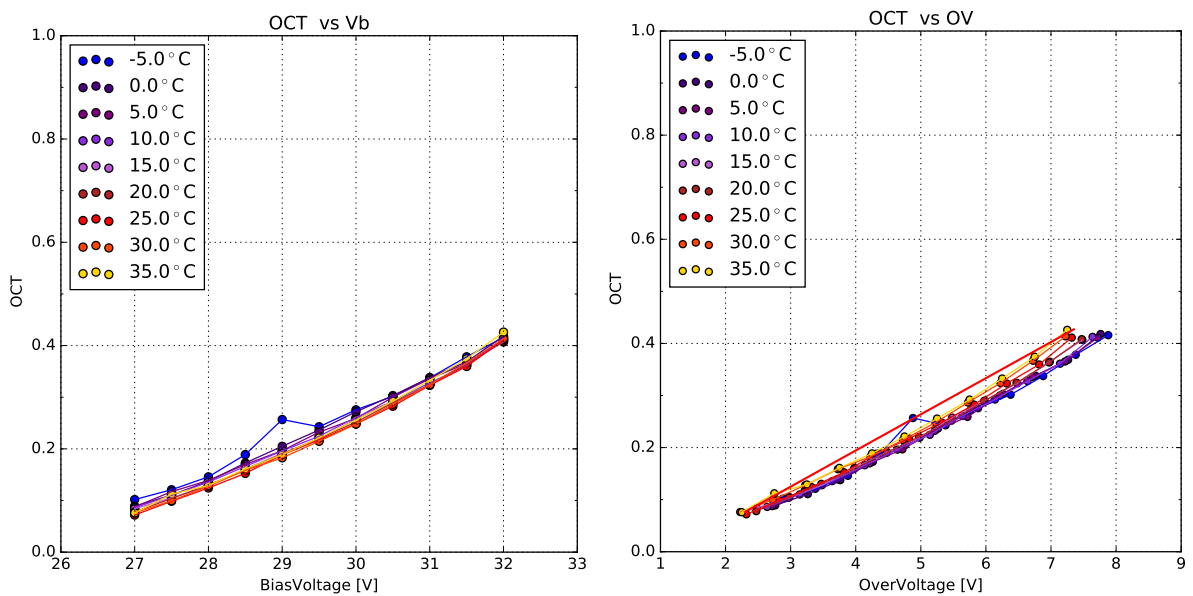


Figure 47: Optical Cross Talk of the SensL FJ-60035 test array, plotted against over-voltage , bias-voltage and temperature. OCT results of Nagoya University marked by the red line. Datasheet values at $V_{OV} = 2.5$ V and 5 V at 25 °C are 7% and 22% respectively.

1216 1217 7 Comparison

1218 A comparison of the performance of all devices is the significant step for choosing the SiPM
1219 later to be used in CHEC-S. In order to do this, all measured characteristics are compared versus
1220 over-voltage. Operation of the CHEC-S camera in GCT will come down to a decision between
1221 two operational points. The first point will be marked by an OCT of under 15%. Every other
1222 attribute of the SiPM at this over-voltage is then compared. This point will trade off precision
1223 for efficiency, a lower OCT makes real event detection easier, on the other hand, a lower PDE
1224 may forfeit a lot of potential data.

1225 The second point of operation is marked at the highest achievable PDE. This work does not
1226 involve PDE measurements, other groups are commissioned to determine the point of highest
1227 PDE. This point will assure the highest detection of event photons, but will trade that for an
1228 increase in detector noise, due to the higher DCR and more importantly OCT.

1229

1230 Comparing results to other groups is shown in figure(48), using different experimental se-
1231 tups and procedures and therefore also entirely different analysis techniques. The groups,
1232 that evaluate SiPMs, the University of Leicester, the University of Nagoya and the University
1233 of Catania, are all conducting fixed window readout of the SiPM after an expected light-pulse
1234 from a flasher-LED or pulsed laser.

1235

1236

1237 1238 7.1 Dark Count Rate

1239 Comparing the DCR of the measured devices and results from the other groups is shown in
1240 figure(48). The differences in analysis procedure will only have a slight impact on the pre-
1241 sumed DCR, since all experiments record dark-count events over their respective acquisition
1242 time windows. On the other hand, if the readout window is sufficiently small, events origi-
1243 nating from afterpulsing or delayed crosstalk could be missed. All groups experience the same
1244 multi-hit coincidence, meaning a light-event or dark-event coinciding with another, forming a
1245 (partial)multi p.e. event.

1246 Only two of the five measured devices have measurements result from other groups to compare,
1247 as it is not their focus. In the case of both, the LVR 6mm and the LCT5 7mm results can be
1248 discussed to some degree as matching. While the correlation is obvious for the LCT5 7mm de-
1249 vice figure(48)(red), where the covered measurement range in this work exceeds the external
1250 results, while matching and showing the same trend, the LVR 6mm results deviate. Between an
1251 over-voltage of 3V and 4V the results overlap, the trend on the other hand is obviously different.
1252 Additionally the limit on the higher range due to noise makes it impossible to compare against

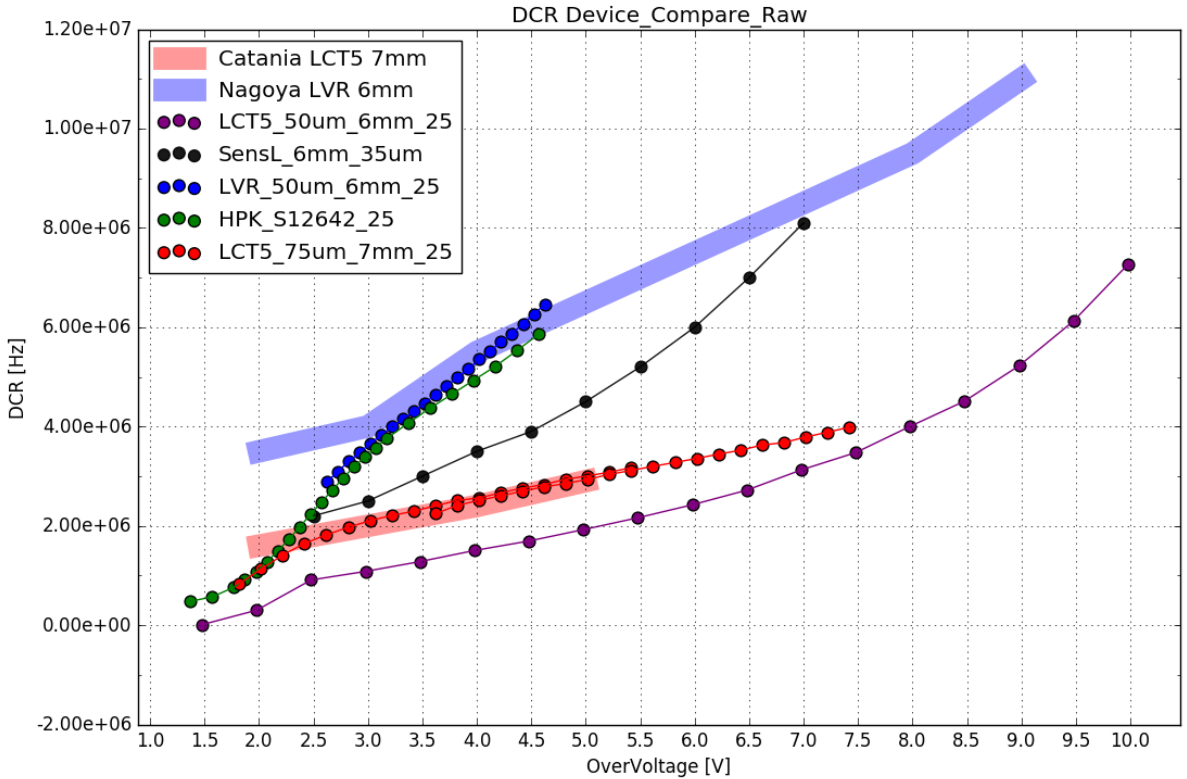


Figure 48: Dark Count Rate comparison of measured devices at 25°C. Description

1253 the full range measured by the external group, so the DCR for LVR 6mm must be labeled as not
 1254 matching.

1255 7.2 Optical Cross Talk

1256 The comparison of the OCT between the different groups and the results presented in this work
 1257 are dependent of the analysis and acquisition procedure. Extended trace analysis, utilized in
 1258 this work captures all aspects of the OCT, prompt and delayed as well as afterpulsing. The
 1259 procedure of time window analysis, utilized by the groups being compared to, are, due to their
 1260 limited window, either biased towards the prompt cross talk or in extreme cases, will not be
 1261 able to capture delayed cross talk or time-delayed afterpulsing at all. Comparing data analysis
 1262 techniques, for example, at the University of Leicester is therefore a vital step. Their approach
 1263 utilizes a pulsed laser as light source and involves no cooling of the SiPM tile. The waveforms
 1264 are extracted from the scope and a small time window is defined from the known time position
 1265 window of the incident pulse to search for peaks, find their value and generate a histogram. To
 1266 the pulse area histogram, a theoretical model of contributing factors is fitted. This theoretical
 1267 model simulates characteristics, updating continuously to find their correct values. Those values
 1268 are the full set of characteristics of the device in testing, among them: gain curve, breakdown-
 1269 voltage, OCT, PDE, noise, dynamic range, crosstalk probability.
 1270 There are a number of differences in their approach compared to the one utilized in this work,

1272 most important is the time window size. If the window after an incident pulse is too short, data
 1273 loss is a possibility, depending on the delay time of delayed cross-talk and afterpulsing assisted
 1274 by traps with long lifetimes. This is a problem, especially with devices of the LCT5 generation
 1275 implementing physical trenches isolating the cells and effectively reducing the prompt cross-
 1276 talk, here the contribution from the prompt cross-talk to the overall OCT is lowered. Missing
 1277 data from delayed cross-talk and afterpulsing, because it will not be recorded yet, would lead
 1278 to errors in the overall OCT results being lower than expected.
 1279

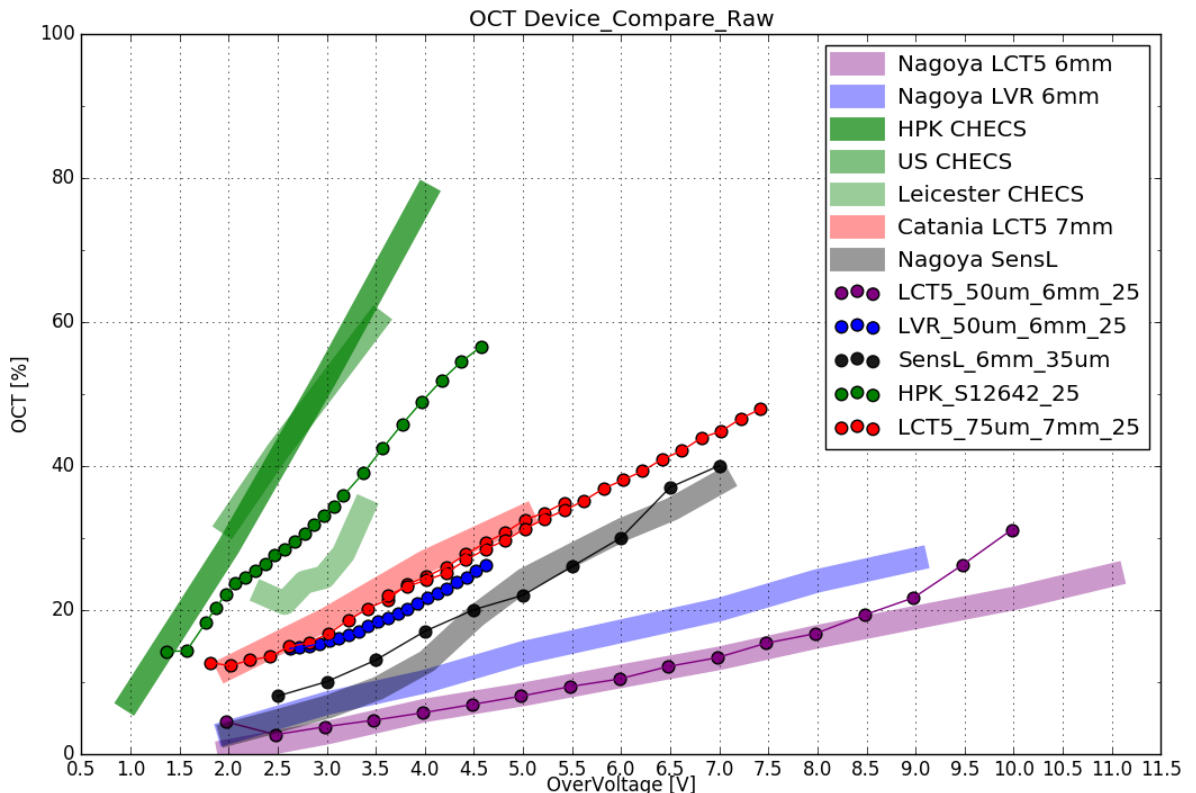


Figure 49: Cross Talk comparison of measured devices at 25°C. Description

1280 This is indeed the case for the S12642 tile in figure(49)(green). The light green bar below
 1281 (negative y-axis) the dotted data presented in this work shows the results from the University
 1282 of Leicester indeed being lower. In purple results of the LCT5 S13360 device with physical
 1283 trenches are shown. Compared to results from the University of Nagoya, there is a prominent
 1284 upturn at around an over-voltage of $\sim 8V$. This could be due to the differences in analysis tech-
 1285 nique. The University of Nagoya also employs time window analysis. LCT5 possesses lowered
 1286 prompt cross-talk probability, so the contribution of delayed cross-talk to the overall cross-talk
 1287 is higher than for S12642. With rising over-voltage the ratio between prompt and delayed
 1288 cross talk shifts towards a higher contribution from delayed cross-talk[14][20]. While at lower
 1289 over-voltages ($\sim 0.5V$) the cross-talk is nearly entirely dominated by the prompt cross-talk with
 1290 nearly no contribution of delayed cross-talk, at ($\sim 2V$) contributions are mostly equal and at

1291 high over-voltages ($\sim 7V$) the contribution of delayed cross-talk is expected to be above 80%,
1292 probably due to higher penetration depth and avalanche probability.
1293 Results of the LCT5 7mm device from both groups mostly overlap, the slight shift between them
1294 is most likely caused by a small error in the breakdown-voltage calculation, due to no cooling
1295 of the tile in experiments involving light. In addition, the slope of both results seems to be mostly
1296 equal, and the extended range measurement, overlapping with the low-range results confirms
1297 that.
1298 Even though results from 3 different groups mostly correlate, or have at least partially un-
1299 derstood differences, the OCT of LVR 6mm figure(49)(blue) compared to the results from the
1300 University of Nagoya do not show any correlation at all. This is concerning, because comparing
1301 S13360 (purple) to the same group showed strong correlation over a wide over-voltage range.
1302 Since there is also no datasheet present yet, this device is a prototype, the assumption is that
1303 the device examined is physically different than the device present at Nagoya. It may just be
1304 a difference in coating, which combined with the TSV technology could lead to the present
1305 uncorrelation[20].

1306 7.3 Point of Operation Comparison 1307

1308 A different method of comparison involves the two proposed points of operation, illustrated
1309 at the beginning of section(7). By adding the PDE measured by external groups, all three
1310 characteristics can be illustrated together. Figure(??) shows the comparison result of the SiPMs
1311 examined in this work. A minimal OCT point of 15% in the left column, and the maximum PDE
1312 points in the right column, both include external PDE measurements.

1313 At the first, minimal OCT, operation point the LCT5 6mm (S13360) device is favorable, since it
1314 possesses a high PDE of 49% with a fairly low DCR below the expected NSB. The currently used
1315 SiPM in CHEC-S only reaches 25% according to datasheet values.

1316 The four HPK devices (the first four in the list), all have a maximum achievable PDE around the
1317 same level, $\sim 50\%$. The difference in DCR and OCT at this level is the deciding factor. While
1318 the current CHEC-S SiPM reaches a very high OCT level of $\sim 50\%$, the newer generation HPK
1319 SiPMs, with physical trenches, are well below at $\sim 25\%$. The DCR on the other hand seems to be
1320 similar for each device. The LCT5 7mm SiPM at this point of operation seems to have the lowest
1321 DCR among them, but the measurements of this device have not yet reached the maximum PDE
1322 value and will be extended, higher PDE is possible.

1323 In both cases, the low PDE of the SensL SiPM makes it not competitive.

1324 7.4 Photon Detection Efficiency 1325

1326 The measurement technique in this work utilizes only dark counts and aims at giving an under-
1327 standing of the OCT and temperature dependencies of the different SiPMs proposed, therefore
1328 no PDE measurements are possible. The point of operation with the highest PDE as well as the

Device	Min. OCT			Max. PDE		
	OCT	DCR	PDE	OCT	DCR	PDE
CHECS	15%	0.5 MHz	25% (DS)	50%	5 MHz	48% (DS)
LCT5 6mm	15%	3.4 MHz	49% (Nagoya)	22%	5 MHz	51% (Nagoya)
LCT5 7mm	15%	2.0 MHz	42% (Catania)	25%	2.5 MHz	53% (Catania)
LVR 6mm	15%	2.5 MHz	43% (Nagoya)	>27%	>6MHz	>50% (Nagoya)
SensL	15%	3.0 MHz	37% (Nagoya)	30%	6 MHz	40% (Nagoya)

Figure 50: Comparison table of the measured devices based on the two proposed operation points for CHEC-S. First point represents minimal achievable OCT, second point represents maximum achievable PDE. PDE values taken from results of other groups and datasheet values. Note that the LCT5 6mm device can achieve even lower OCT values ($\sim 3\%$ at $V_{ov} = 2.5$)

1329 PDE versus OCT behaviour is determined by a different group in Japan, at the University of
 1330 Nagoya. A figure showing the behavior of PDE versus OCT is the usual procedure of compar-
 1331 ing SiPMs, it gives a correlated overview of the two most significant characteristics. This gives
 1332 insight of the capabilities of the different devices compared to the two proposed points of op-
 1333 eration in section(7.3). For consistency and to make comparison between group results easier,
 1334 the PDE ascertained by the groups, of devices in common, compared to the resulting OCT from
 1335 this work produces figure(51).

1336

1337 Comparing all devices at the two proposed points of operation produces the table in
 1338 figure(50). This table together with figure(51) of the five measured devices in this work, where
 1339 PDE data is accessible, is used to confirm results between groups and assist in the decision on
 1340 the most viable SiPM for CHEC-S. The final decision will be taken by the GCT group based on
 1341 measurements on substantially more devices (see section(H), for the complete list).

1342 The PDE of SiPMs, when plotted versus the corresponding OCT at a common over-voltage point
 1343 show the behaviour in figure(51). A clearly visible saturation after a certain OCT marks the
 1344 point, from where an increase in power no longer increases photon-detection capabilities. An
 1345 increase in OCT without rising PDE would have an adverse effect on the detectors resolution.

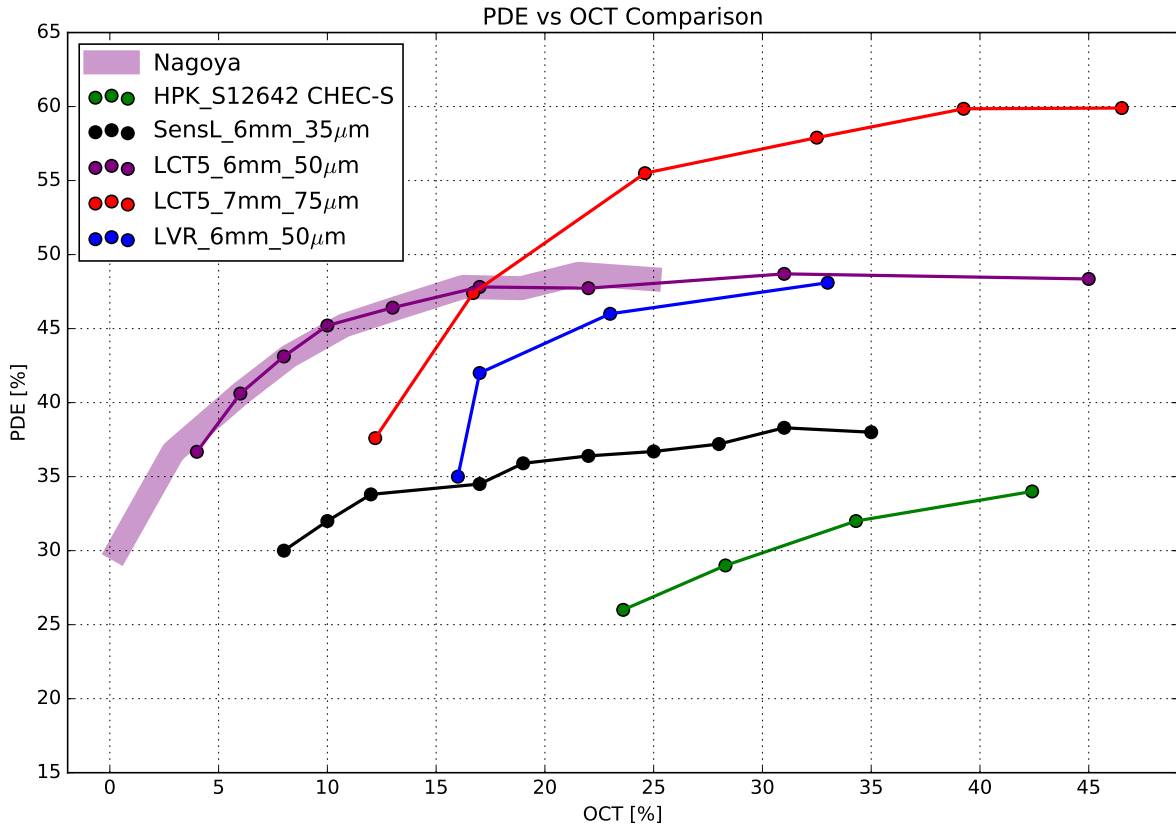


Figure 51: PDE results from the University of Nagoya parametrized with OCT results from this work, where available. PDE measurements at $\lambda = 400\text{nm}$. The faded purple bar shows an example measurement of the University of Nagoya. An optimum device for IACT application would be in the upper left region.

- 1346 The prototype LCT5 7mm fig(51)(red) device reaches the highest PDE. This is expected for de-
 1347 vices with larger cell-size and pixel-size, leading to a higher fill-factor. The increase in size and
 1348 therefore PDE comes with a trade-off, increasing size comes with a rise of DCR and OCT, which
 1349 are very high at this point (at $\sim 25\%$).
 1350 The commercially available LCT5 6mm (HPK S13360) SiPM shows the most promising results.
 1351 It reaches a high PDE very quickly compared to its OCT, with $\sim 47\%$ before the OCT reaches
 1352 20%. Compared to this, the OCT of the LVR 6mm at a point where the PDE saturates and
 1353 reaches the same PDE is very high.
 1354 The LCT5 6mm device seems the most promising for the low-OCT point, while the LCT5 7mm
 1355 device would be the choice at the high PDE point. Being a fairly new technology, the LVR device
 1356 is being developed and will be competitive.
 1357 Due to the low fill-factor, the PDE of the SensL FJ60035 device makes it not competitive. The
 1358 HPK S12642 device is clearly sub-optimal for CHEC-S, but will still be used for initial tests. It
 1359 shows a very low PDE compared to a very high OCT at this point.

8 Conclusion and Outlook

1362 Over the course of this work five new-generation SiPMs have been examined in dark conditions,
1363 for their possible use in single photon detection for the high energy instrument of the Cherenkov
1364 Telescope Array.

1365 A lasting experimental teststand has been developed, that is capable to be upgraded for fu-
1366 ture illumination tests. It is a reference to the involved groups, who will build similar setups
1367 to test the every SiPM for the mass-production of the CHEC camera. The teststand involves
1368 a climate chamber for temperature regulation, that functions as a light tight box. For each
1369 SiPM pre-existent shaping electronics has been modified in order to achieve a preferred signal.
1370 Data acquisition code was developed to control the experimental parameters of the teststand
1371 remotely, and storing all experimental data from the internal memory of the oscilloscope on
1372 a Lab-PC. A data analysis procedure has been designed and developed to analyze the data of-
1373 fline, both were developed in python. The analysis method showed performance issues with
1374 measurements of devices at higher OCT levels. Illumination tests will make it easier to reach
1375 lower over-voltage ranges, due to the lower dependency of dark counts with low gain, that is
1376 characteristic in that region.

1377 Experimental studies of the SiPMs showed better performance at lower temperatures. In ob-
1378 servation conditions, temperatures lower than 25 °C are unfortunately not expected. Even at
1379 those temperatures SiPMs are a strongly considered candidate. For the examined devices, the
1380 temperature dependence of the dark noise and the gain has been studied.

1381 By now, only dark measurements can be conducted, but once a tunable lightsource and
1382 monochromator is installed, light measurements are possible. Before that, a solution for the
1383 potential warm-up of the SiPM surface must be found.

1384 The work on both, the teststand and the analysis method, will be expanded in the future. Fol-
1385 lowing this work the involved groups start to exchange the physical devices for better coverage
1386 of the measured characteristics.

1387 For part of the measured devices, strong correlations between the involved groups have been
1388 found, the other part contained discrepancies, that are only in part understood. The exchange
1389 of physical devices will clarify the source.

1390 Comparing the devices measured in this work showed the LCT5 generation to be favorable for
1391 both proposed points of operation of CHEC-S. There is a new technology, LVR, that is promising
1392 and still being developed.

9 Glossary

- 1393 1. IACT - Imaging Atmospheric Cherenkov Telescope
1394
1395 2. VHE - Very High Energy
1396
1397 3. CTA - Cherenkov Telescope Array
1398
1399 4. LST - Large Sized Telescope
1400
1401 5. MST - Medium Sized Telescope
1400
1402 6. SST - Small Sized Telescope
1403
1404 7. GCT - Gamma Cherenkov Telescope
1405
1406 8. CHEC - Compact High Energy Camera (CHEC-M based on MAPMs, CHEC-S based on
1403 SiPMs)
1404
1405 9. SiPM - Silicon Photomultiplier
1406
1407 10. MAPM - Multi Anode Photomultipliertubes
1408
1409 11. p.e. - photoelectron
1410
1411 12. DCR - Dark Count Rate
1408
1412 13. OCT - Optical Cross Talk
1409
1410 14. PDE - Photon Detection Efficiency
1411
1412 15. HPK - Hamamatsu Photonics K.K.
1413 16. SensL - Sense Light
1412
1413 17. LCT - Low Cross Talk
1413
1413 18. LVR - Low Voltage Range

10 Bibliography

References

- 1418 [1] Jim Hinton et al. *Teraelectronvolt Astronomy* Ann. Rev. Astron. Astrophys., 47:523
- 1419 [2] The CTA Consortium *Design Concepts for the Cherenkov Telescope Array CTA, An Advanced*
1420 *Facility for Ground-Based High-Energy Gamma-Ray Astronomy* ; arXiv:1008.3703v3 [astro-
1421 ph.IM] 11 Apr 2012
- 1422 [3] Teresa Montaruli et al. *The small size telescope projects for the Cherenkov Telescope Array*
1423 arXiv:1508.06472v1 [astro-ph.IM]
- 1424 [4] *The ASTRONET Infrastructure Roadmap* ISBN: 978-3-923524-63-1
- 1425 [5] Jim Hinton et. al *Seeing the High-Energy Universe with the Cherenkov Telescope Array* As-
1426 troparticle Physics 43 (2013) 1-356
- 1427 [6] R. López-Coto for the HAWC collaboration *Very high energy gamma-ray astronomy with*
1428 *HAWC* arXiv:1612.09078v1 [astro-ph.IM] 29 Dec 2016
- 1429 [7] John Murphy *SensL J-Series Silicon Photomultipliers for High-Performance Timing in Nuclear*
1430 *Medicine*
- 1431 [8] A. N. Otte et al. *Characterization of three high efficient and blue sensitive Silicon photomul-*
1432 *tipliers* arXiv:1606.05186v2 [physics.ins-det] 26 Jan 2017
- 1433 [9] A. Bouvier et al. *Photosensor Characterization for the Cherenkov Telescope Array: Silicon*
1434 *Photomultiplier versus Multi-Anode Photomultiplier Tube* ; arXiv:1308.1390v1 [astro-ph.IM]
1435 6 Aug 2013
- 1436 [10] V. Vassilieva , S. Fegan *Wide field aplanatic two-mirror telescopes for ground-based*
1437 *gamma-ray astronomy* Astropart. Phys. 28 (2007) 10, [astro-ph/0612718] arXiv:astro-
1438 ph/0612718v2 12 Apr 2007
- 1439 [11] A. Zech, J.-P. Amans, S. Blake et al. *SST-GATE: A dual mirror telescope for the Cherenkov*
1440 *Telescope Array* arXiv:1307.3035v1 [astro-ph.IM] 11 Jul 2013
- 1441 [12] Julien Rousselle et al. *Construction of a Schwarzschild-Couder telescope as a candidate for*
1442 *the Cherenkov Telescope Array: status of the optical system* arXiv:1509.01143v1 astro-ph.IM
- 1443 [13] J. Rosado S. Hidalgo *Characterization and modeling of crosstalk and afterpulsing in Hamamatsu*
1444 *silicon photomultipliers.* arXiv:1509.02286v2 [physics.ins-det] 21 Oct 2015
- 1445 [14] K. Boone, Y. Iwai, F. Retiere, C. Rethmeier *Delayed avalanches in Multi-Pixel Photon Counters*
1446 arXiv:1703.04651v1 [physics.ins-det] 14 Mar 2017

- 1447 [15] Robert G. Wagner et al. *The Next Generation of Photo-Detectors for Particle Astrophysics*
1448 arXiv:0904.3565v1 [astro-ph.IM] 22 Apr 2009
- 1449 [16] *Opto-semiconductor handbook Chapter 03 Si APD, MPPC*. Hamamatsu Photonics K.K.
- 1450 [17] Jonathan Biteau et al *Performance of Silicon Photomultipliers for the Dual-Mirror Medium-*
1451 *Sized Telescopes of the Cherenkov Telescope Array* arXiv:1508.06245v1 [astro-ph.IM] 25 Aug
1452 2015
- 1453 [18] Richard White *private communication*. 2017
- 1454 [19] Hiro Tajima *private communication*. 2017
- 1455 [20] Koei Yamamoto *private correspondence*. 2016
- 1456 [21] Luigi Tibaldo *Initial testing at MPIK (wb July 18 2016)* July 2016
- 1457 [22] T. C. Awes et al. *Configurable electronics with low noise and 14-bit dynamic range for*
1458 *photodiode-based photon detectors* Nuclear Inst. and Methods in Physics Research, Mai 2006
- 1459 [23] Maurice Stephan. *Design and Test of a Low Noise Amplifier for the Auger Radio Detector*
1460 Diploma Thesis, RWTH Aachen University, July 2009
- 1461 [24] http://astro.desy.de/gamma_astronomy/cta/index_eng.html
- 1462 [25] [http://www.ung.si/en/research/laboratory-for-astroparticle-physics/
1463 projects/cta/](http://www.ung.si/en/research/laboratory-for-astroparticle-physics/projects/cta/)
- 1464 [26] [http://www.ung.si/en/research/laboratory-for-astroparticle-physics/
1465 projects/fermi-lat/](http://www.ung.si/en/research/laboratory-for-astroparticle-physics/projects/fermi-lat/)
- 1466 [27] [http://212.71.251.65/aspera//index.php?option=com_content&task=
1467 blogcategory&id=111&Itemid=234](http://212.71.251.65/aspera//index.php?option=com_content&task=blogcategory&id=111&Itemid=234)

1468 1469 11 Appendix

1470 1471 A CTA

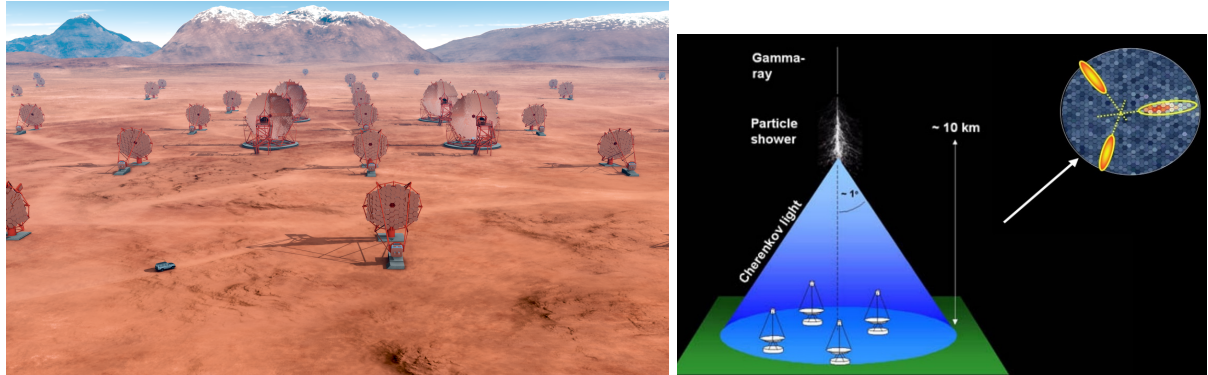


Figure 52: A render of the finished CTA Array at the site in Chile (left) with visible LSTs and MSTs, and the Shower Path Reconstruction technique of the stereoscopic view employed by current IACT experiments like HESS, MAGIC, VERITAS (right).

1472 1473 B progenitor experiments of CTA



Figure 53: IACT Projects: HESS in the Khomas Highland, Namibia. MAGIC at the Roque de los Muchachos Observatory on La Palma , one of the Canary Islands. VERITAS at Mount Hopkins, Arizona, USA

C OCT dependency on cellsize

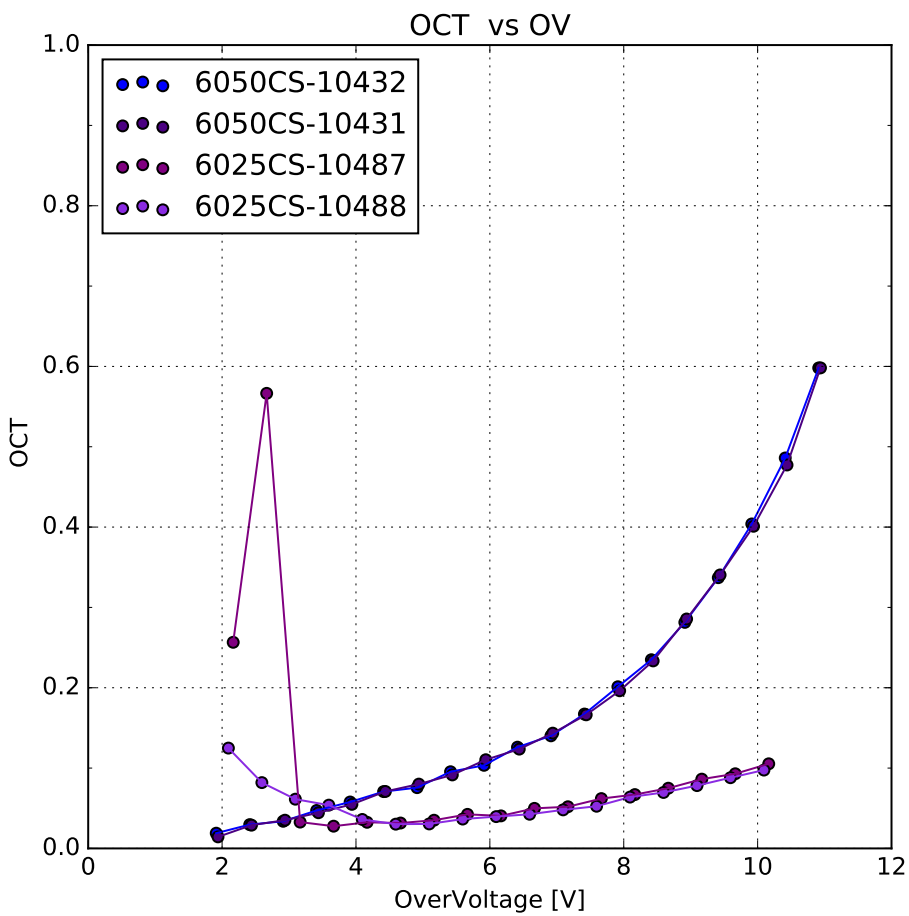
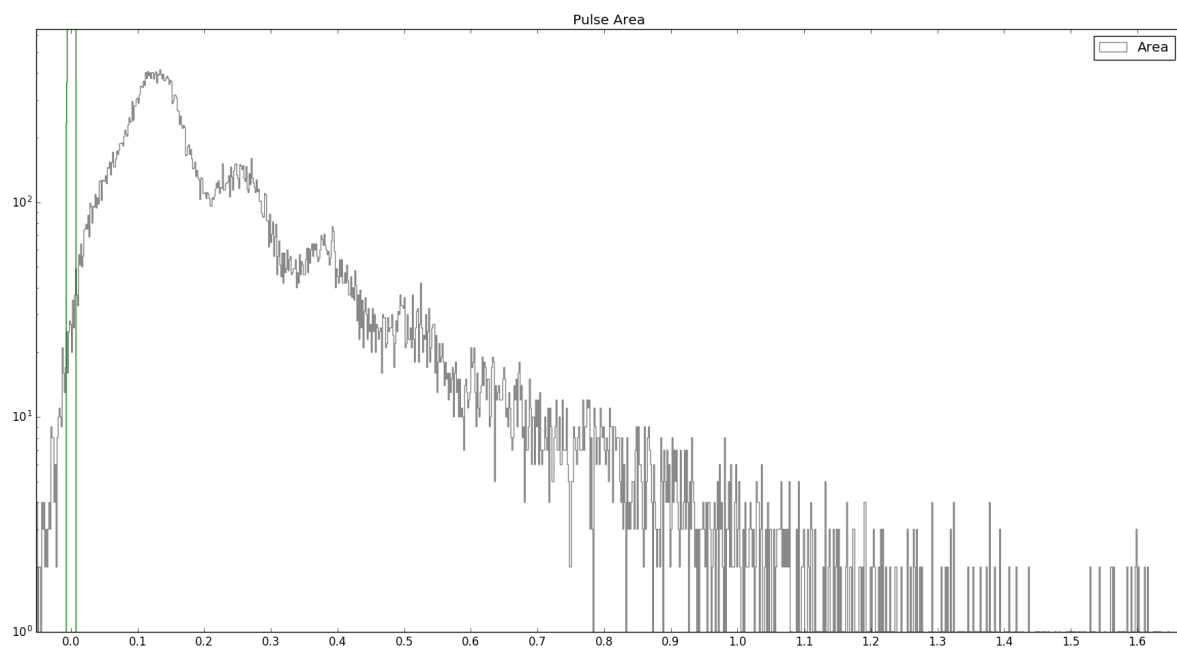
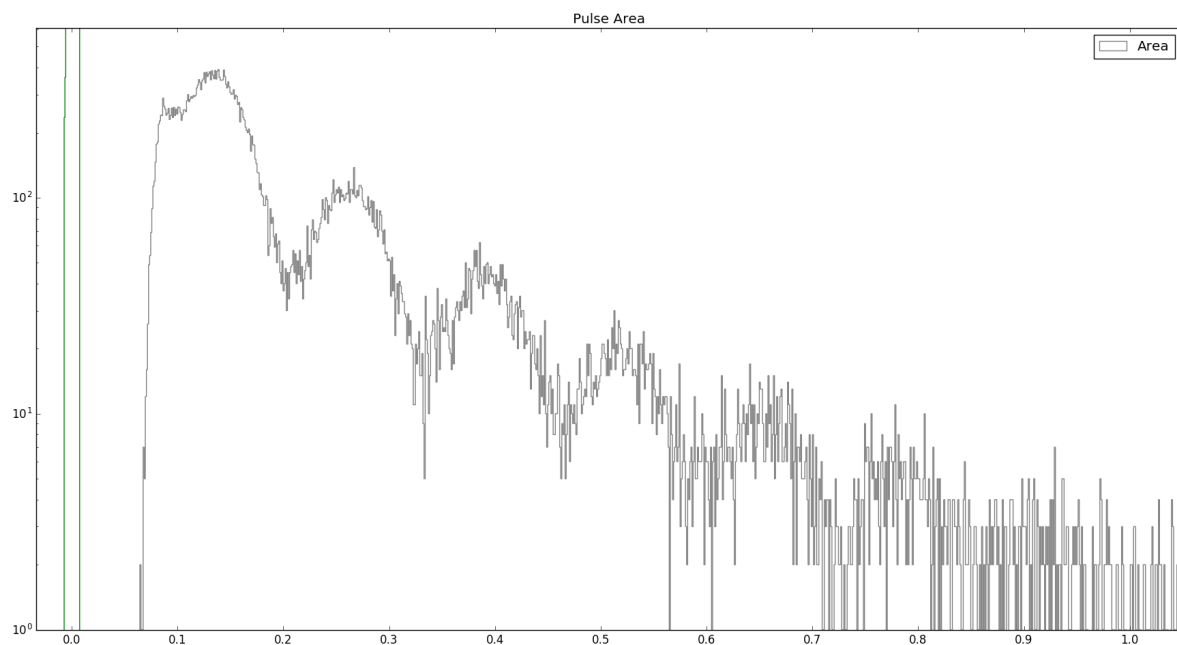


Figure 54: Results of the OCT of two sets of two similar HPK S13360 devices, that only differ in their respective cell-size. HPK S13360 is the first device incorporating physical trenches in the upper layer, optically isolating each cell. Consequence to this is a drastic reduction in prompt cross-talk. Delayed cross-talk and afterpulsing are basically unaffected. Upscaling of the $25\mu\text{m}$ results shows an overlap between the two, see text.

In figure(54) the results of the complete OCT of two sets of $50\ \mu\text{m}$ and $25\mu\text{m}$ HPK S13360 devices are shown. Plotting the results of two similar devices, only different in their cell-size, and then multiplying the $25\ \mu\text{m}$ results by the factor derived from their difference in area, here $\times 4$, a correlation is visible. Scaling up the OCT of the $25\ \mu\text{m}$ cell, shows an overlap between the two cell-sized pixels. This means, that the OCT is directly area and therefore cell-size dependent. Research by J. Rosado and S. Hidalgo [13] on the cross-talk probability of Hamamatsu SiPMs showed through Monte Carlo simulation, that the prompt crosstalk mostly takes place in a small area of pixels (~ 8) around the primary one. Which means, that the cross-talk is directly increasing with increasing cell-size, or in other words: with chance to diffuse to a neighboring cell. Small cells reduce the chance, as there is less area to a neighboring cell to pass through. Since the measurements conducted in this work do not differ between the range of secondary

¹⁴⁸⁷ avalanche effects, the OCT shown contains every aspect, prompt and delayed as well as after-
¹⁴⁸⁸ pulsing.

D Pulse Area Spectra of different integration window widths



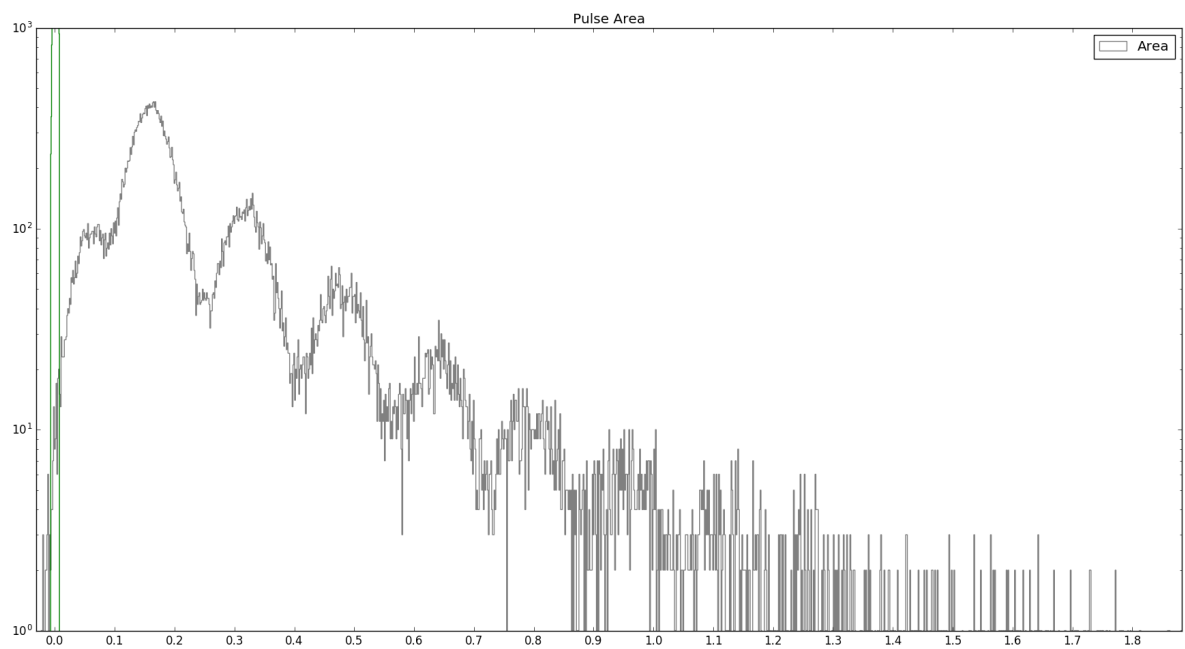


Figure 55: Pulse Area Spectra with window widths of 5 left 5 right (top), 5 left 20 right (middle), 10 left 10 right (bottom) bins respectively. Left of the 1p.e. peak of the top picture a part of the 0p.e. peak is visible. The middle figure shows the distortion an asymmetrical integration window causes. The bottom figure is the employed integration window to derive the pulse area histogram.

E Pulse Area Spectra examples

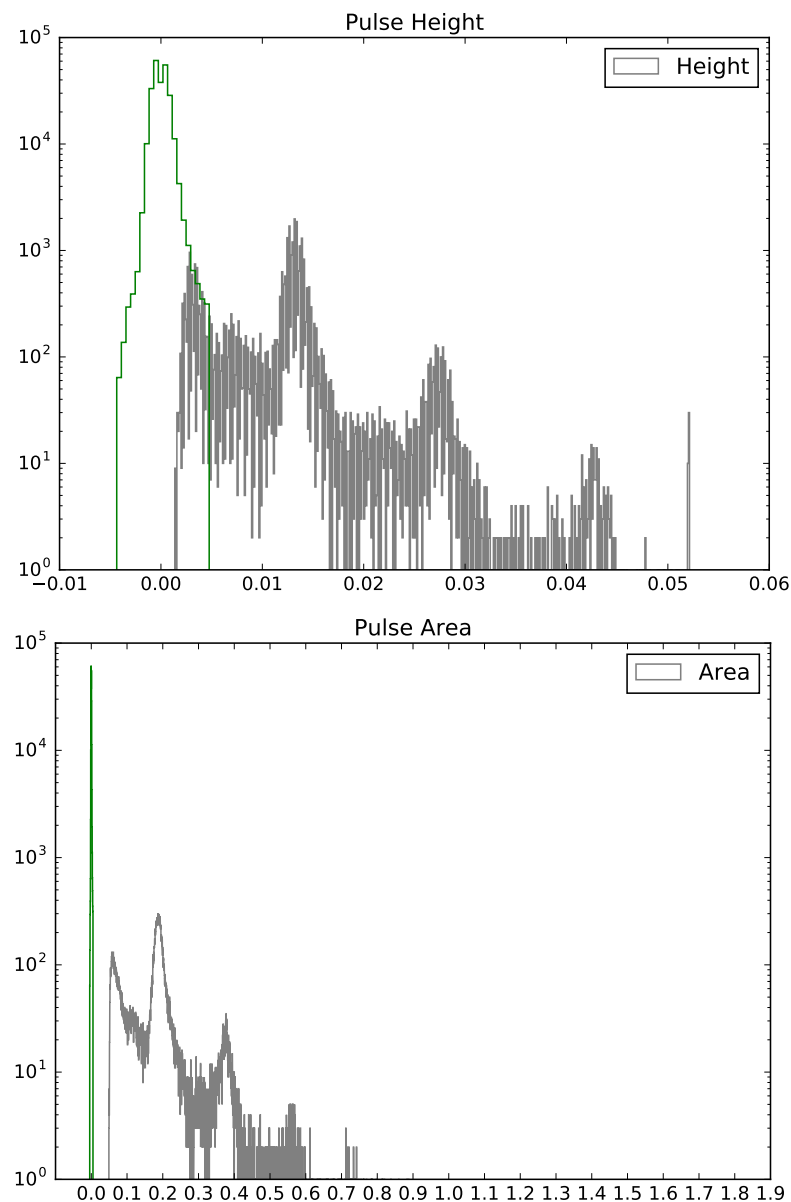


Figure 56: Pulse height and pulse area spectrum of the S12642 device at $V_b = 58V$ and $T = 25^\circ C$. The x-axis is pulse height and pulse area respectively and the y-axis is number of counted pulses

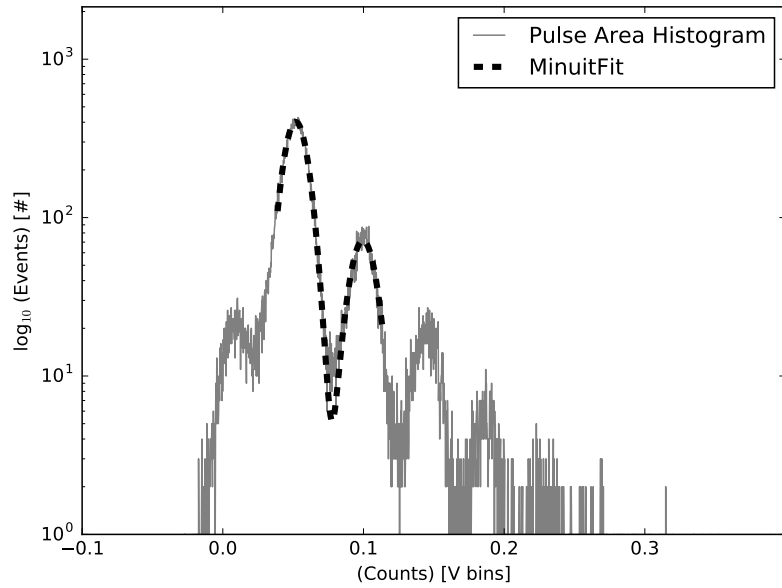


Figure 57: Pulse area spectrum of the S13360 LCT5 6mm device at $V_b = 56.2\text{V}$ at $T = 25^\circ\text{C}$. The x-axis is pulse height and pulse area respectively and the y-axis is number of counted pulses. The dashed black line shows the fitted function.

F BreakdownVoltage

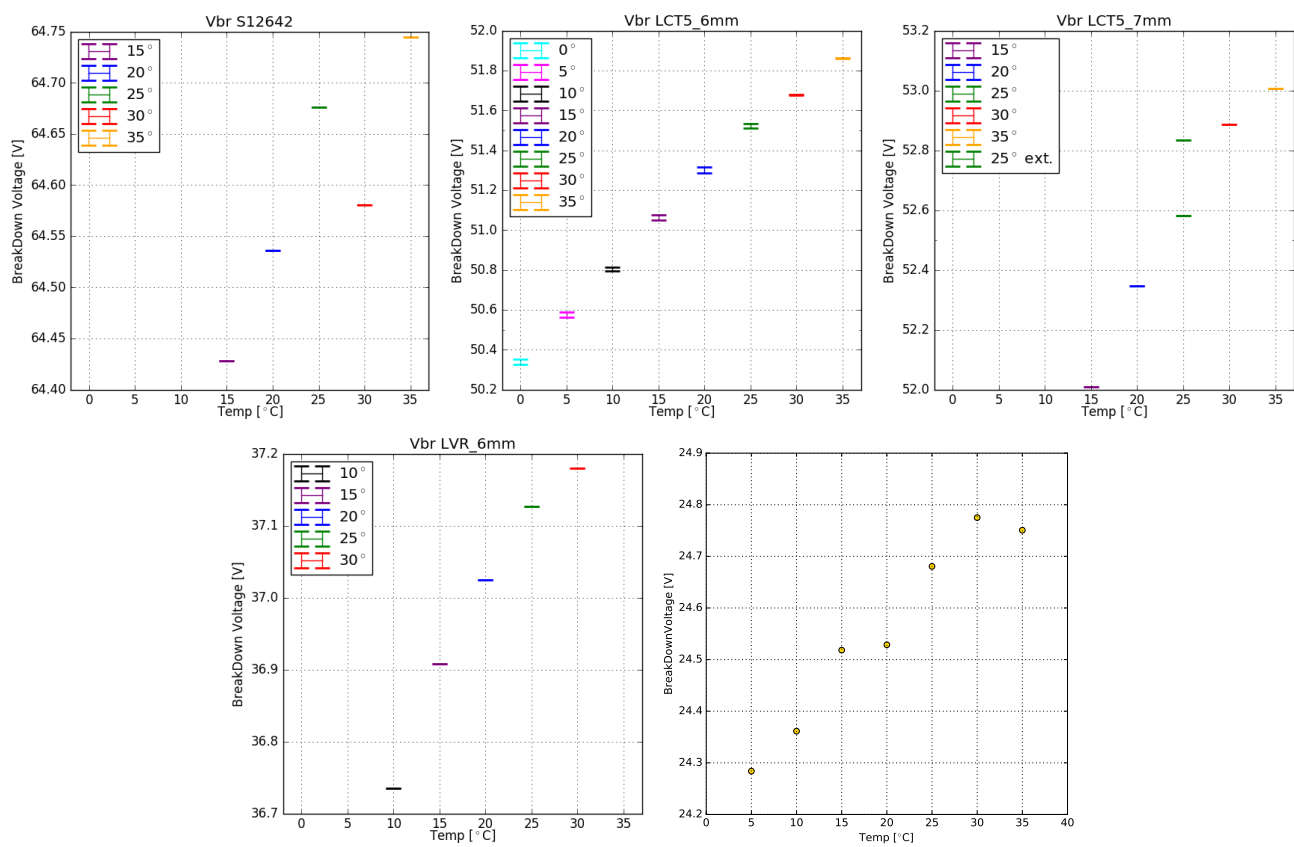


Figure 58: Dependency of the breakdown-voltage of temperature for the 5 measured devices.

For LCT5 7mm , the extended range measurement adds an extra datapoint at 25 °C
 HPK S12642 (CHEC-S) (top left) ; HPK LCT5 6mm (top middle) ; HPK LCT5 7mm (top right) ; HPK LCT5 LVR 6mm (bottom left) ; SensL FJ60035 (bottom right).

Device	$\Delta V / T$ [mV/°C]
CHECS	13.1 ± 4.1
LCT5 6mm	43.5 ± 0.4
LCT5 7mm	53.0 ± 4.0
LVR 6mm	25.6 ± 2.6
SensL	15.0 ± 1.1

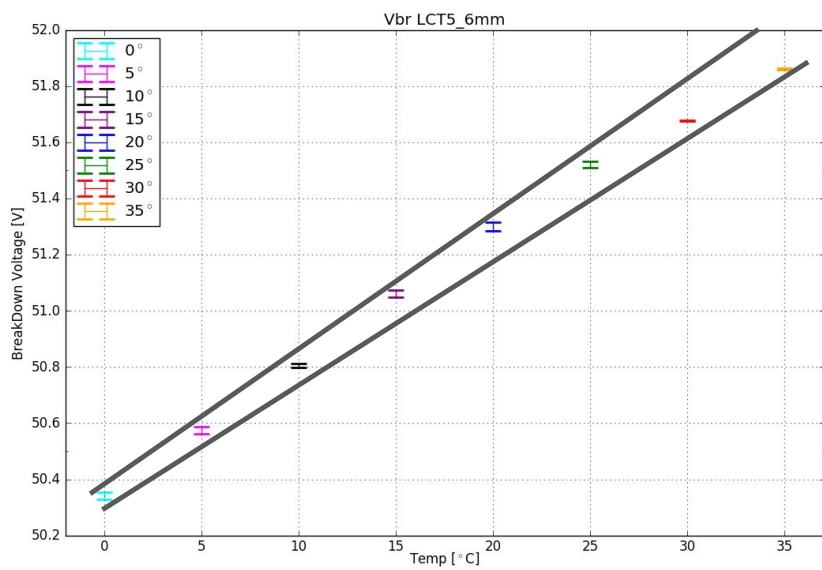
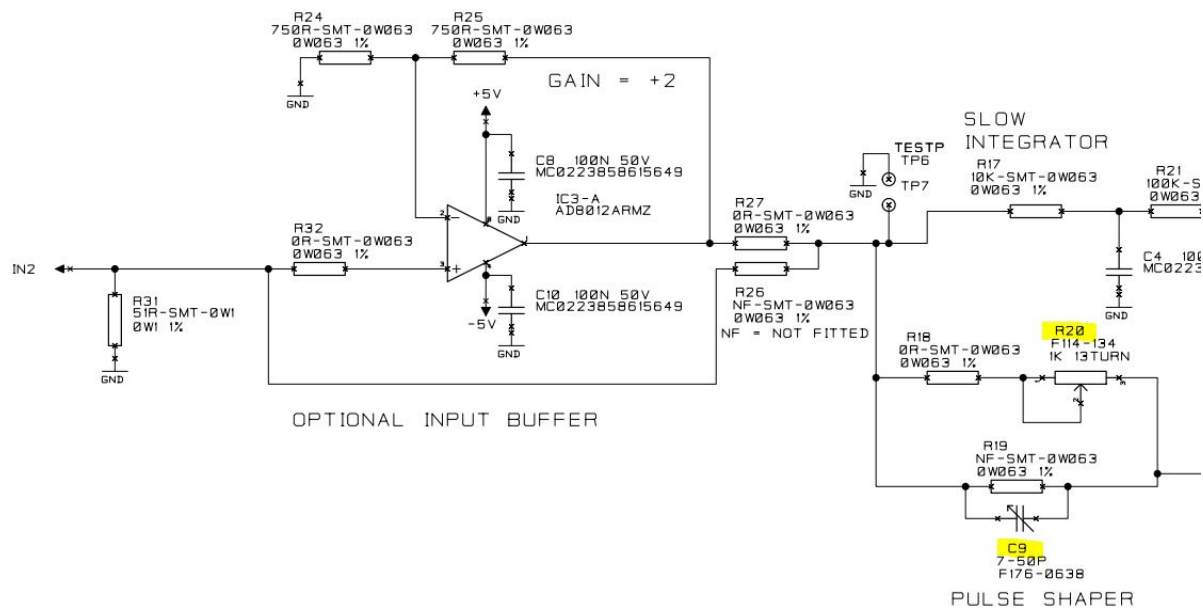


Figure 59: The extracted breakdown-voltage dependence of all measured devices, derived from two regression lines and their mean. For some devices the breakdown-voltage dependency is known through datasheet values. S12642 = 60 mV/°C, S13360 = 54 mV/°C, SensL FJ60035 =<21.5 mV/°C

G Shaper**Figure 60:** Full schematic of the shaper developed at the University of Leicester.

H SiPM list tested at University of Nagoya

Manufacturer	pixel size [mm]	cell size [μm]	technology	coating
HPK S12642-1616PA-50 *CHEC-S SiPM	3	50	standard	silicon
HPK LCT5 S13360-6050CS	6	50	LCT5	silicon
HPK LCT5 6.975MM-SIL Single	6.915	75	LCT5	silicon
HPK 6050HWB-LVR-LCT	6	50	LVR	silicon
SensL FJ60035	6	35	TSV	glass
HPK S12572-050C	3	50	standard	silicon
HPK S13360-3050CS	3	50	LCT5	silicon
HPK S13360-3050VE	3	50	LCT5	epoxy
HPK S13360-3075CS	3	75	LCT5	silicon
HPK S13360-6075CS	6	75	LCT5	silicon
HPK LVR-3050CS	3	50	LVR	silicon
HPK LVR-6050CS	6	50	LVR	silicon
HPK LVR-6075CS	6	75	LVR	silicon
FBK NUV (reference device)	6	30	NUV	?
HPK LVR-S-50-3	3	50	LVR	silicon
HPK LVR-S-50-6	6	50	LVR	silicon
HPK LVR2-S-50-6	6	50	LVR 2	silicon
HPK LVR2-N-50-6	6	50	LVR 2	none
HPK LVR2-S-50-7	7	50	LVR 2	silicon

Figure 61: List of SiPM device candidates for CHEC-S measured by involved groups. *(LCT5: Low Cross Talk 5th iteration , LVR: Low Voltage Range , TSV: through silicon via , LVR2: Low Voltage Range 2nd iteration , standard: no trenches) [19]

I CHEC-S pixel comparison

1501 Comparison of results from 10 different pixels on the CHEC-S (HPK S12642-1616PA-50) array.
 1502 Every pixel is analyzed with the same technique and analysis parameters.

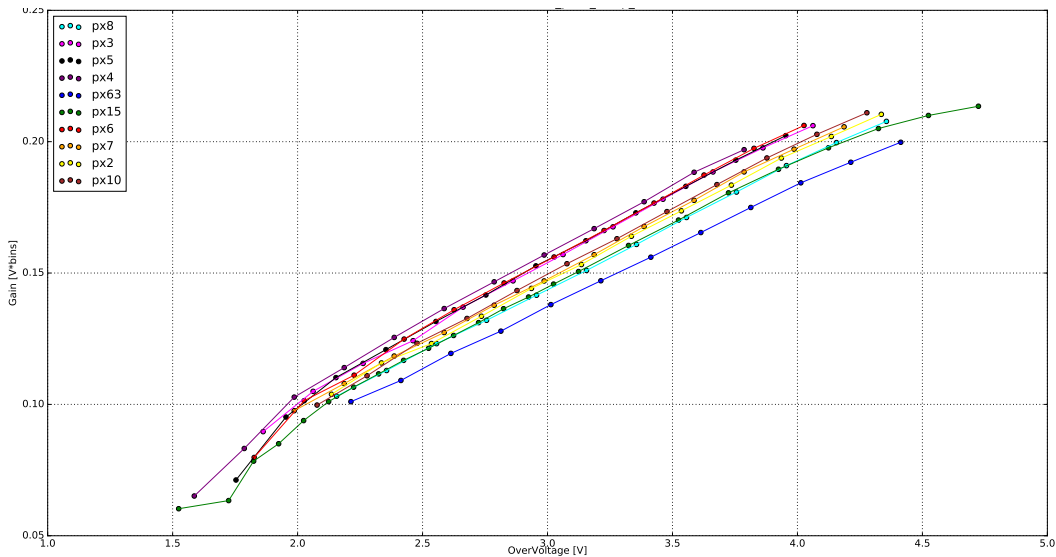


Figure 62: Gain comparison of 10 different pixels of the CHEC-S (HPK S12642-1616PA-50) array

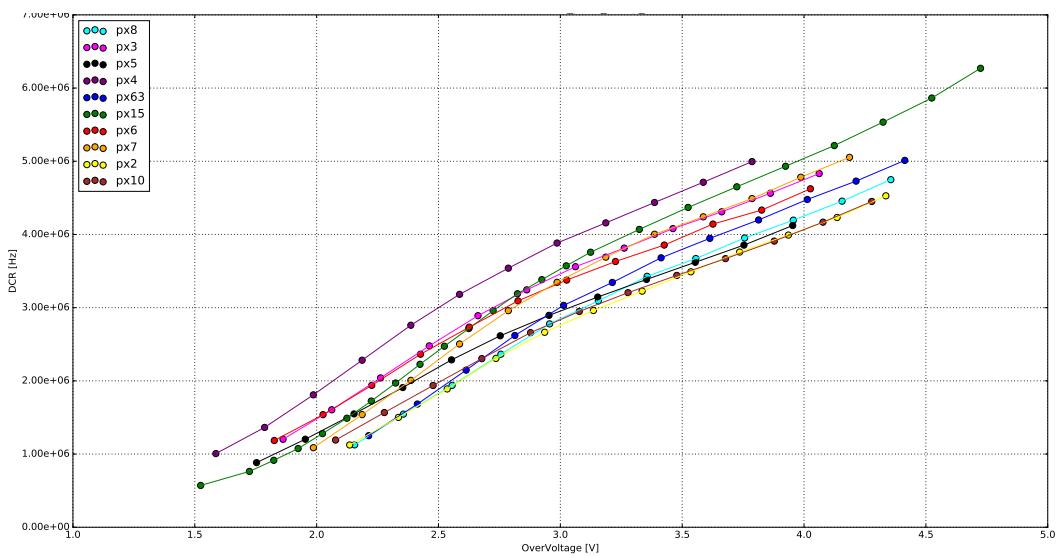


Figure 63: DCR comparison of 10 different pixels of the CHEC-S (HPK S12642-1616PA-50) array

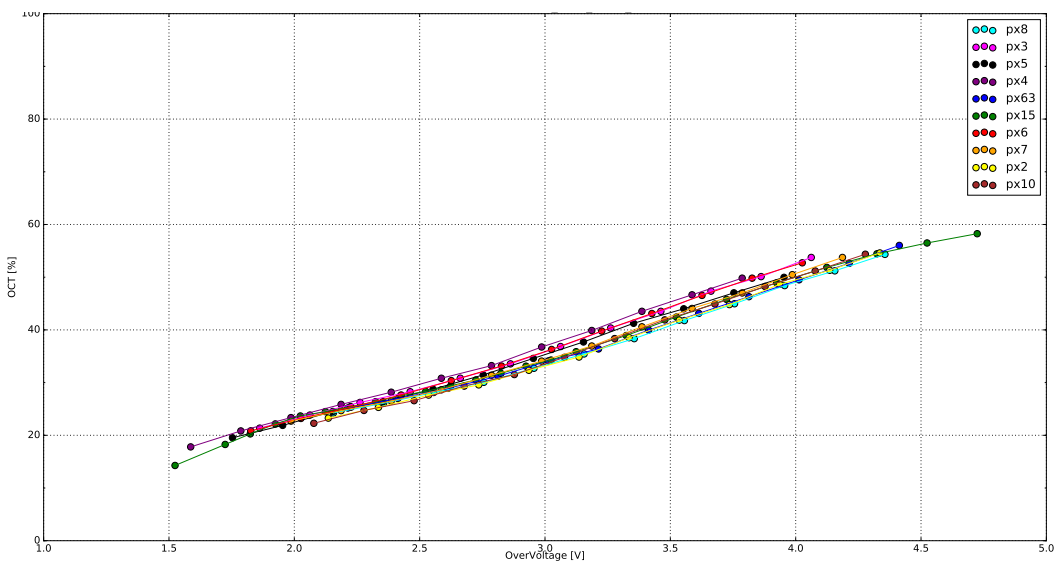


Figure 64: OCT comparison of 10 different pixels of the CHEC-S (HPK S12642-1616PA-50) array

J Additional Data Analysis Plots

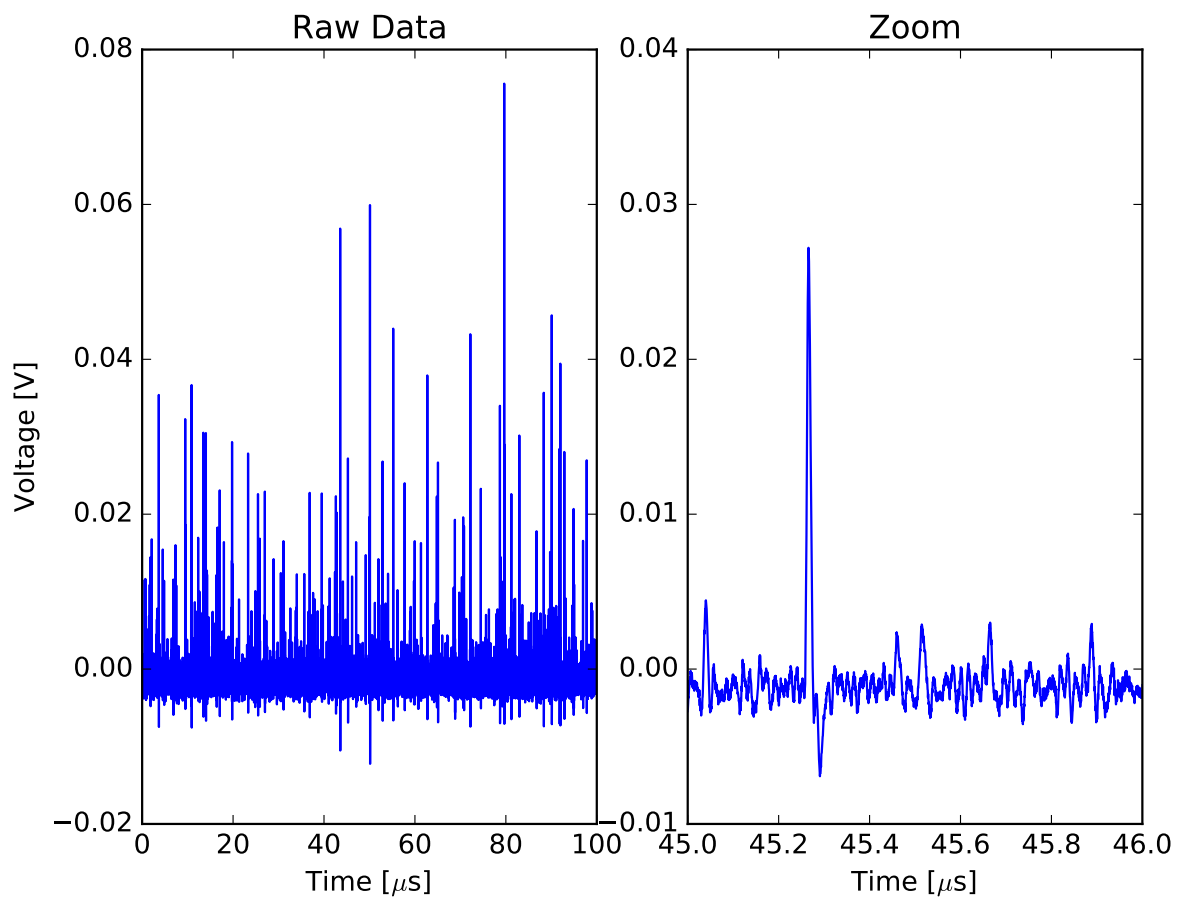


Figure 65: Raw data from the oscilloscope, converted, but no analysis steps taken.

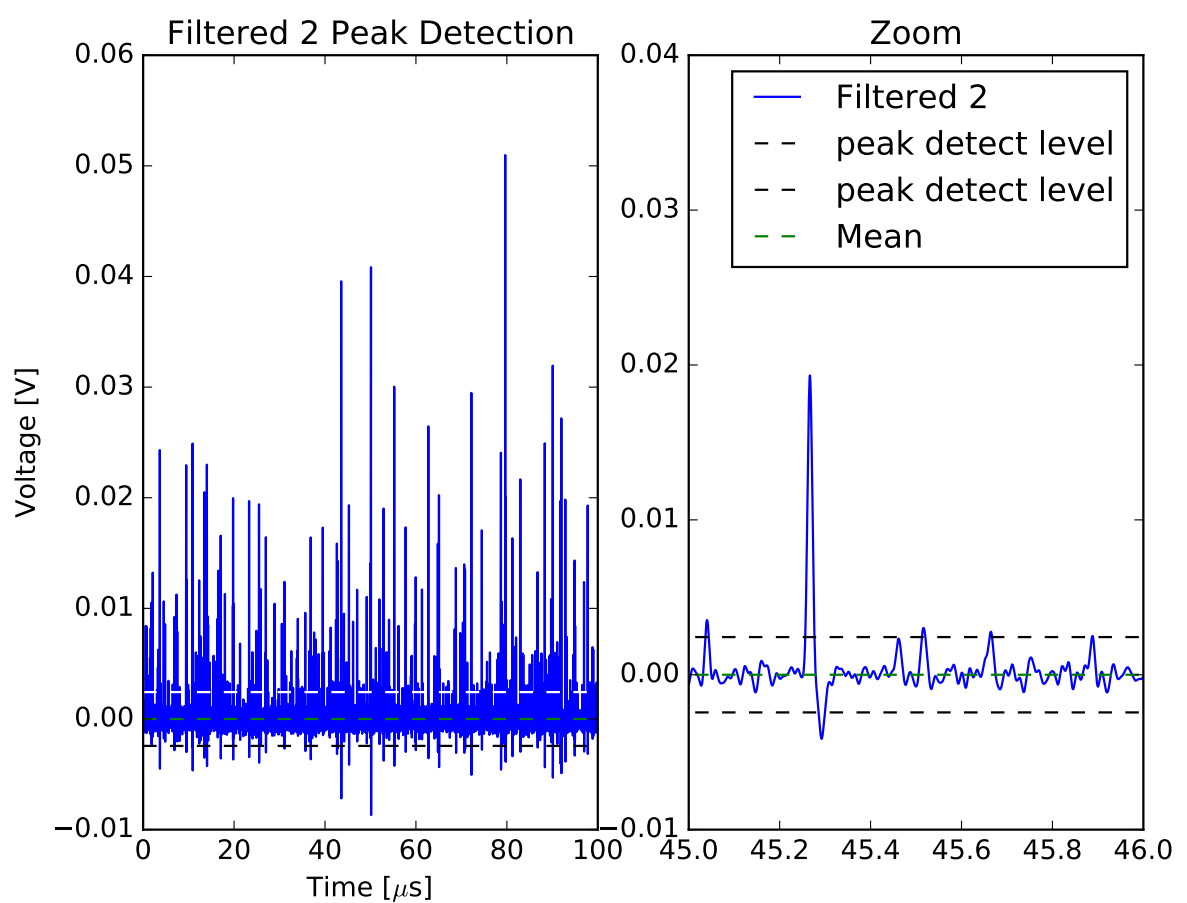


Figure 66: Peak detection level visible on filtered signal 2.

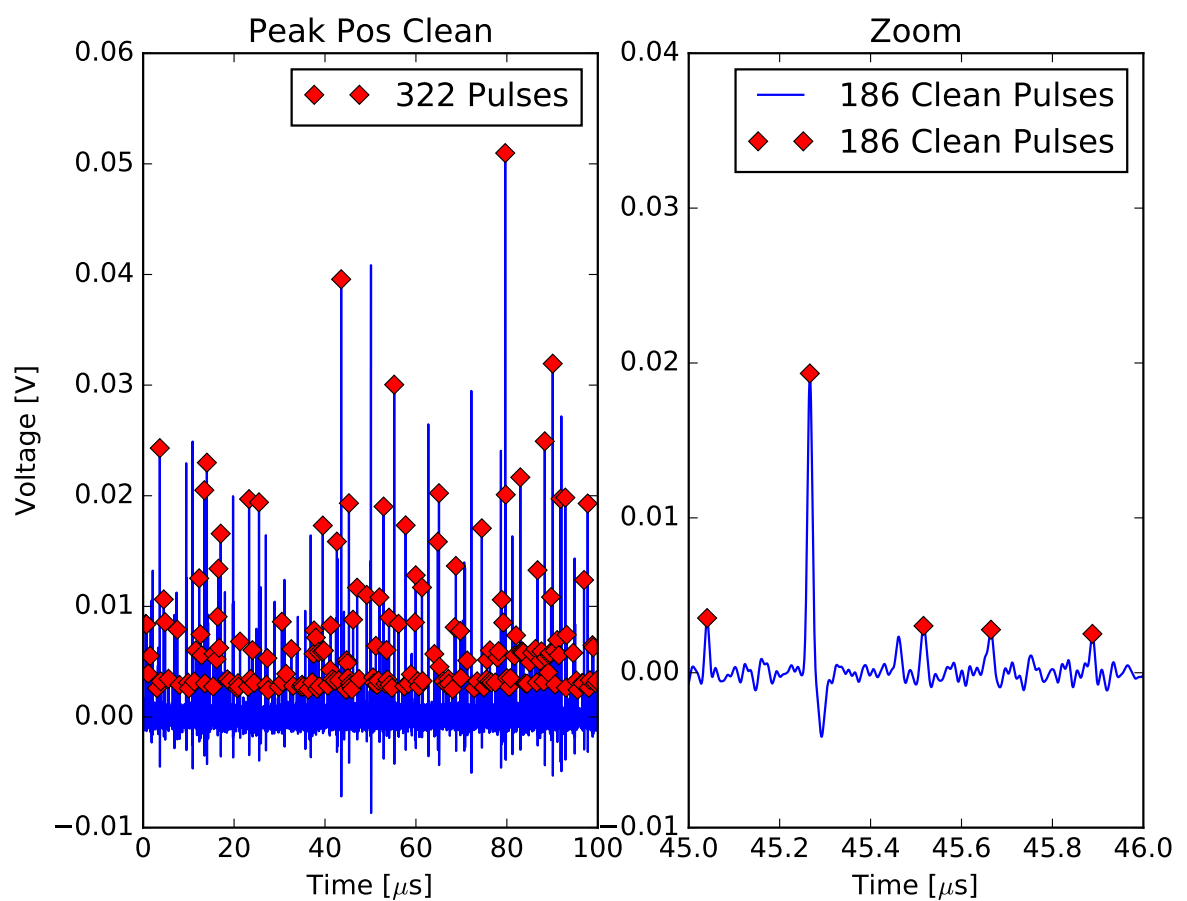


Figure 67: Number of peaks detected, clean keyword is to check for peak proximity.

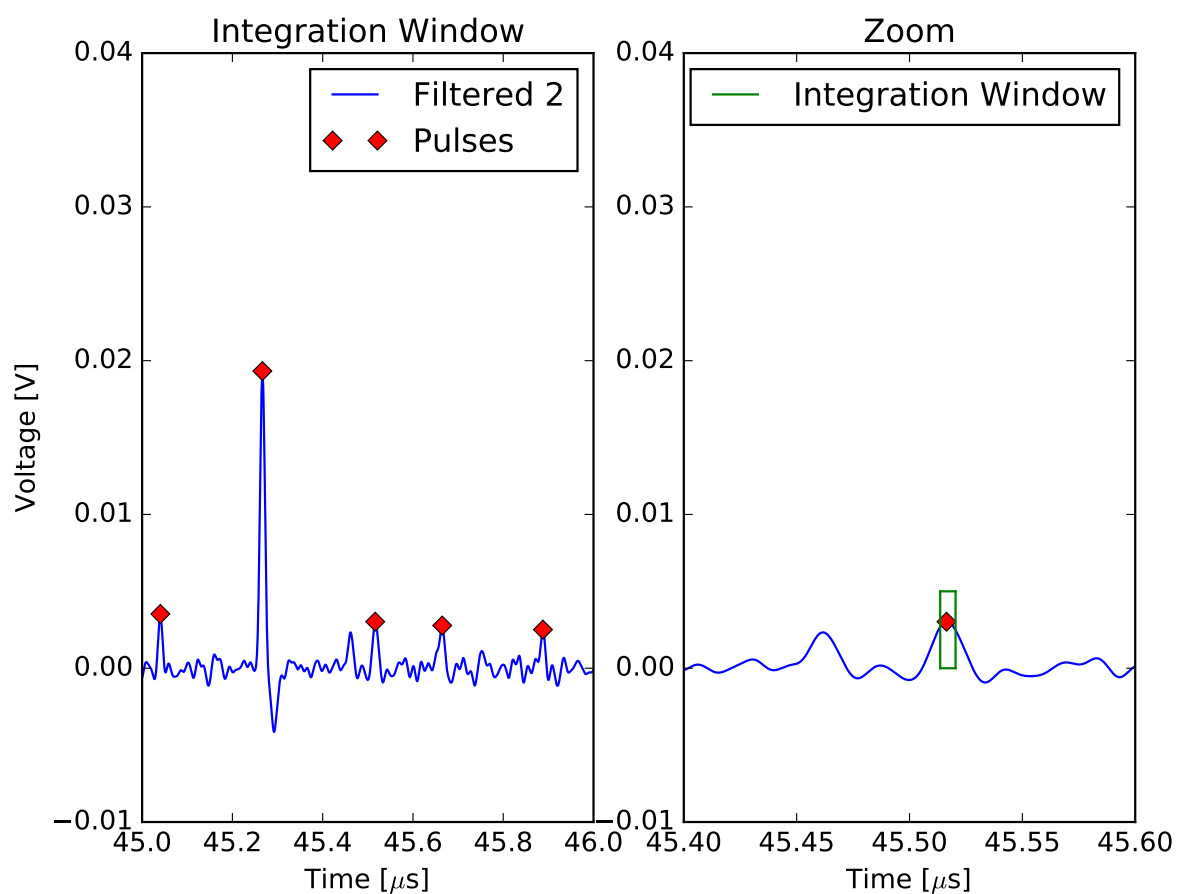


Figure 68: Illustration of an integration window applied to the pulse.

1505 K Multi incident probability and Optical Cross Talk

1506 , _____>,

1507 With increasing DCR the probability of two dark events happening at the same time rises with
1508 increasing bias-voltage. This has an effect on the calculated OCT. In the event of 2 1p.e. pulses
1509 coinciding with each other, they could be misinterpreted as 1 2p.e. pulse. Taking, for example,
1510 the DCR of S13360, 4 MHz at $V_{ov} = 8V$ and $T = 25^\circ C$, with the FWHM of the characteristic
1511 pulse as 5.6 ns we can calculate the probability of two coinciding pulses as $\sim 2.2\%$. This proba-
1512 bility has a direct effect on the calculated OCT (eq:7), in reducing it compared to the calculation.
1513 The OCT at this point is only $\sim 17\%$, but a $\sim 2.2\%$ shift of the number events $N_{events(\geq 1.5p.e.)}$ to
1514 $N_{events(\geq 0.5p.e.)}$ lowers the OCT by $\sim 0.75\%$. Even though the multi hit coincidence is low, this
1515 shows that there are analysis related problems with high DCRs.

1516

1517

1518 For devices with high DCR and OCT like S12642 this effect grows in magnitude. At only
1519 $V_{ov} = 4.5V$ at $25^\circ C$ the DCR is 6 MHz. With the pulse FWHM of 9 ns this leads to a coincidence
1520 of 5.4%. The OCT at that point is 55%, so a reduction of 5.4% of the $N_{events(\geq 1.5p.e.)}$ towards the
1521 $N_{events(\geq 0.5p.e.)}$ leads to a reduction of the OCT by 5.6%.

1522 Maybe a half FWHM overlap is more real, since now overlap is marked as true, even when
1523 the 2 pulses blur into a very blurry one by only "touching" with their FWHM. Dont know, maybe
1524 half fwhm would be more real.

1526 Erklärung zur Master-Thesis

1527 Hiermit versichere ich, die vorliegende Master-Thesis ohne Hilfe Dritter nur mit
1528 den angegebenen Quellen und Hilfsmitteln angefertigt zu haben. Alle Stellen, die
1529 aus Quellen entnommen wurden, sind als solche kenntlich gemacht. Diese Arbeit
1530 hat in gleicher oder ähnlicher Form noch keiner Prüfungsbehörde vorgelegen.

1531 Darmstadt, den April 26, 2017

1532 _____
1533 (B. Gebhardt)